SSCL-SR-1154
SSC-LOI0002

Letter of Intent to the

Superconducting Super Collider Laboratory

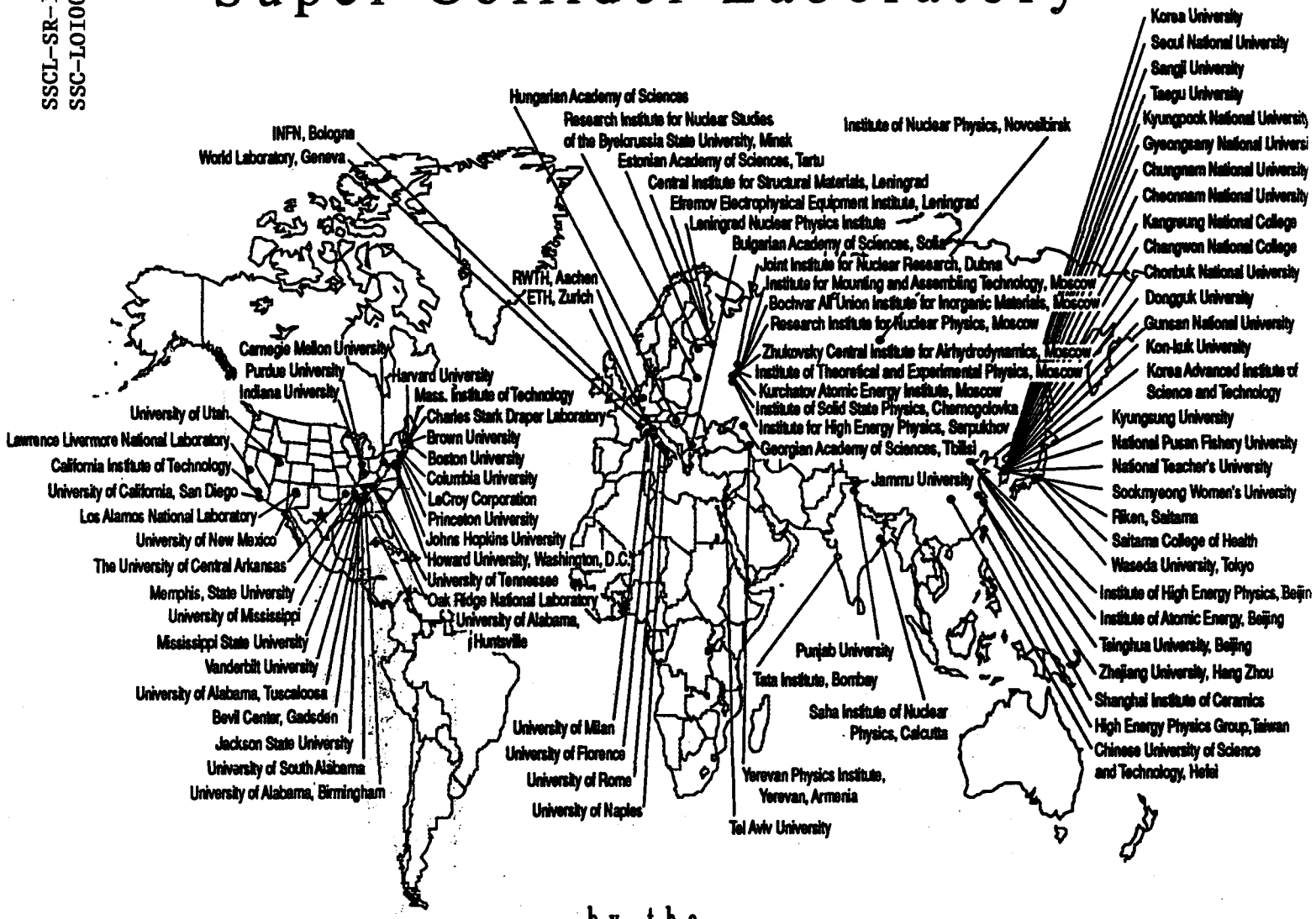

by the

L★ COLLABORATION

November 1990

Letter of Intent

to the Superconducting Super Collider Laboratory by the L* Collaboration

November 1990

The University of Alabama, Tuscaloosa, Alabama, USA
L. Baksay, J. Busenitz, D. DiBitonto, J. James, L. Junkins, X. Lu, R. Muñoz, T. Pennington, P. Razis, D. Whitcomb, K. Subhani, Y.W. Yu

The Bevill Center for Advanced Manufacturing Technology, Gadsden, Alabama, USA
G. Bennett, J. Gibney, M. Lawley, J. Lefler, J. Roberts, S. Schultz, H. Smith, C. Upton, M. Upton, J. Weaver, G. Woodliff

The University of South Alabama, Mobile, Alabama, USA
K. Clark, M. Jenkins

The University of Alabama, Huntsville, Alabama, USA
J. Gregory, Y. Takahashi

The University of Alabama, Birmingham, Alabama, USA
J. Harrisson, E. Robinson, E. Wills

Lawrence Livermore National Laboratory, Livermore, California, USA
E. Ables, R. Bionta, H. Britt, M. Capell, A. Chargin, O. Clamp, G. Deis, O. Fackler, J. Heim, C. Henning, J. Horvath, B. Jacoby, C. Johnson, D. Makowiecki, J. Miller, M. Mugge, R. Sawicki, E. Schmitt, S. Shen, D. Slack, W. Stoffel, J. Travis, R. Vital, T.J. Wenaus, R. Wong, C. Wuest

California Institute of Technology, Pasadena, California, USA
M. Chen, G. Gratta, M. Gruenewald, D. Kirkby, R. Mount, H. Newman, R.Y. Zhu

University of California, San Diego, California, USA
J.B. Branson, M. Hebert, E. Sheer, X. Sopczak

Purdue University, Lafayette, Indiana, USA
A. Bujak, R.J. DeBonte, D.D. Carmony, L. Gutay, T. McMahon, B. Stringfellow

Indiana University, Bloomington, Indiana, USA
E.D. Alyea, M. Gebhard, R. Heinz, A. Komives, L. Miller, S. Mufson, J. Musser, S. Nutter, J. Pitts, G. Spiczak, G. Turner

Iowa State University, Ames, Iowa, USA
E.W. Anderson

Johns Hopkins University, Baltimore, Maryland, USA
H. Akbari, J. Bao, C-Y. Chien, J.F. Krizmanic, J.D. Orndorff, A. Pevsner, W.J. Spangler, C. Spartiotis, A. Szalay

Boston University, Boston, Massachusetts, USA
S. Ahlen, J. Beatty, J. Brooks, T. Coan, D. Ficenec W. Lu, A. Marin, J. Rohlf, B. Zhou

Harvard University, Cambridge, Massachusetts, USA
K. Kamar, P. McBride, J. Schuette, K. Strauch

Massachusetts Institute of Technology, Cambridge, Massachusetts, USA
A.L. Anderson, U. Becker, P. Berges, J.D. Burger, Y.H. Chang, E.G. Chen, M. Chen, I. Clare, R. Clare, T.S. Dai, F.J. Eppling, M. Fukushima, M.P.J. Gaudreau, K. Giboni, C. Grinnell, E.S. Hafen, P. Haridas, G. Herten, T. Kramer, T. Lainis, D. Luckey, P. Marston, T. Matsuda, D.B. Montgomery, D. Pelly, I.A. Pless, J.M. Qian, M. Sarakinos, S.M. Shotkin, M. Steuer, J.D. Sullivan, K. Sumorok, J. Tang, Samuel C.C. Ting, S.M. Ting, P. Thomas, B. Wadsworth, M. White, S.X. Wu, B. Wyslouch, X.J. Yan, C.H. Ye, C. You, X. Zhang

The Charles Stark Draper Laboratory, Cambridge, Massachusetts, USA
R. Araujo, J. Barry, E. Berk, M. Fury, M. Hansberry, T. Hines, G. Holden, F. Nimblett, J. Paradiso, W. Toth, L. Wilk

University of Mississippi, University, Mississippi, USA
L. Cremaldi, J. Ferguson, S. Harper, J. Reidy, J. Zhang

Mississippi State University, Starkville, Mississippi, USA
L. Croft, B. Piercey

Jackson State University, Jackson, Mississippi, USA
F. Lott

Princeton University, Princeton, New Jersey, USA
M. Convery, P. Denes, D. Lea, P. Piroué, H. Sicotte, D. Stickland, D. Wright

Los Alamos National Laboratory, Los Alamos, New Mexico, USA
D. Alde, R. Barber, J. Boissevain, T. Carey, B. Cooke, R. Farber, P. Ferguson, V. Gavron, T. Goldman, R. Gupta, J. Kapustinsky, W.W. Kinnison, K. Lackner, A. Lapedes, D.M. Lee, M. Leitch, R. Little, T. Lopez, M. Mattis, G. Mills, E. Mottola, R. Prael, R. Ricketts, W. Rodriguez, V.D. Sandberg, G.H. Sanders, D. Sharp, R. Slansky, B. Smith, W. Sommer, G. Stephenson, D. Strottman, G.T. West, W. Wilde, W. Wilson, L. Winter

University of New Mexico, Albuquerque, New Mexico, USA
J. Ellison, D. Finley, S. Humphries, B.H. Wildenthal

Columbia University, New York, New York, USA
E. Aprile, M. Moulsen, R. Mukherjee, M. Suzuki

LeCroy Corporation, Chestnut Ridge, New York, USA
M. Gorrics, B. Manor, R. Sumner

Carnegie Mellon University, Pittsburgh, Pennsylvania, USA
I. Brock, A. Engler, T. Fergusson, R.W. Kraemer, F. Linde, C. Rippich, J. Smith, R. Sutton, H. Vogel

Brown University, Providence, Rhode Island, USA
M. Aryal, A. De Silva, D. Rossi, M. Widgoff

University of Tennessee, Knoxville, Tennessee, USA
S.C. Berridge, W.M. Bugg, G.T. Condo, Y.C. Du, T. Handler, H.J. Hargis, E.L. Hart, R. Kroeger, A. Weidemann

Memphis State University, Memphis, Tennessee, USA
D. Franceschetti, S. Jahan, W. Jones

Vanderbilt University, Nashville, Tennessee, USA
S. Csorna

Oak Ridge National Laboratory, Oak Ridge, Tennessee, USA
D.J. Alexander, J.B. Ball, F.E. Barnes, J.M. Barnes, M.L. Bauer, R.L. Beatty, J.A. Blank, L.A. Boatner, C.Bottcher, H.R. Brashear, C.R. Brinkman, T.J. Burns, J.G. Carter, B.C. Chakoumakos, M.M. Chiles, K.K. Chipley, J.E. Choate, L.G. Christophoruou, F.E. Close, H.O. Cohn, J.H. DeVan, T.H. Dunigan, M.S. Emery, H. Faides, P.J. Fogarty, A. Gordeev, T.A. Herrick, M.J. Hollis, D.T. Ingersoll, J.O. Johnson, J.W. Johnson, Y. Kamyshkov, H.E. Knee, R.J. Lauf, D. Lousteau, D.L. McCorkle, S.A. McElhaney, D.L McElroy, J.W. Moore, F. Plasil, R.T. Primm III, K. Read, M.J. Rennich, R.T. Santoro, A. Savin, T.E. Shannon, K. Shmakov, V.K. Sikka, T.P. Sjoreen, M.S. Smith, A. Smirnov M.R. Strayer, R.W. Swindeman, E. Tarkovsky, J.F. Wendelken, A. Wintenberg, C.Y. Wong, K.G. Young,

University of Utah, Salt Lake City, Utah, USA
M.Salamon

Howard University, Washington DC, USA
R.M. Catchings, J. Lindesay

Bulgarian Academy of Sciences, Sofia, Bulgaria
Institute for Nuclear Research and Nuclear Energy
D. Bourilkov, V. Genchev, I. Geshkov, V. Krastev, G. Sultanov, P. Yaidjiev

Bulgarian Academy of Sciences, Sofia, Bulgaria
Central Laboratory of Automation and Instrumentation
G. Antcev, L. Antonov, B. Betev, H. Dimitrov, V. Dimitrov, G. Filipov, N. Shivarov

I. Physikalisches Institut, RWTH Aachen, Germany
P. Blömeke, M. Buchholz, E. Goulig, H. Haan, K. Hilgers, W. Karpinski, H-H. Kleinmanns, O. Kornadt, W. Krenz, T. Lehmann, K. L. Lübelsmeyer, T. Meinholz, D. Pandoulas, J. Y. Pei, M. Röhner, K. Schmiemann, D. Schmitz, M. Schöntag, A. Schultz von Dratzig, J. Schwenke, G. Schwering, R. Siedling, M. Toporowsky, W. Wallraff, W. Xiao, Y. Zeng, J. Zhou

Central Research Institute for Physics of the Hungarian Academy of Sciences, Budapest, Hungary
Gy. Bencze, E. Dénes, E. Nagy, J. Tóth, L. Urbán

Tel Aviv University, Tel Aviv, Israel
G. Alexander, A. Beck, I. Cohen

INFN and University of Bologna, Bologna, Italy
G. Anzivino, F. Arzarello, G. Barbagli, G. Bari, T. Barillari, M. Basile, L. Bellagamba, D. Borscherini, G. Bruni, P. Bruni, L. Caputi, G. Cara Romeo, G. Castellini, M. Chiarini, L. Cifarelli, F. Cindolo, F. Ciralli, E. Colavita, A. Contin, M. Dardo, S. D'Auria, S. De Pasquale, C. Del Papa, F. Fiori, I. Fiori, F. Frasconi, P. Giusti, G. Iacobucci, I. Laakso, G. Laurenti, Q. Lin, B. Lisowski, G. Maccarrone, A. Margotti, T. Massam, R. Nania, V. O'Shea, E. Pallante, F. Palmonari, P.G. Pelfer, D. Piccioni, S. Qian, G. Sartorelli, M. Schioppa, M. Scioni, G.C. Susinno, R. Timellini, A. Zichichi

INFN and University of Florence, Florence, Italy
A. Baldini, E. Borchi, M. Bruzzi, R. D'Alessandro, P. Spillantini, Y.F. Yang

INFN and University of Milan, Milan, Italy
F. Allegretti, C. Furetta, R. Paludetto, S. Pensotti, A. Penzo, P.G. Rancoita, L. Riccati, A. Villari, L. Vismara

INFN, Naples and University of Naples, Naples, Italy
A. Aloisio, M.G. Alviggi, E. Brambilla, G. Chiefari, R. De Asmundis, E. Drago, V. Innocente, S. Lanzano, L. Merola, M. Napolitano, S. Patricelli, C. Sciacca

University of Rome, Rome, Italy
L. Barone, G. Basti, F. De Notaristefani, E. Longo, M. Mattioli, S. Morganti, S. Pizzini

Bucharest State University, Bucharest, Romania
T. Angelescu, N. Gheordanescu, A. Mihul, T. Tudor

Institute for Atomic Physics, Bucharest, Romania
S. Bercea, F. Cotorobai, A Schneider

Swiss Federal Institute of Technology, Zürich, Switzerland
H. Anderhub, J. Behrens, A. Biland, M. Dhina, R. Fabbretti, G. Faber, M. Fabre, K. Freudenreich, M. Haensli, H. Hofer, I. Horvath, E. Isiksal, M. Jongmanns, H. Jung, P. Lecomte, P. LeCoultre, J. Lettry, L. Li, X. Lue, M. MacDermott, M. Maolinbay, D. McNally, M. Pohl, G. Rahal-Callot, D. Ren, H. Rykaczewski, B.Spiess, H. Suter, J. Ulbricht, G. Viertel, H. VonGunten, S. Waldmeier, J. Weber, L. Zehnder

World Laboratory, Geneva, Switzerland
S. Aksouh, Q. An, R. Ayad, P. Baba, X. Cai, H. Castro, X-Y. Cui, M.T. Dova, E. Eskut, Q. Fan, J. Galvez, W. Hao, A. Hasan, T. Hernandez-Benavides, H.R. Hoorani, G. Hu, M. Kaur, R.A. Khan, N.S. Khokhar, V. Kumar, A. Kuzucu, E. Leon Florian, C. Li, Q. Lin, B. Lisowski, R. Liu, Y. Liu, C. Maidantchik, R. Malik, Y. Mi, Y. Mir, N-E. Moulai, M.A. Niaz, V. O'Shea, N. Ozdes, J. Qian, S. Qian, K.N. Qureshi, Z. Ren, F. Rivera, H. Rizvi, T. Ruan, R.K. Sehgal, J. Seixas, A. Sharma, P. Sharma, C. Solano-Salinas, L. Sun, A. Syed, P. Vikas, U. Vikas, M. Wadhwa, Y. Wang, Z.M. Wang, G. Xexeo, C. Xu, G. Yang, C. Ye, Q. Ye, J.M. You, K. You, Y. Zamora Garcia, M. Zeng, Z. Zhang, A. Zichichi

Institute of Solid State Physics, Chernogolovka, USSR
V.F. Gantmaher, V.A. Grazjlis, Yu.A. Ossipyan, I.F. Schegelev, V.B. Timofeev

Joint Institute for Nuclear Research (JINR) Dubna, USSR
A.A. Bel'kov, E. Belykova, I.V. Boguslavsky A. Cheplakov, A. Cheremukhin, S. Dolya, V. Dunin, Yu. Ershov, N. Fadeev, A. Feshchenko, I. Golutvin, N. Gorbunov, I. Gramenitsky, I. Ivanchenko, M. Kadykov, V. Kalagin, A. Karev, V. Karzhavin, M. Kazarinov, S. Khabarov, V. Khabarov, Yu. Kiryushin, D. Kiss, V. Krivokhizhin, V. Kukhtin, A.V. Lanyov, R. Lednicky, I. Lukyanov, V. Lysyakov, A. Makhankov, V. Minashkin, N. Nogaytsev, V. Odintsov, V. Perelygin, D. Peshekhonov, V. Peshekhonov, D. Pose, V. Prikhodko, A. Prokesh, A. Rashevsky, I. Savin, S. Sergeev, G.S. Shabratova, A.S. Shchelev, M. Shafranov, I. Shpak, A. Skrypnik, G. Smirnov, D. Smolin, V. Sviridov, A. Vishnevsky, G.A. Yarygin, Yu. Yatsunenko, O. Zaimidoroga, M. Zamyatin, A. Zarubin, V. Zhiltsov, E. Zubarev

Central Institute for Structural Materials "Prometei", Leningrad, USSR
V. Chizhikov, G. Karzov, V. Lavrukhin, V. Markov, N. Panfilov, A. Romanov

Efremov Electrophysics Equipment Institute, Leningrad, USSR
E. Bondarchuck, A. Chegodajev, A. Dedurin, N. Doinikov, S. Egorov, O. Filatov, V. Glukhih, V. Kuchinsky, V. Muratov, A. Roshal, G. Trokhachev, E. Zapretilina

Leningrad Nuclear Physics Institute, Leningrad, USSR
V. Andreev, A. Denisov, Y. Dokshitser, V. Ivochkin, V. Janovsky, A. Kaschuk, V. Khoze, A. Krivshich, P. Levtchenko, V. Mayorov, A. Nadtochy, V. Razmyslovich, Y. Ryabov, V. Samsonov, A. Sarantsev, V. Schegelsky, A. Schetkovsky, Y. Sokornov, A. Shevel, N. Smirnov, E. Spiridenkov, V. Suvorov, A. Tsaregorodtsev, G. Velichko, S. Volkov, A. Vorobyov, An. Vorobyov, Y. Zalite

Research Institute for Nuclear Studies of the Byelorussia State University, Minsk, USSR
M.A. Baturitsky, N.E. Chekhlova, S.V. Cherepitsa, V.A. Mosolov, N.M. Shumeiko, A.V. Soroko, E.F. Titkov

Bochvar All Union Institute for Inorganic Materials, Moscow, USSR
V. Drobishev, V. Filkin, N. Gryaznov, A. Nikulin, E. Plashkin, G. Vedernikov, G. Zelensky

Institute for Mounting and Assembling Technology, Moscow, USSR
O. Druzhilovsky, S. Stepanov

Institute of Theoretical and Experimental Physics, ITEP, Moscow, USSR
A. Arefiev, A. Artamonov, A. Babaev, V. Bocharov, A. Bolozdynya, S. Burov, N. Bystrov, V. Chernyshev, M. Chumakov, A. Dolgolenko, V. Dolgoshein, V. Efremenko, A. Epifanzev, V. Epstein, A. Fedotov, Yu. Galaktionov, V. Gemanov, P. Gorbunov, B. Gordeev, P. Goritchev, Yu. Gorodkov, E. Grigoriev, R. Gurin, V. Khovansky, Yu. Kirilko, A. Klimentov, Yu. Kornelyuk, A. Kouchenkov, V. Koutsenko, A. Kovalenko, S. Kruchinin, M. Kubantsev, A. Kunin, A. Kushenkov, V. Lebedenko, I. Makhlueva, A. Malinin, S. Mamontov, A. Maslennikov, A. Nikitin, N. Pankin, V. Plotnikov, V. Plyaskin, V. Pojidaev, A. Rozjkov, M. Ryabinin, I. Satsky, M. Savitsky, A. Selivanov, V. Semetchkin, V. Shamanov, P. Shatalov, S. Shevchenko, V. Shevchenko, V. Shoutko, E. Shumilov, M. Sokolov, S. Solomentzev, V. Tchudakov, I. Vetlitsky, V.A. Vinogradov, V.B. Vinogradov, I. Vorobiev, V. Zaitsev, O. Zeldovich, S. Zeldovich, N. Zvetkov

Kurchatov Atomic Energy Institute, Moscow, USSR
S. Barabanov, S. Belyaev, L. Bragin, N. Chernoplekov, T. Davlatyan, V. Drozdov, E. Golubev, E. Grishin, A. Imenitov, V. Karpov, I. Karpushov, E. Klimenko, A. Kochergin, V. Kruglov, V. Kulyasov, Yu. Kurojedov, A. Kuznetsov, S. Lelekhov, O. Lisutenko, Yu. Lisutenko, A. Malofejev, V. Manko, V. Martemyanov, N. Martovetsky, V. Martynenko, A. Matvejev, V. Mokhnatuk, E. Mukhina, A. Myagkov, S. Novikov, I. Ovchinnikov, S. Osetrov, V. Patrikejev, V. Podshibyakin, K. Polulyakh, G. Razorenov, N. Rodina. V. Ryabov, A. Safronov, M. Sedov, V. Selivanov, E. Shatny, M. Solodnev, S. Svertnev, S. Terentjev, E. Velikhov, P. Volkov, A. Voropaev, T. Vostrikova, M. Vyirodov, E. Vyisotsky, I. Zotov

Research Institute for Nuclear Physics, Moscow State University, Moscow, USSR
R.K. Dementiev, I.S. Filimonov, L.K. Gladilin, E.M. Leikin, I.V. Nadezdin, A.V. Nemitkin, N.P. Novokshanov, V.I. Rud', L.M. Scheglova, A.N. Solomin, E.A. Tchudakov

Zhukovsky Central Institute for Airhydrodynamics, Moscow, USSR
A. Becklemischev, A. Dzuba, Yu. Ilvin, N. Klockova, V. Panin

The Soviet-Netherlands Joint Venture "ELCOM", Protvino, USSR
S. Klimenko, V. Rykalin, P. Spiridonov

Institute for High Energy Physics, Serpukhov, USSR
N. Fedyakin, A. Kozelov, R. Krasnokutsky, A. Lebedev, S. Medved, Yu. Mikhailov, Yu. Pirogov, E. Razuvaev, R. Shuvalov, E. Slobodyuk, A. Vasiliev

Institute of Nuclear Physics, Novosibirsk, USSR
L. Barkov, A. Skrinsky, E. Solodov

Yerevan Physics Institute, Yerevan, Armenia, USSR
N. Akopov, A. Amatuni, Ts. Amatuni, R. Astabatyan, R. Avakyan, A. Avatesyan, G. Bayatyan, P. Galumyan, A. Hagomeryan, R. Kavolov, S. Kazaryan, S. Matinyan, G. Mkrtchyan, A. Oganesyan, J. Petrosyan, V. Pogosov, K. Shikhlyarov, A. Sirunyan, S. Taroyan, N. Ter-Isaakyan, G. Vartapetyan

Institute of Physics, Academy of Sciences of the Georgian SSR, Tbilisi
K. Ahabadze, D. Chkareuli, A. Djavrishvili, G. Dvali, L. Gabuniya, L. Hizanishvili, I. Iashvili, E. Ioramashvili, G. Leptukh, T. Lomtadze, N. Manjalidze, P. Petman, N. Roinishvili, M. Svanidze, E. Zadadze

Institute of Physics, Academy of Sciences of the Estonian SSR, Tartu
I. Ots, H. Uibo

Institute of High Energy Physics, Beijing, China
C. Chen, G.M. Chen, H.S. Chen, S.X. Fang, S.G. Gao, W.X. Gu, Y.F. Gu, Y.N. Guo, Y. Han, J. He, J.T. He, B.N. Jin, H.T. Li, J. Li, P.Q. Li, W.G. Li, X.G. Li, S.Z. Lin, Q. Liu, Y.S. Lu, Z.P. Mao, L.J. Pan, Z.M. Qian, G. Rong, Y.Y. Shuo, H.W. Tang, K.L. Tung, J.H. Wang, L.Z. Wang, R.J. Wu, Y.G. Wu, Z.D. Wu, R.S. Xu, Y.D. Xu, S.T. Xue, C.G. Yang, C.Y. Yang, K.S. Yang, H.W. Tang, Q.Y. Tang, Z.Q. Yu, B.Y. Zhang, C.C. Zhang, D.H. Zhang, L.S. Zhang, S.Q. Zhang, D.X. Zhao, M. Zhao, Z.P. Zheng, G.Y. Zhu, Q.M. Zhu, Y.C. Zhu, Y.S. Zhu, H.L. Zhuang

Tsinghua University, Beijing, China
J.G. An, X.D. Chai, H.M. Chen, Z.M. Chen, Y.M. Hu, Y.Z. Lin, W.D. Ni, R.C. Shang, S.D. Xu, S.J. Zhu

Institute of Atomic Energy, Beijing, China
H.L. Ding

Chinese University of Science and Technology, Hefei, China
H.F. Chen, Z.F. Gong, C.H. Gu, C. Li, Z.Y. Lin, W.G. Ma, C.R. Wang, X.L. Wang, Z.M. Wang, Z.Z. Xu, B.Z. Yang, J.B. Ye, X.Q. Yu, Z.P. Zhang

Shanghai Institute of Ceramics, Shanghai, China
X.L. Fang, P.X. Gu, J.K. Guo, C.F. He, G.Q. Hu, S.K. Hua, H.J. Li, J.L. Li, P.J. Li, Q.Z. Li, Z.L. Pan, D.Z. Shen, G.S. Shen, E.W. Shi, W.T. Su, X.X. Wang, Z.Y. Wei, Y.Y. Xie, L. Xu, Z.L. Xue, D.S. Yan, Z.W. Yin, X.L. Yuan, Y.F. Zhang, G.M. Zhao, Y.L. Zhao, W.Z. Zhong, R.M. Zhou

Tongji University, Shanghai, China
L.Y. Chen, J. Du, M. Gu, J. Wang, L.M. Wang, X. Wu, K.H. Xiang, W.H. Zheng

Zhejiang University, Hang Zhou, China
P.E. Feng, W.K. Gu, Z.X. Han, C. Jiang, J.P. Jiang, Y.X. Lu, Z.K. Lu, Y.H. Pan, J.X. Qia, J.Y. Shi, Y.X. Sun, Y.Y. Sun, R. Wang, S.G. Wang, G.M. Wu, K.S. Vhen, G.G. Ysng,

Shandong University, Jinan, China
M. He, M.H. Jiang, Y.H. Liu, L.M. Mei, X.L. Meng, C.R. Wang, N.J. Zhang

High Energy Physics Group, Taiwan, China
C. Chang, A. Chen, H.Y. Chen, W.Y. Cheng, S.S. Gau, Y.C. Gau, Y.Y. Lee, W.T. Lin, W.T. Ni, Y.D. Tsai, S.C. Yeh

Punjab University, Chandigarh, India
M.M. Aggarwal, J.B. Beri, J.M. Bhatia, P.M. Kohli, M. Kaur Singh, V.S. Mittra, S. Sood

Jammu University, Jammu, India
S.K. Badyal, Devanand, A. Gupta, V.K. Gupta, L.K. Mangotra, N.K. Rao

Saha Institute of Nuclear Physics, Calcutta, India
P.V.K.S. Baba, B.B. Baliga, U.K. Chaturvedi, R. Gupta, V. Kumar, M.K. Nandy, R. Ray, S.C. Saha, R. Sehgal, P. Sen, R. Shyam, M. Wadhwa

Tata Institute of Fundamental Research, Bombay, India
T. Aziz, S. Banerjee, S.R. Chendvankar, S.N. Ganguli, S.K. Gupta, A. Gurtu, A.K. Jain, P.K. Malhotra, K. Mazumdar, R. Raghavan, K. Shankar, K. Sudhakar, S.C Tonwar

Science and Engineering Research Laboratory, Waseda University, Japan
T. Doke, H. Ichinose, N. Ishida, T. Ito, A. Hitachi, T. Kashiwagi, J. Kikuchi, Y. Nagasawa, T. Nakasugi

Saitama College of Health, Saitama, Japan
K. Matsuda, E. Shibamura

Riken, Saitama, Japan
T. Takahashi

Changwon National College, Changwon, Korea
C.H. Hahn

Chonbuk National University, Chonju, Korea
J.B. Choi

Chonnam National University, Kwangju, Korea
H.I. Jang, J.Y. Kim, T.I. Kim, I.T. Lim, M.Y. Pac

Chungnam National University, Daejeon, Korea
H.Y. Lee

Dongguk University, Seoul, Korea
W. Namgung

Gunsan National University, Gunsan, Korea
J.Y. Ryu

Gyeongsang National University, Chinju, Korea
S.-K. Choi, K.S. Chung, S.H. Chung, I.-G. Park, J.-S. Song, C.S. Yoon

Kangreung National University, Kangreung, Korea
G.S. Kang, D.W. Kim

Kon-kuk University, Seoul, Korea
S.K. Oh

Korea Advanced Institute of Science and Technology, Daejeon, Korea
J.E. Kim, J.K. Kim, I.G. Koh, H.Y. Park

Korea University, Seoul, Korea
S.D. Chang, B.G. Cheon, J.H. Cho, C.O. Kim, T.Y. Kim, S.B. Lee, S.W. Nam

Kyungpook National University, Taegu, Korea
S.G. Jo, J.-K. Ko, E.W. Lee, S.-Y. Lee, M.-G. Park, T.S. Park, D. Son

Kyungsung University, Pusan, Korea
Y.M. Park

National Pusan Fishery University, Pusan, Korea
S.-H. Doh

National Teacher's University, Cheongju, Korea
S.N. Kim

Sangji University, Wonju, Korea
Y.Y. Keum

Seoul National University, Seoul, Korea
J. Kim

Sookmyeong Women's University, Seoul, Korea
J.N. Park

Taegu University, Taegu, Korea
D.S. Kim

Spokesperson: Samuel C.C. Ting
MIT-LNS, Bldg. 44
51 Vassar Street
Cambridge, MA 02139, USA
Telephone: (617) 253-5065
Fax: (617) 253-4100
E-mail: None.

Contents

FOREWORD

The L* Collaboration (≈1100 scientists from 99 institutions) submits this Letter of Intent to the SSCL to build an experiment to precisely measure e, μ, γ and jets.
Since the submission of the EoI, much progress has been made in R&D in all detector subsystems. Following the instructions of the director of the SSC Laboratory and of the Program Advisory Committee, the L* Collaboration has modified the design of the L* experiment and reduced the scope. The results of these efforts are:

- A reduction of the detector volume and weight by more than a factor of two from the EoI design
- Maintaining the original L* physics objectives
- A reduction of the total L* cost to below 492 M$ (FY90)
- An increase in flexibility of the detector to adapt to changing physics objectives and machine parameters; in particular to perform experiments at a luminosity of 10^{34} and higher
- Broadening the participation of foreign countries from Europe and from the Asia Pacific region with the total foreign contribution approximating half of the total estimated cost.

Some major developments for the L* Collaboration are:

1. The establishment of major national centers in the U.S. at Oak Ridge National Laboratory (for the Hadron Calorimeter and engineering coordination) and at Los Alamos National Laboratory (for the Central Tracker) and at Lawrence Livermore National Laboratory (for the Muon Chamber). Working together with 29 L* institutes and universities in the U.S. these national laboratories will be the focal point for the L* Collaboration.
2. The formation of the L* Collaboration in the USSR under the leadership of Academecians S. Belyaev, Yu. Ossipyan, A. Skrinsky, and E. Velikhov. The USSR L* group has 16 institutions specialized in high energy physics, in magnet design and construction, in precision instrumentation, and in material science.
3. The participation of the Bologna Group in L*. Under the leadership of Professor A. Zichichi, the Bologna Group has had a long record of success in large international collaborations. Examples are pioneering the experiments on $p\bar{p} \rightarrow \mu^-\mu^+$ (1962) and $e^+e^- \rightarrow e\mu$ (1967) to search for heavy leptons, the construction of Gran Sasso, the construction of HERA, and the creation of the LAA project at CERN to systematically develop instrumentation for experiments at LHC, SSC and Eloisatron. The Bologna Group's record makes it a most valuable participant in L*.
4. The formation of the Korea Center for High Energy Physics, under the leadership of Professor Jae Kwan Kim, incorporating a total of 19 universities.
5. The formation of the L* Collaboration in China involving 7 institutions.
6. The formation of the L* Collaboration in India involving 4 institutions.

In the following chapters we describe the L* experiment and the changes since the EoI.

I Physics Considerations

A Introduction

The Superconducting Super Collider will be a unique accelerator with $\sqrt{s} = 40$ TeV and a luminosity of 10^{33} cm^{-2}s^{-1} increasing to $> 10^{34}$ cm^{-2}s^{-1} later. The size, cost and construction schedule of an SSC experiment imply that the detector design must be flexible to effectively adapt to the evolving physics with minimum additional cost and appropriate to the timeframe in which SSC will be operating. While designing the experiment for LEP, L3, in 1981, we realized that the cost and eight-year construction time would mandate a design adaptable over the lifetime of LEP and beyond. Indeed, today L3 is the only detector that can be quickly modified to run at the future LEP Hadron Collider (LHC) at CERN.

With a similar long range view towards the SSC, the L* detector is designed with the following features:

1. **Good e, μ, γ resolution.**
2. **Ability to operate at 10^{34} cm^{-2}s^{-1}.**
3. **The option to operate at 2×10^{34} cm^{-2}s^{-1} and beyond.**
4. **The option to cleanly study e, μ and jets.**

B Physics Perspective

The past quarter of a century has witnessed many fundamentally important discoveries in elementary particle physics. These discoveries, which give us more confidence in the Standard Model, were all made by precision experiments of leptonic and photonic final states. Indeed, one is reminded of the following [1]:

1. The discovery of two neutrinos came from measuring μ and e final states.
2. The discovery of the J particle shown in Figure I.1, emerged from an experiment on e^+e^- final states with a mass resolution of 0.1% and a hadron background rejection of 10^{10}.
3. The τ lepton was discovered by measuring coincidence of μe in the final state.
4. The discovery of the P_c state by the DASP collaboration at DORIS in July 1975 from a very clear and elegant observation of 2γ transitions is one of the most important confirmations of the existence of charm quarks.
5. The Υ particle was discovered by an experiment with a μ pair mass resolution of 2%.(see Figure I.2.)
6. The proof that the J particle is indeed a bound state of $c\bar{c}$ quarks came from precision inclusive photon measurements with NaI crystals by the Crystal Ball group. The identification that the Υ particle is a bound state of $b\bar{b}$ quarks came from inclusive photon measurements by the CUSB, and

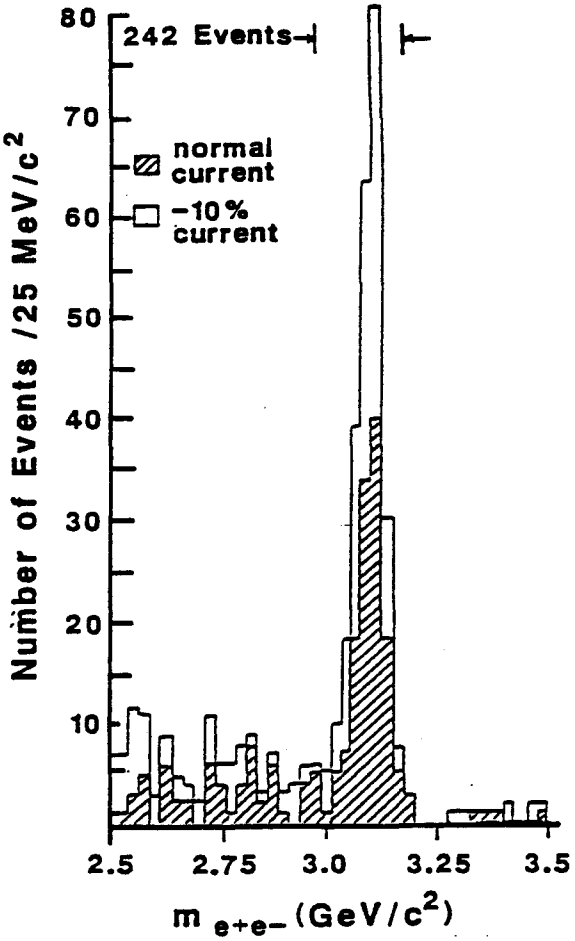

Figure I.1: The discovery of the J particle.

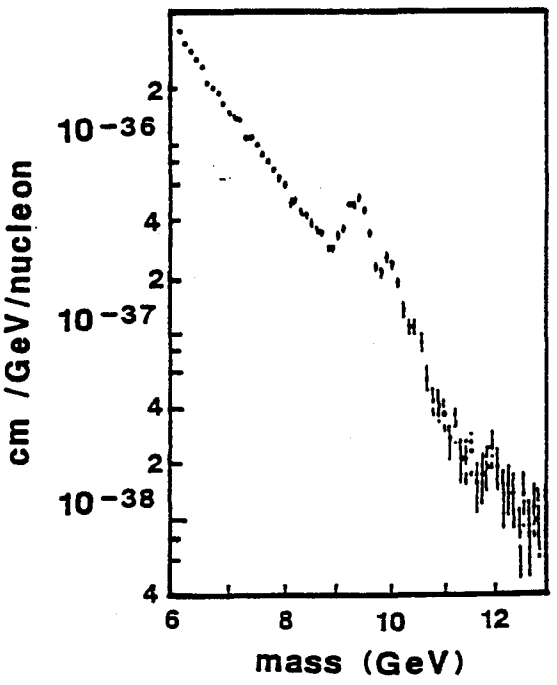

Figure I.2: The discovery of the Υ particle: Muon pair spectrum observed at Fermi National Laboratory.

CLEO groups as well as by the ARGUS and Crystal Ball groups.

7. The Z^0 particle was discovered with a large solid angle detector measuring e^+e^- and $\mu^+\mu^-$ final states.
8. The $W^\pm$ were found by measuring their large momentum single electron and muon decays.

These facts lead us to make the following observations:

(i) **These discoveries were not predicted when the original accelerators were constructed (the Z and W being the exceptions).**

(ii) **None of these discoveries were made by detecting hadronic final states.**

(iii) **The design for experiments at SSC energies ought to incorporate these experiences using precision detection capabilities for final states to perform definitive studies on heretofore unforeseen physics phenomena.**

C Experience in e μ γ Physics

Physicists in the L* collaboration have nearly 25 years of experience in developing the techniques to perform an experiment measuring γ, leptons and lepton pairs with high precision and large solid angle.

Table I.1 summarizes this learning process by the MIT group. The most important lesson learned in the 25 years of studying e,μ, γ is that in real experiments the background is always much higher than anticipated. This can be seen from our most recent study of the J particle production from 110,000 $Z \rightarrow$ hadron decays. Figure I.3 shows the $Z^0 \rightarrow e^+e^- + x$ spectrum where the e^+ and e^- are identified as isolated electromagnetic clusters in the BGO matched to a vertex chamber track. There is no evidence of a J peak. In Figure I.4 we add the requirement that the energy measured in BGO match the momentum measured in the vertex chamber. As a consequence, the background rate has decreased by a factor of $\sim$ 10 and a clear $J \rightarrow e^+e^-$ appears in the spectrum.

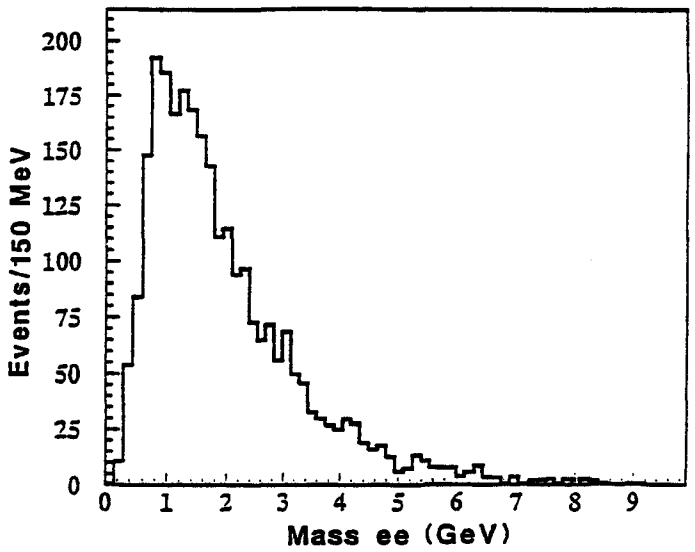

Figure I.3: Two electron invariant mass spectrum corresponding to 110000 $Z^0 \rightarrow$ hadrons events collected with the L3 detector at LEP. Electrons are identified as isolated electromagnetic clusters in the BGO matched to vertex chamber tracks.

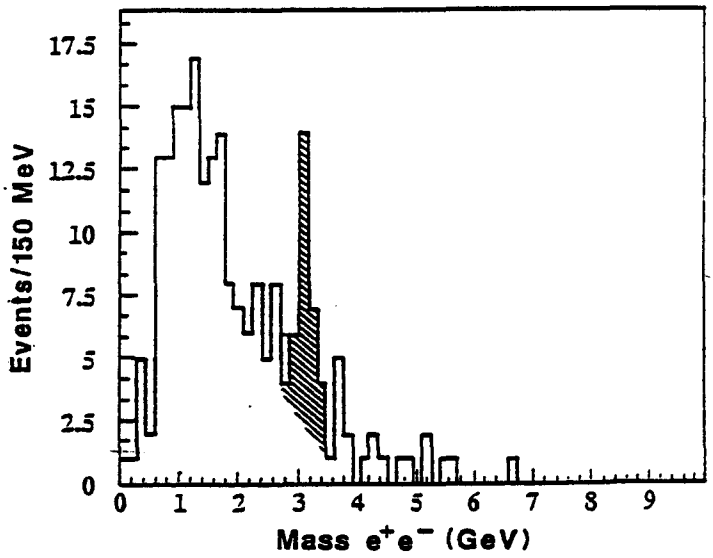

Figure I.4: The same as Figure I.3 but requiring also matching between the energy in the BGO calorimeter and the momentum from the vertex chamber for tracks of opposite sign. A signal coming from the decay $J \rightarrow e^+e^-$ appears.

References

[1] Phys. Rev. Let. 9, (1962) 36; Phys. Rev. Let. 33, (1974) 1404; Phys. Rev. Let. 35, (1975) 1489; Phys. Lett. 57B, (1975); Phys. Rev. Let. 39, (1977) 252; Proceedings of the 1981 International Symposium on Lepton and Photon Interactions at High Energies (1981) 165; Phys. Rev. Let. 49, (1982) 1612; Phys. Rev. Let. 51, (1983) 160; Phys. Rev. Let 52, (1984) 799; First report by ARGUS and Crystal Ball groups presented by P.M. Tufts in "Proceedings of the Symposium on Leptons and Photons Interactions at High Energies", Cornell, 1983; Phys. Lett. 126B, (1983) 398; Phys. Lett. 122B, (1983) 103;

[2] Becker, U. et.al., NIM 129 (1975), 593; Barber, D.P. et.al., Phys. Report 63(1987) 333.

Table I.1: 25 Years of Particle Physics Research

Experiments in e, μ, γ	Instrumentation for e, μ, γ
1964 at DESY $\gamma \to e^+e^-, QED, R < 10^{-14}$ cm, $\rho, \omega, \phi \to e^+e^-$, SU (3) In the process of checking the validity of quantum electrodynamics and studying leptonic decay of vector mesons, the DESY-MIT group developed techniques to measure leptons in a high intensity γ beam of 10^{11} per second. They obtained a rejection $ee/hh = 1/10^6$ and a mass resolution of $\Delta m/m = 1\%$.	
1972 at BNL $J \to e^+e^-$, New Quarks Based on the experience acquired at DESY, the MIT-BNL group designed a spectrometer able to measure lepton pairs in a high intensity proton beam of 10^{12} per second (equivalent to a luminosity of 10^{36} cm^{-2}s^{-1}) with $ee/hh = 1/10^{10}$ and a mass resolution of $\Delta m/m \approx 0.1\%$. This led to the discovery of the J particle.	**1972: High rate chambers** Very high-rate proportional chambers enabled us to run at BNL for three years with an extracted beam of 10^{12}ppp, leading to the discovery of J.
1977 at ISR $pp \to \mu^+\mu^-$, Scaling At ISR the CERN-Harvard–MIT-Naples-Pisa group designed an experiment with a 2π solid angle measuring μ-pair production with a luminosity of up to 10^{32} cm^{-2}s^{-1}. It measured $pp \to \mu\mu$ scaling precisely.	**1976: Large area drift chamber** Large area drift chambers with simple [2] I-beam field shaping enabled us to construct 800 m^2 of chambers for the ISR $pp \to \mu^+\mu^- x$ experiment, with a resolution $\sigma = 300$ μm. This type of chamber was also used at PETRA and SLAC experiments and improved in the UA1 muon chambers at CERN.
1978 at PETRA $e^+e^- \to Q\bar{Q}G$, Gluons, α_s, $e^+e^- \to \mu^+\mu^-$, QED, $R <$ 10^{-16} cm At PETRA the Aachen-DESY-IHEP-JEN-MIT-NIKHEF (MARK J) built a 4π calorimeter detector measuring electrons, muons and hadron jets. This experiment measured precisely muon pair asymmetry with a systematic error of 1%. The result confirmed the prediction of the Standard Model. At the same time, TASSO (Aachen, DESY and others) built the first modern large solid angle detector surrounding the interaction region with an excellent central tracking detector followed by an electromagnetic detector with good angular coverage. The work of the PETRA groups form much of the foundation of experimental support for our understanding of QCD.	**1979: Straw tubes** Thin wall drift tubes (now called straw tubes) with high rate capability operated in Mark J as vertex detector with a resolution of $\sigma = 250$ μm. **1978–1982: High precision chambers** The development of high-rate high-resolution (130 μm/wire) chambers for ISABELLE resulted in the multisampling precision drift chambers for L3. The coordinate resolution of < 50 μm and a specially designed and monitored support structure to < 30 μm enabled us to construct the precision muon detector of L3. **1989: R&D for the SSC** 1. Methods to build high resolution muon chambers covering 1000 m^2. 2. Best gas for these chambers operating in magnetic field. 3. High precision alignment systems and UV laser verification.
1983 at LEP: $\Gamma_{ee} = 83.3 \pm 0.8$ MeV, $N_\nu = 3.07 \pm 0.11, g_A = -0.499 \pm 0.003, g_V = -0.047 \pm 0.012$, $\sin^2\theta_W = 0.232 \pm 0.003$ At LEP, many physicists in this LoI participated in building a 4π detector, L3, with e, μ, γ resolution $\Delta p/p \sim 1\%$ at $p = 50$ GeV. So far, based on 1.1×10^5 in L3 it measured the E-W parameters $g_V, g_A, \Gamma_{ee}, N_\nu$, set a limit on $M_H > 42.1$ GeV, and measured the $B\bar{B}$ mixing $\xi_B = 0.178 + 0.049 - 0.040(\sigma$ effect). As in the case of the DESY experiments, the J, and the Υ experiments, the momentum of $\mu(e)$ are measured twice, first in the vertex chamber (P_V), and second, in the precision muon chambers (P_μ), or in BGO (P_e). The muon energy loss ΔE is measured by the sampling calorimeter which also monitors the hard photon radiation. Energy balance (1) is used to eliminate hadrons. $$P_V = \Delta E + P_\mu \quad \text{or} \quad P_V = P_e. \qquad (1)$$	**1980–1989: BGO** BGO crystals developed in the Shanghai Institute of Ceramics enabled the L3 collaboration to build the precision electromagnetic calorimeter (12000 crystals), measuring e, γ with an accuracy of $(1.3/\sqrt{E} + 0.5)\%$. **1989: BaF_2** Successful R&D on BaF_2 crystals by the L* Collaboration leads to BaF_2 as an excellent material for the electromagnetic detector in the high radiation environment at SSC.

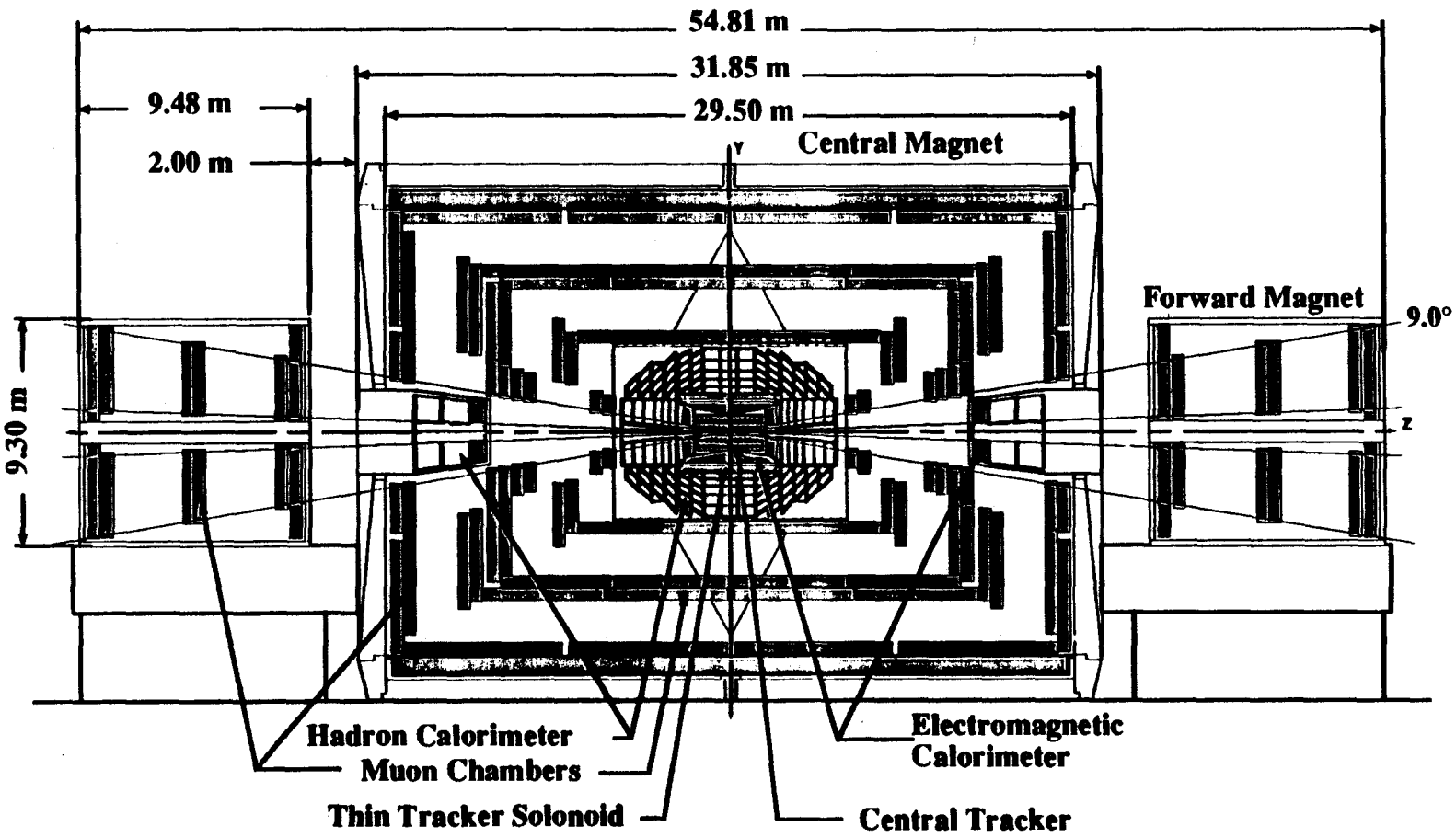

Figure II.1 L* Detector: Resistive Coil Side View

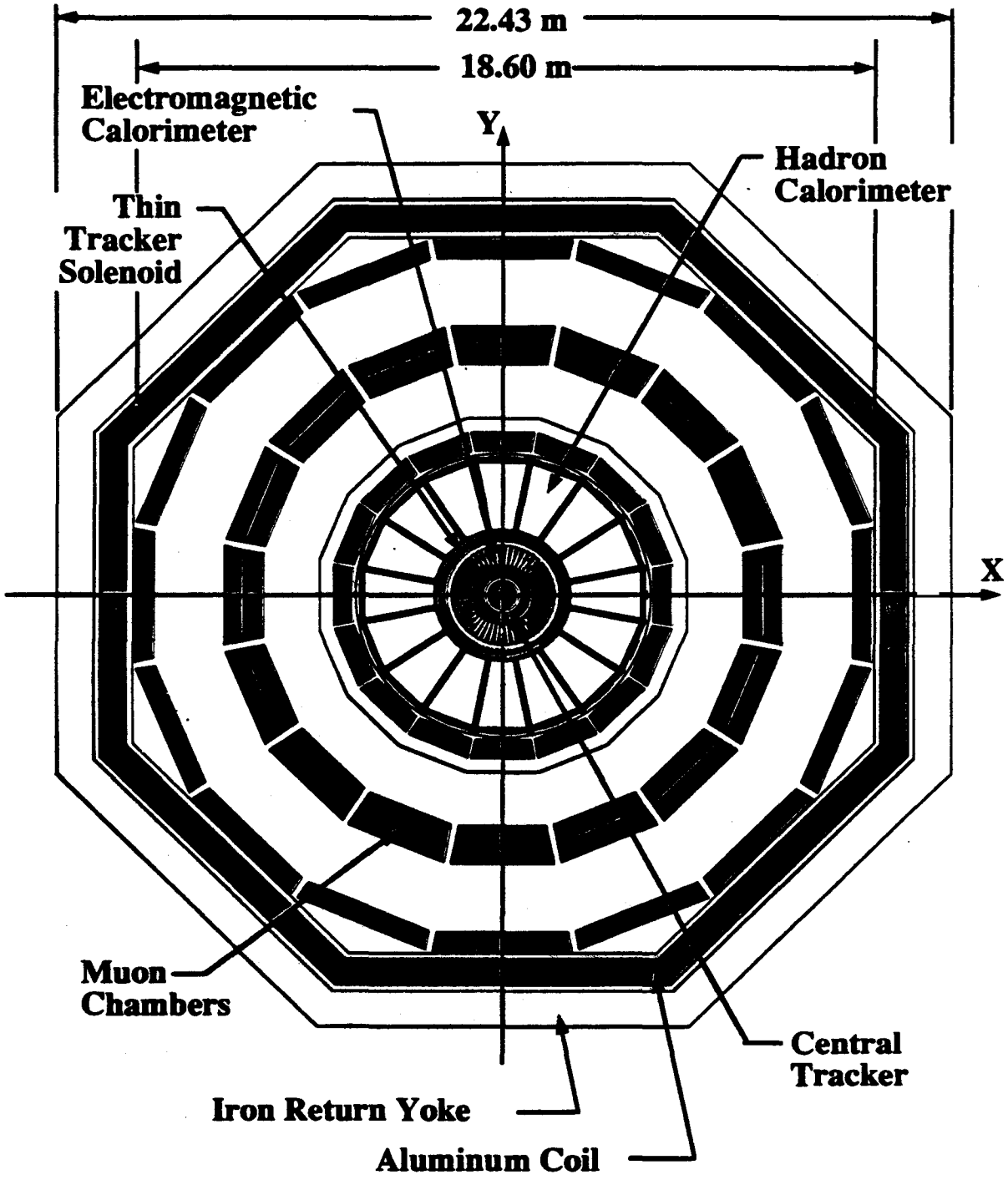

Figure II.2 L* Detector: Resistive Coil End View

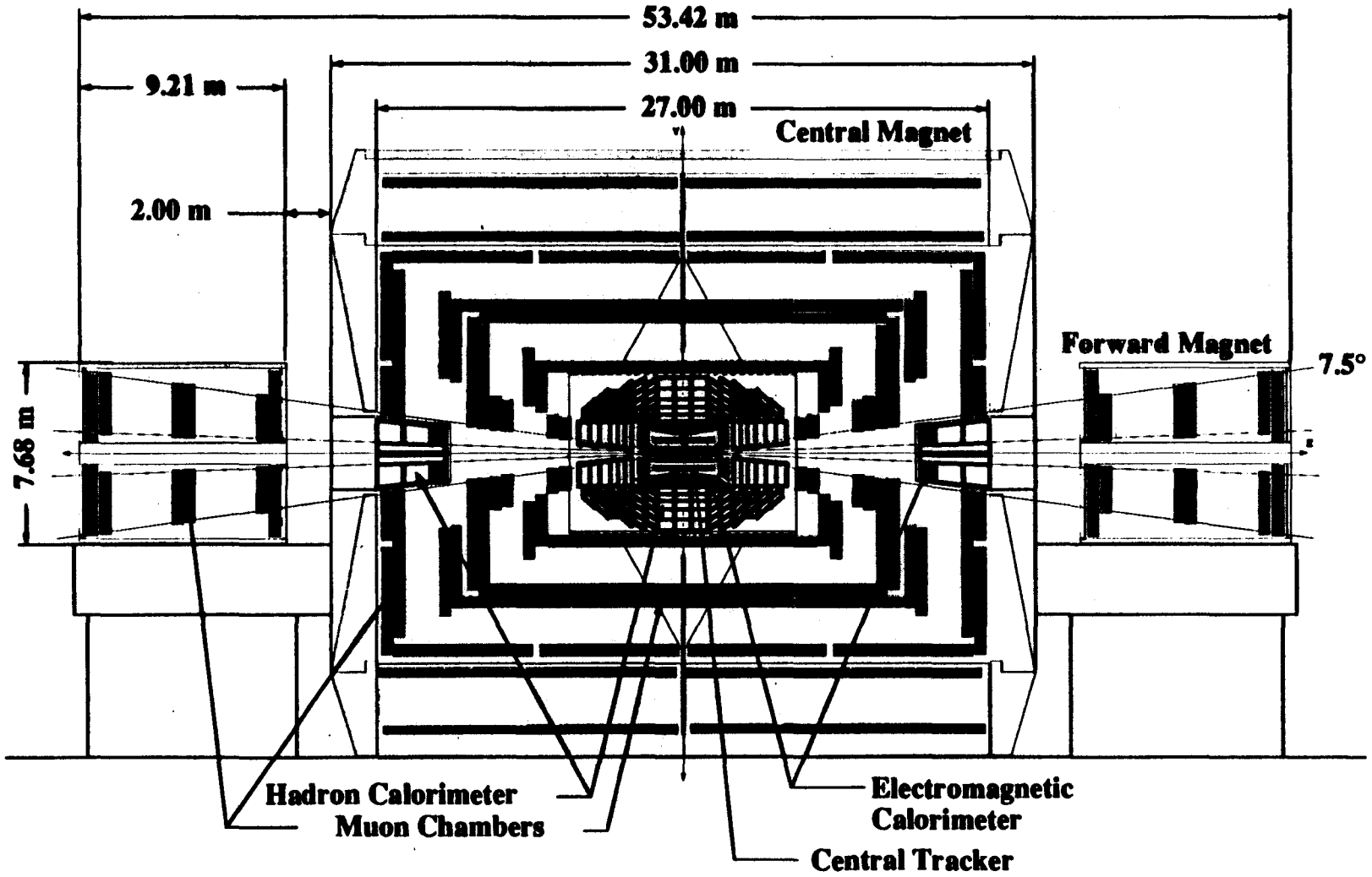

Figure II.3 L* Detector: Double SC Coil Side View

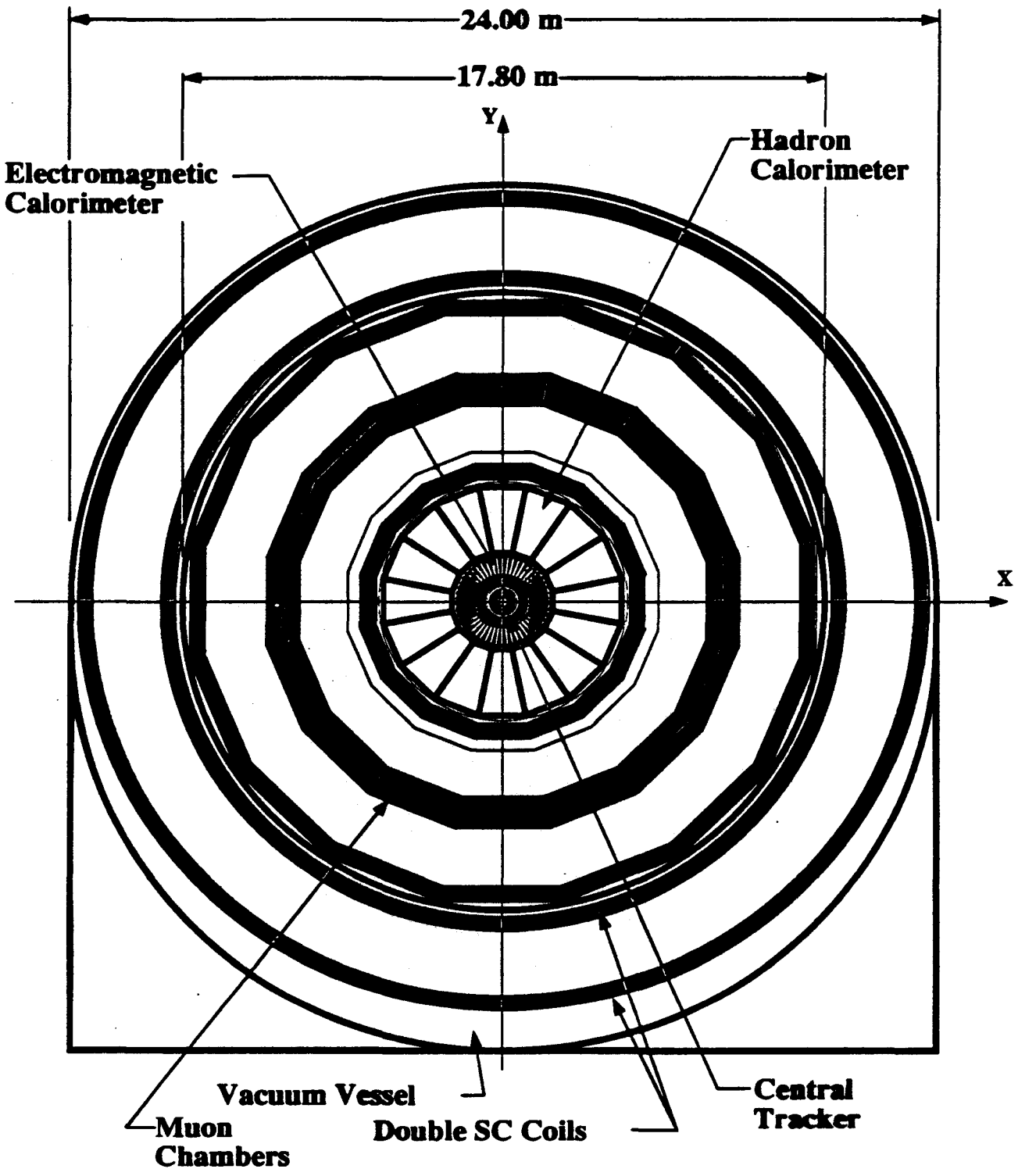

Figure II.4 L* Detector: Double SC Coil End View

II The L* Experiment

A Design Considerations

Following the advice of the Director of the SSCL and the Program Advisory Committee, the L* collaboration has conducted a comprehensive program of study to reduce the scope of L*. The physicists and engineers of L* have worked closely with a group of experts (the L* Internal Review Committee, LIRC) consisting of experienced project managers from Livermore National Laboratory, Los Alamos National Laboratory, Oak Ridge National Laboratory and Institute leaders from ETH, Zürich, from RWTH, Aachen, and from the Kurchatov Institute, USSR. The LIRC has made a detailed examination, often down to level 5 of the L* equipment cost, labor cost, contingency, EDIA, etc. All detector subsystems have undergone extensive R&D.

To downscope the detector in the most logical manner we have carried out the following procedure:

1. Analysis of the physics implications of:
   (a) Reducing the muon resolution from our EoI goal by redesign of the conventional magnet or by design of a new superconducting magnet of reduced cost.
   (b) Reducing the longitudinal sampling frequency of the hadron calorimeter and increasing the size of the sampling towers so that we reduce the total number of electronics channels.
   (c) Reducing the amount of BaF_2 by 1/3 by covering the forward region 6.7° – 2° with conventional detectors.
2. A detailed systematic study of magnet construction as functions of:
   (a) cost, weight, overall dimensions,
   (b) muon resolution,
   (c) power consumption,
   (d) assembly procedure and reliability in operation.
3. A reanalysis of the (EoI) muon chamber arrangement to reduce the total number of chambers. We have further reduced the number of electronic channels by linking sense wires.
4. An accelerated effort of R&D on the Hadron Calorimeter for scintillators:
   (a) to understand damage to the fiber,
   (b) to understand the uniformity of light collection,
   (c) to study scintillator tiles.

   and for the silicon detector options:
   (a) to elaborate large scale production techniques in the USSR, to reduce the cost by a factor of 10 or more,
   (b) to start a full thickness hadron calorimeter test.
5. Accelerated R&D effort on TMS for the Forward Calorimeter System including:
   (a) Radiation damage studies,
   (b) Fast detector response matched to the SSC,
   (c) Materials compatability with TMS,
   (d) Compensation
6. Accelerated R&D effort on BaF_2 for:
   (a) UV light transmission and suppression of longer wavelengths
   (b) production of crystals of adequate quality at low cost
   (c) control of radiation damage
   (d) development of readout diodes, and
   (e) development of an adequate calibration system.
7. Accelerated R&D effort on liquid xenon including:
   (a) mass production of liquid xenon,
   (b) purchase or lease of xenon,
   (c) supply from USSR,
   (d) light collection with adequate uniformity,
   (e) development of photodiodes, and
   (f) calibration.
8. A detailed redesign study of the central tracker to minimize the cost and radiation damage to the silicon.

The intensive R&D efforts have yielded the following progress on the L* subdetectors:

Magnet: Much R&D work was accomplished in the Kurchatov Institute on the double coil superconducting magnet. This work includes:

- completion of a 25 kamp superconductor,
- start of the production line of the L* 50 kamp conductor,
- detailed stress and structural analysis of the double coil design,
- detailed analysis of assembly sequence, flow, tooling, etc.

Muon Detector: The most significant results of the precision muon detector R&D effort since submission of the EoI are:

- The feasibility of manufacturing wire mesh cathode planes (to replace individual wires) to meet our required tolerances has been demonstrated.
- A chamber conceptual design and possible production method incorporating these mesh planes were determined.
- Mass production techniques are being determined.
- Systematic studies of gas for the L* muon system have identified a candidate gas which fulfills most of the L* requirements. A systematic approach for further study was developed.

- Structural design concepts for the central and endcap region have been completed including details of structure joints and structure and chamber mounts.
- A new radial design concept for the endcap region was devised and worked out. It is modular and allows precise alignment for momentum measurement, and reduces the number of chambers required.

Hadron Calorimeter: We have chosen the liquid scintillator, or scintillator tiles, as the first option, taking into account cost uncertainty in production of large quantities of silicon in the USSR and the progress we have made in scintillator R&D. For reasons of cost and increased radiation hardness, we have chosen TMS as the first option for the entire Forward Calorimeter system. In addition, we have selected liquid argon as a backup, should both scintillator and silicon detector R&D fail to meet critical milestones. Some of the interesting results on liquid scintillator R&D are

- Successful results in the study of chemical compatability of a liquid scintillator with wave-length shifting fibers. In the test two types of scintillator have shown either low or no chemical activity.
- The simulations of light yield and light collection by a WLS fiber were confirmed experimentally at ITEP.
- Complete Monte Carlo code simulating optical properties of combined scintillator and fiber system including light transport was finished. The simulation was performed and results on the uniformity of the light collection as well as on fiber geometry optimization were obtained.

Electromagnetic Calorimeter: Through the efforts of Shanghai and Beijing, we now have assurance that production cost for BaF_2 crystals is 2.5\$/cm^3. In addition, we have identified the Leningrad Nuclear Physics Institute as a backup supplier for large quantities of BaF_2, at 2.5\$/cm^3.
Shanghai and Beijing both have now produced L* size crystals with L* UV light transmittance requirement and light collection uniformity to $\sim$ 2%. Our systematic studies on BaF_2 radiation damage indicate that

- radiation damage in BaF_2 is saturated after $\sim$ 100 kRads, and
- it is caused by externally introduced impurities. By controlling the level of impurities, therefore, radiation hard crystals can be produced.

We are in the process of testing the new K-Cs-Te photocathode to suppress the slow component in BaF_2. An RFQ to calibrate BGO in L3 will be installed in February of 1991 which will enable us to learn how to calibrate BaF_2.
For the LXe detector we have made progress on the following:

- We have produced ϕ =5 cm UV photodiodes and fast amplifiers and tested them repeatedly. We can now produce them in large quantities.
- Tests with heavy ions on a 1 liter prototype detector show a $\sigma/E < 0.5\%$ for $E > 2.5$ GeV.
- Calibration with a source *in situ* agrees with heavy ion results.
- We have constructed two full L* type LXe cells which function properly.
- We are now sure the required quantity of LXe can be produced at $\sim$\$2.5/cm.

Central Tracker: Major R&D Results on the Central Tracker are:

Silicon:

- Radiation damage exposures of lithium niobate for optical modulators have been done at Los Alamos.
- Cooling ring prototypes have been fabricated.
- First silicon bridge prototypes fabricated and tested.
- Structural models have been verified. Bridge assembly behaves as if it was a single piece of silicon.

Straws: Radiation damage tests show no microscopic damage of wire and tube walls at 6×10^{14} n/cm^2.

Fibers: 3 commercial fiber types tested in reactor neutrons at 2×10^{13}, 2×10^{14} and 1×10^{15}n/cm^2. The measured attenuation length of 1 m is acceptable for use in L*. The first prototype PMT has been fabricated by Hamamatsu to L* specifications. Tests in a B-field are being set up.

B The Basic Design:

1. The magnet system consists of a central magnet and forward-backward magnets. The central magnet can be either of conventional design with aluminum coil with $B = 0.4$ T (Figures II.1 and II.2) or a superconducting coil with a superconducting return coil to replace iron, with $B = 0.83$ T (Figures II.3 and II.4). Both magnets can be installed in a hall with a width of 25 m. The F/B magnets are conventional with a field of 0.2 T.
2. The 4π precision muon detector provides a resolution at $p = 0.5$ TeV and $\theta = 90°$.

$$\left(\frac{\Delta p}{p}\right)_{\mu} = 4.9\%$$

for the normal magnet, or

$$\left(\frac{\Delta p}{p}\right)_{\mu} = 2.8\%$$

for the superconducting magnet. The F/B magnets extend the polar angle to $\theta = 2°$ with $\delta p/p = 5.0\%$.

3. A fast hadron calorimeter made of lead with liquid scintillator, or scintillator tile detectors covers the angular region down to $\theta = 5.7°$. The calorimeter response has a fast response and is constructed with a tower geometry pointing to the intersection region. Its resolution is

$$\left(\frac{\Delta E}{E}\right)_{\text{jet}} = \left(\frac{50}{\sqrt{E}} + 2.0\right)\%$$

A separate forward calorimeter covers the angular region from 6.7° to 0.3°.

4. For the normal magnet, the field of the central tracker is increased by 0.6 T to 1.0 T by a thin superconducting solenoid around it. A transport system has been designed to easily remove and exchange the central tracking chamber and electromagnetic detector for either high luminosity ($> 10^{34}$ cm^{-2}s^{-1}) runs or runs with additional hadron calorimetry replacing the electromagnetic calorimeter for jet studies.
5. A precision electromagnetic detector covers the angular region $6.7° < \theta < 178°$. It is made of BaF_2 or liquid xenon. The electromagnetic calorimeter provides an energy resolution of

$$\left(\frac{\Delta E}{E}\right)_{e,\gamma} \approx \left(\frac{1.3}{\sqrt{E}} + 0.5\right)\%,$$

and an angular resolution $\Delta\theta = 0.2°, \Delta\varphi = 0.2°$, with an e/π rejection $\approx 10^{-4}$. The combined electromagnetic and hadron calorimeter has a total of 12 λ_{int}, and the fine sampling allows us to track muons as well as to measure radiated photons.
6. The central tracking detector determines a 0.5 TeV particle with a resolution of $\approx 50\%$ to: (a) measure the momentum of e and μ from matching with precision e and μ measurements in specialized e and μ detectors, and (b) measure the multiplicity of charged particles surrounding e and μ.

Table II.1 is a summary of comparisons of the EoI design versus the current design.

In the following chapters, we describe in some detail the L* baseline design. Since the L* organization remains the same as described in the EoI (pp 81–82), it is not repeated here.

Table II.1: Comparison between EoI and LoI

	EoI	LoI
	Experimental Area	
Hall width	> 30 m	25 m
	Central Magnet	
Resistive:		
iron weight	48,200 t	20,300 t
coil weight	7,800 t	3,130 t
power	20 MW	12 MW
$\Delta P/P_\mu$	2.4%	4.9%
outside diameter	26.7 m	22.43 m
Superconducting:		
coil weight	4,000 t	1,704 t
outside diameter	30 m	24 m
$\Delta P/P_\mu$	2.4%	2.8%
	Muon Chambers	
electronic channels	223k	110k
Number of chambers	436	340
	Hadron Calorimeter	
Number of channels	335k	83k
	Electromagnetic Calorimeter	
Weight, BaF_2	83.6 t	61.5 t
Electronic channels:		
BaF_2	26,014	18,044
LXe	72,000	42,786
	Central Tracker	
Number of Si strips	3.7×10^6	3.2×10^6
Si readout channels	76k	5.1k
Number of straws	75k	52k
Number of fibers	50k	36k
Total Cost		< 492 M$

C Options

To exploit the true potential of the SSC at 10^{34} cm^{-2}s^{-1} and higher (2×10^{34} cm^{-2}s^{-1}), we use the fact that the base line design has a very large magnetic volume filled with precision muon chambers. Thus, it is relatively easy to

1. modify slightly the central tracker,
2. put in a new central tracker,
3. remove the central tracker and electromagnetic detector and surround the intersection region closely with a compact sampling calorimeter, or
4. replace the electromagnetic calorimeter with an enlarged central tracker which provides a much longer measurement arm to study inclusive lepton and jets.

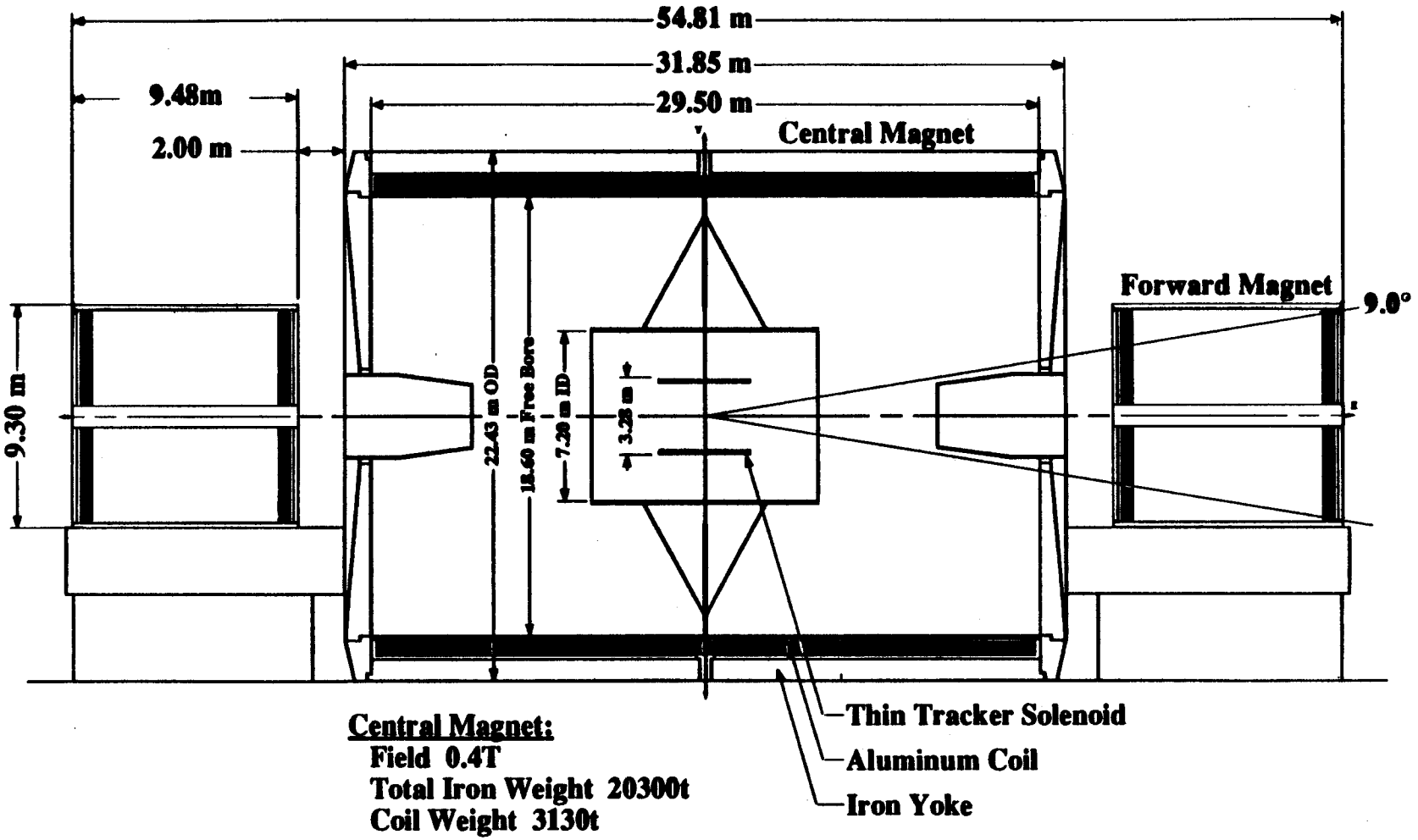

Figure III.1 L* Magnet System: Resistive Coil Side View

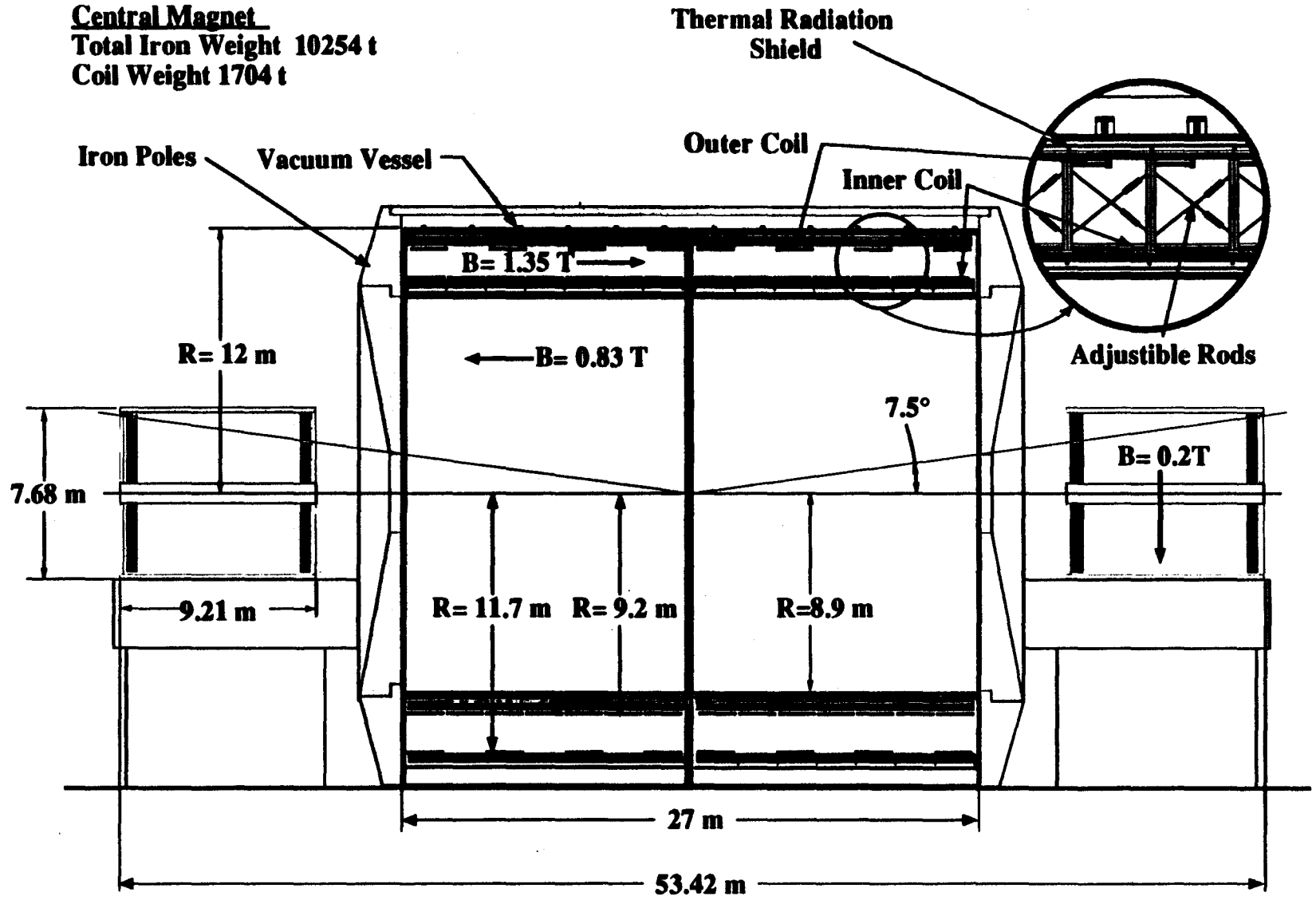

Figure III.2 L* Magnet System: Double SC Coil Side View

III Magnet System

A Introduction

The design concept of the L* magnet system remains similar to that of the EoI. However, to follow the PAC recommendations, the magnet system cost, size, weight and electric power requirements have all been reduced.

This system, based on the experience gained with the L3 magnet at CERN, consists of a large central solenoid oriented parallel to the beam axis and of two Forward/Backward (F/B) dipole magnets oriented perpendicular to the beam. With BL^2 as the performance figure of merit, a minimum system cost tends towards larger bore diameters and lower magnetic fields. For the conventional magnet this leads to a field of 0.4 T and for the superconducting (S.C.) magnet to a field of 0.83 T. Muon momentum resolution at 0.5 TeV and at $\theta = 90°$ is 4.9% and 2.8% respectively.

Two of the three concepts presented in the EoI for the central solenoid have been retained:

1. an aluminum coil with an iron return yoke
2. a superconducting coil surrounded by a second concentric, superconducting coil which replaces the iron return yoke.

Table III.1 displays the main central solenoid parameters for both options compared with the corresponding EoI parameters.

Table III.1: Main parameters for the two versions of the central solenoid.

Parameter	LoI	EoI	Unit
Resistive Coil Version			
Outside diameter	22.43	26.7	m
Magnet overall length	31.85	34	m
Total iron weight	20,300	48,200	t
Coil weight	3,130	7,800	t
Coil DC power	12	20	MW
Central field	.4	.75	T
Muon resolution	4.9	2.4	%
S.C.Double Solenoid			
Outside diameter	24	30	m
Magnet overall length	31	34	m
Coil weight	1,704	4,000	t
Refrigeration load at 4.5 K	2	3.5	kW
Central field	.83	.75	T
Muon resolution	2.8	2.4	%

The aluminum coil conceptual design has been proven in L3 and the corresponding L* magnet can be constructed with little R&D effort. The higher value of BL^2, the reduced electric power consumption and the lower weight are the main advantages of the superconducting double coil option. The two systems are shown in Figure III.1 and Figure III.2 respectively.

A design incorporating elements of both superconducting coil versions for the central solenoid presented in the EoI has been selected. The iron return yoke is replaced by a second superconducting coil. Iron poles are used to make the field homogeneous and to minimize fringe fields.

The redesigned S.C. system can be lowered into the experimental hall in two 850 t pieces, compatible with the 1000 t gantry crane anticipated to be available at SSCL.

The basic design of the F/B magnets (see Section E) remains unchanged. In the case of the central aluminum solenoid the polar angle acceptance coverage has been increased to $2° < \theta < 9°$. For the S.C. solenoid the coverage remains at $2° < \theta < 7.5°$, as presented in the EoI.

B Design Considerations

B.1 Resistive Coil Version

Parametric studies were performed to determine system performance (muon resolution) as a function of magnet size, weight, power and cost. The relationships of magnet outside diameter, magnetic field, power, cost and muon resolution are shown in Figure III.3, III.4 and Figure III.5.

As seen from Figures III.3 and III.4 0.5 T leads to a smaller outside diameter, but as seen from Figure III.5, this would rapidly increase the cost. Therefore, the selected design parameters of 22.43 m outside diameter, 12 MW electric power, and 4.9% muon resolution are

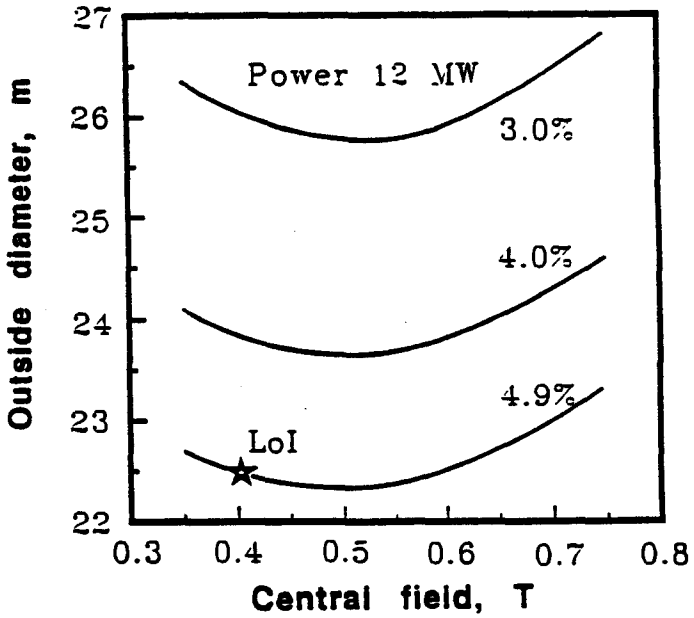

Figure III.3: Outside diameter versus central field for three values of muon resolution.

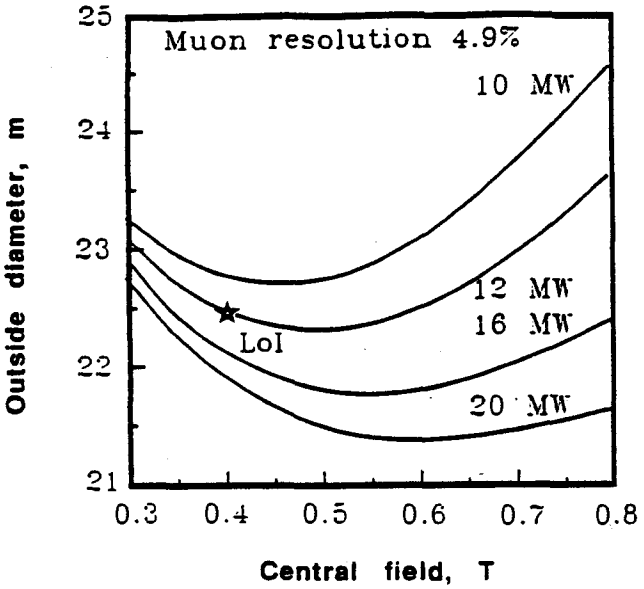

Figure III.4: Outside diameter versus central field and imposed power.

based on the combined consideration of magnet system design, cost, size of the experimental hall and SSCL facility requirements.

B.2 Superconducting Double Solenoid

Two superconducting options were presented in the EoI. In the first option a 90% reduction of the power consumption was achieved by replacing the aluminum coil with a superconducting coil. In the second option the iron return yoke is replaced with a second superconducting coil, thus also eliminating the large weight of iron. For this purpose a double S.C. solenoid option is proposed for the L* detector.

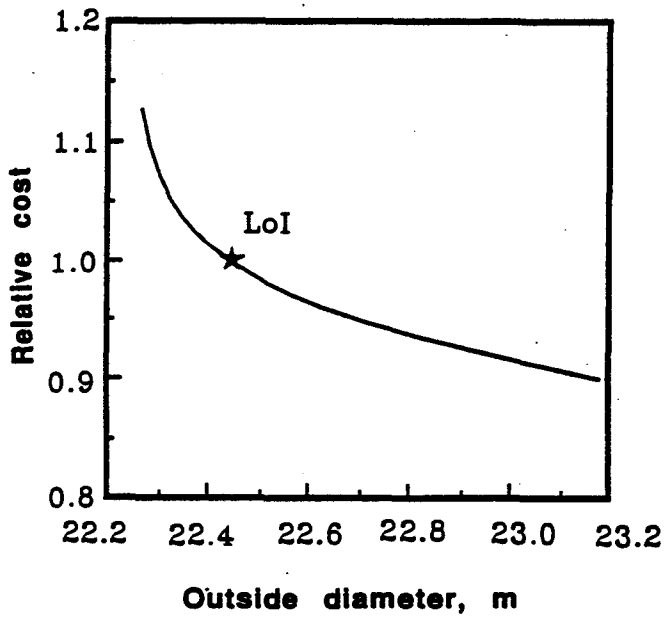

Figure III.5: Cost versus outside diameter of the conventional magnet.

In the EoI design field uniformity at the ends was provided by end compensation windings. For the LoI design iron plugs will be used to improve uniformity of the field. Although iron poles are substantially heavier than end compensation coils, they provide better access to the muon chambers, eliminate the need to warm up the coil for any manipulations with the chambers and ensure that stray field will be approximately zero.

Down scaling for the LoI has led to parameters for the double coil design which can provide a substantial improvement in resolution with lower weight and approximately the same cost as the conventional option.

Because electric power is not a consideration in the superconducting system optimization, it has been possible to increase the field strength and slightly reduce the bore diameter of the S.C. option compared to the EoI layout and significantly reduce the outside diameter of the magnet. As a result there has been only a small loss in resolution from 2.4% to 2.8%. The system parameters shown in Table III.1, above, represent a reasonable optimization between magnet cost and the experimental hall width.

As is the case with the conventional magnet, BL^2 scaling leads to lower magnet cost with larger outside diameter. These dependences are shown for BL^2 = 18.2 Tm^2 corresponding to 2.8% muon resolution in Figure III.6. The LoI design is slightly above the minimum cost because of constraints on the outside diameter. The return flux density in the annulus between the coils is somewhat higher than optimum resulting in more structure and superconductor.

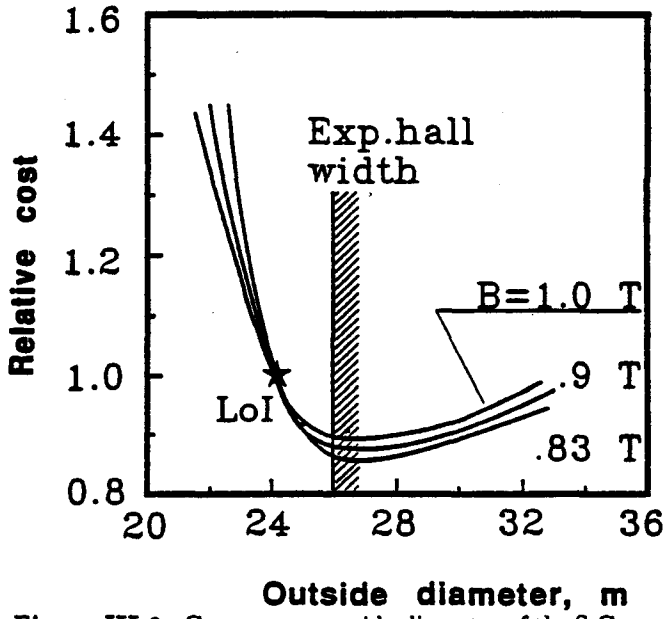

Figure III.6: Cost versus outside diameter of the S.C. magnet. Numbers at the curves indicate central field in the detector.

C Central Magnet with Resistive Coil

C.1 Coil and Iron Yoke

The general design is directly derived from the L3 concept and it is described in the EoI (Chapter III, pp. 10-15). Therefore only a short description of the magnet is given here. A cross section of the resistive coil system is shown in Figure III.1.

To form the solenoid, aluminum plates of about 8 m length, 0.7 m width and 9 cm thickness are welded together by electron beam into octagonal coil windings.

The internal volume of the magnet is protected from the heat losses of the coil by a thermal barrier consisting of 10 cm of inert thermal insulation and of an active thermal shield stabilized at a temperature of $20 \pm 1°C$, by a water cooling system.

The magnet cooling system is designed to remove the power dissipated by the main solenoid (12 MW) as well as by the two F/B magnets (0.75 MW each) together with their bus-bars (0.5 MW) and thermal shields. Since the main part of the magnet circuit is aluminum, it requires a separate, closed loop, low conductivity water (LCW) circuit cooled by the SSCL cooling system. A secondary loop will be derived from the main circuit to maintain the heat shields of the three magnets at a constant temperature. The power supply electronics is cooled by an independent LCW system. The coil is equipped with monitoring detectors to localize potential troubles during the assembly and the running periods. The monitoring system is described in the EoI p.12.

The iron return yoke is shown in Figure III.1. Design and construction of the iron yoke are similar to those of L3 and are described in the EoI(pp.12–14).

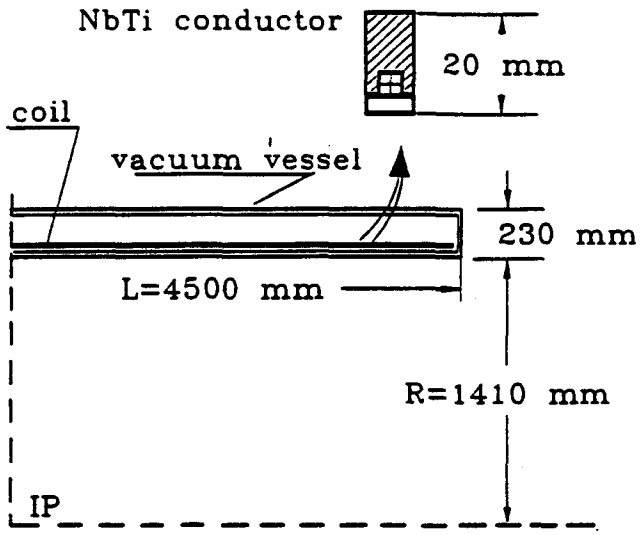

Figure III.7: Thin tracker solenoid section.

Table III.2: Characteristics of the thin tracker solenoid

Parameters	Value	Unit
Main dimensions		
Winding diameter	2,965	mm
Winding length	4,300	mm
Cryostat inner diameter	2,820	mm
Cryostat outside diameter	3,280	mm
Cryostat length	4,500	mm
Nominal current	13–21	kA
Critical current at 1.5T and 4.5K	42	kA
Generated field	0.6–1.0	T
Field uniformity	3	%
Inductance	0.1	H

C.2 Thin Tracker Solenoid

To improve the resolution in the Central Tracking Chamber (CTC), the central magnetic field will be increased locally by a thin superconducting solenoid, located between the electromagnetic and hadron calorimeters. The solenoid generates an additional magnetic field up to 1.0 T, which provides for the CTC a total field up to 1.4 T. The location of the thin tracker solenoid is shown in Figure III.1.

The cross section of the solenoid is shown in Figure III.7. It consists of a single layer winding with varying pitch to provide a linear increase in current density from the center to the end of the winding. The main characteristics of the solenoid are shown in Table III.2.

Figure III.7 shows the conductor cross-section as well; its parameters are presented in Table III.3. To provide high transparency, a Rutherford type Nb-Ti cable is stabilized by a copper clad aluminum strip and cooled by pressurized single phase helium in an attached rectangular tube. The conductor is wound in a machined helical groove on the surface of an aluminum alloy mandrel to provide precise location and rigid support of the windings. A glass fiber layer is wound outside the conductor winding to support the electromagnetic forces. At 90° the total amount of material is about 0.7 radiation lengths and the total radial thickness is 23 cm.

The solenoid and its cooled radiation shield are supported inside a vacuum shell with tie rods. The current and the refrigerants are fed into the cryostat through the radial gap between the central and end cap regions of the hadron calorimeter.

The combined field of the central solenoid and the thin tracker solenoid is shown in Figure III.8. The field uniformity in the region of the inner muon chambers is better than 5%. In the CTC volume the field uniformity is better than ±3%.

Table III.3: Parameters of the conductor for the thin tracker solenoid.

Parameter	Value	Unit
Conductor cross-section	8 × 20	mm^2
Nb-50wt%Ti wire		
Diameter	2.16	mm
Number of filaments	8,900	
Critical current (4.5 K, 1.5 T)	10,500	A
Number of wires in cable	4	
Cooling channel		
Tube cross-section	5 × 8	mm^2
Helium channel cross-section	3 × 6	mm^2
Total length	2,180	m

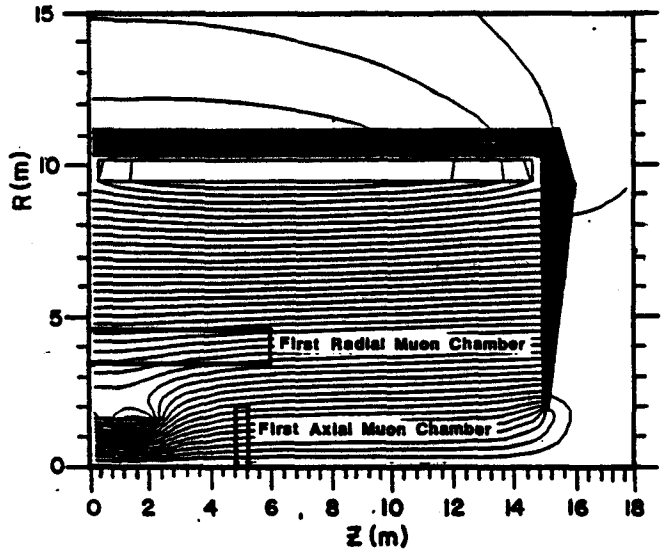

Figure III.8: Field map of the conventional magnet and tracker solenoid.

C.3 Assembly Sequence

The assembly procedure of the aluminum coil and the iron yoke is described in the EoI p.14. In comparison to the EoI design the assembly time is reduced by about 30% by decreasing both the coil and the iron mass. The area required for coil manufacturing is reduced in comparison to the EoI by about 30% and for the iron yoke manufacturing and storage by about 25%.

D S.C. Double Coil Solenoid

D.1 Magnet Design

The superconducting magnet system design is shown in Figure III.2 with its main parameters shown in Table III.4. There are two coaxial solenoidal windings with the fields directed in opposite directions. Ampere-turns are adjusted so that the total magnetic flux returns in the annulus between the two solenoids. As shown in Figure III.9 the superconducting magnet with iron poles also ensures a uniform field for precise muon momenta measurements. Axial electromagnetic forces act mainly on the warm poles instead of the winding which makes the winding performance reliable.

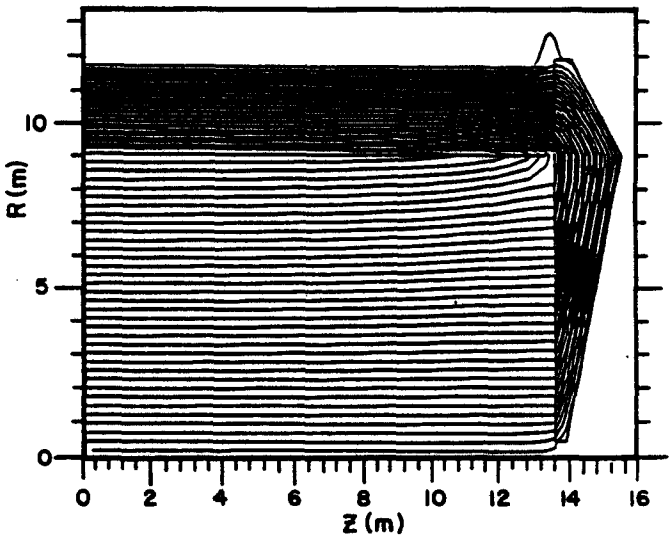

Figure III.9: Field map of the S.C.double coil magnet.

Table III.4: Main parameters of the superconducting magnetic system.

Parameters	LoI	Unit
Outer diameter	24	m
Total length	31	m
Length of the coil	26.6	m
Inner diameter of vacuum vessel	17.8	m
Length of one piece of the coil	13.3	m
Flux density in the annulus	1.345	T
Operation current	50	kA
Inductance	4.1	H
Stored energy	5.16	GJ
Refrigeration load at 4.5K	2	kW
Weight of the conductor	392	t
Magnet weight without iron	1,704	t
Total weight of the magnet	10,254	t
Weight of one piece of the coil	852	t
Conductor length	90.7	km

To simplify the assembly procedure the superconducting coil is divided into two parts separated by the central membrane. Each half is completed with its own separate cryostat. The weight of this magnet is supported by fiberglass columns. The relatively small axial force (less than 1000 t) is supported by tie rods.

The coil winding is shown in Figure III.2. The inner and outer windings are tightly attached to the aluminum alloy structural cylinders; both windings are inside the annulus. Because the field in the annulus is higher than

the field in the magnetic bore, it produces an outward pressure on the outer cylinder and a inward pressure on the inner one. The cylinders are connected to each other by tie rods made of the same aluminum alloy.

Structural design, checked by finite element analysis, shows excellent rigidity to ensure reliability during manufacturing, and for normal operation and for all emergency conditions. This design safety margin for both the conductor and the structural cylinders ensures conservative operation up to a field of 1.0 T.

D.2 Cryogenic System

Both the ALEPH magnet at CERN and MFTF-B magnet at the Lawrence Livermore National Laboratory have used the thermosiphon-cooling method, while many other fusion magnets use forced-flow cooling of the conductor. In the present design, both methods are used to combine their respective advantages to offer redundancy for higher reliability. The first cooling system uses the thermosiphon technique to cool the aluminum support cylinders to which the conductor is bonded. Natural convection-flow develops in vertical coolant tubes attached to the support cylinder. This cooling system is passive; it does not depend upon a refrigerator to maintain operation.

To greatly increase the thermal capacity adjacent to the current-carrying superconductor, a second circuit from the liquifier uses a straightforward forced flow cooling system that circulates single-phase helium. The detailed description of the cryogenic system is presented in the EoI p.22.

D.3 Superconductor

Parameters of the conductor for the L* central solenoid are presented in Table III.5. The superconducting strand is made of Nb-50%Ti with a superconductor to copper ratio of 1:1.5. The 23-strand cable is twisted around a stabilizer rod. It is assembled with two copper cooling tubes, into four copper-clad aluminum profiles that are soft soldered together with an additional rectangular stabilizer as shown in Figure III.10. The core of the conductor is a simple and direct extrapolation from the successful T-15 conductor for which more than 150 kilometers of high quality conductor were produced.

Figure III.11 shows the critical current density versus field at 4.2 K of such a conductor produced in the USSR. The operating temperature and the peak field in the winding are 4.65 K and 2 T respectively. The selected ratio of I_{op}/I_c for these conditions is 0.45 which represents a very conservative and reliable design. Presently 40 t per year of such niobium-titanium wire are produced in the Soviet Union. To serve the needs of the UNK and L* programs, the Kurchatov Institute has already obtained government approval to double the production rate. So that the 37.4 t needed for L* next year, can be easily obtained.

Table III.5: Parameters of the conductor

Parameters	LoI	Unit
Dimensions	30 × 46.6	mm^2
Length of one piece	880	m
Cross section of the channels	2 × 15	mm^2
Critical current at 5K in 2T	100	kA
Number of strands in the conductor	23	
Diameter of the strands	1.6	mm
Superconductor	Nb-50%wtTi	
NbTi:Cu	1:1.5	
Number of filaments	8,900	
Diameter of filament	11	μm
Stabilizer:		
Copper clad aluminum		
Residual resistance ratio		
for Al	500	
for Cu	50	
Cu:Al	1:4	

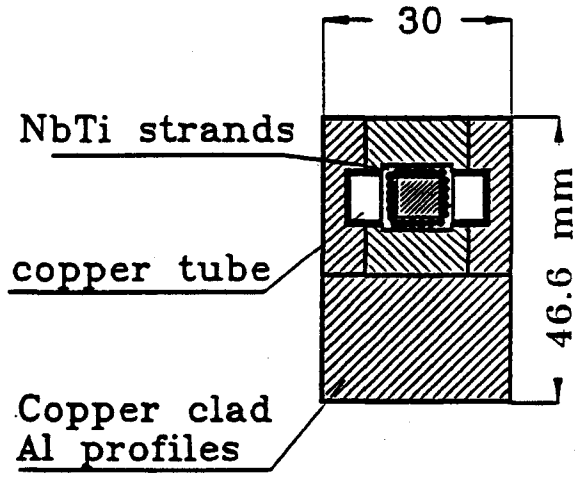

Figure III.10: Cross section of the conductor.

The finished conductor has a total stabilizer to superconductor area ratio of 74:1. This extreme conservatism ensures high stability and dependable operation. Aluminum stabilized conductor will have the same thermal expansion coefficient as the structure to eliminate any possibility of separation of the winding from the structure. The conductor allows a protection discharge with a characteristic time of 71 s and a dumping voltage of 1470 V, which guarantees that the hot spot temperature will be less than 100 K.

The aluminum stabilizer is readily available from the USSR industry. The USSR is one of the world's major producers of aluminum including aluminum conductor for power distribution and electrical equipment. Copper clad aluminum is a standard commercial product. Thousands of tons are produced yearly in a variety of sizes and shapes.

The conductor manufacturing procedure is reliable, inexpensive, and is standard throughout the world for

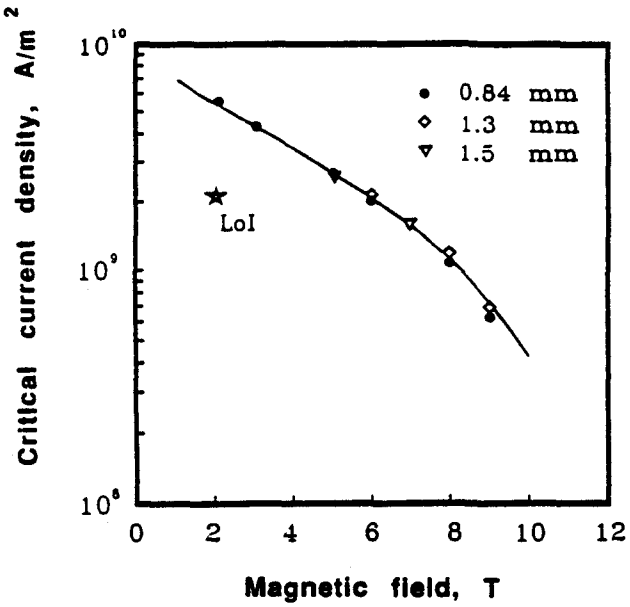

Figure III.11: Critical current density for 8900 filament Nb-Ti wires of different diameters.

joining superconductor cables to their stabilizing substrate. It may use either a copper-clad aluminum or copper stabilizing profiles. This method is widely used in the USSR, in particular for the routine production of conductor for MRI (Magnetic Resonance Imaging) magnets. Conductor similar to that proposed for L* with soldered copper stabilizer was produced in 1982 in the USSR and was successfully tested at the Kurchatov Atomic Energy Institute in model coils.

D.4 Magnet Manufacture

The large magnet dimensions require assembly on the SSCL site. The magnet will be built by Soviet engineers and technicians from parts and conductor assembled in the USSR, using tools supplied by the USSR. These parts will have a weight of 10 to 20 t with dimensions acceptable for transportation by truck. On site quality assurance in accordance with U.S. manufacturing standards will be provided by U.S. support engineers.

The manufacture and assembly will require a workshop 180 m long, 36 m wide and 30 m high where support cylinders and cryostats can be welded and coils manufactured. The inner and the outer coils will be assembled from 16 sections each. Support cylinders for each of the windings will be welded from the preassembled parts. After winding, the insulation and hydraulic tests will be carried out and the coils will be centered and secured by rods. The sections will then be assembled on the cold structure support, and will be enclosed in the cryostat with the liquid nitrogen cooled radiation shield and multilayer insulation. Attachment of the current lead box and cryogenic collectors and pipes will be followed by cryogenic tests and current tests at reduced current. Finally, tested halves of the superconducting coils will be lowered to the experimental hall, assembled with the end poles and fully tested.

D.5 R&D Program

Since all elements of the design have been demonstrated at moderate scale, the R&D effort will consist primarily of the manufacturing engineering, tooling development and verification at full scale. Parallel R&D will continue on the superconductor to optimize its performance in low fields. The major element of the verification test program will be a one half size (approximately 10 m winding outside diameter and 1 m coil width), full current (50 kA) model coil. This coil will be assembled and tested in the USSR, at the Kurchatov Institute. This program will verify all manufacturing operations and train the technicians who will build the magnet at the SSCL site. The test coil will closely simulate forces and mechanical stresses in the winding, structure and cold mass supports. It will provide a full scale demonstration of the conductor, length of cooling channel, current leads and supplies. The system controls, instrumentation, and protection scheme will also be demonstrated.

E Forward Backward Magnets

Forward and backward magnets are located at about ±18 m from the interaction point and have their magnetic fields perpendicular to the beam direction. This is well suited to the analysis of small angle particles. Angular coverage will be up to 9.0 degrees for the resistive coil version and 7.5 degrees for the superconducting one. Each has a 0.2 T field and requires 0.75 MW of power.

The main parameters of the F/B magnet for the superconducting version are given in Table III.6. The magnetic field inside the F/B magnets is vertical to ease the muon chamber manufacturing. The coil is split in two halves with a one meter gap to incorporate the last accelerator beam elements inside the F/B magnet.

Table III.6: Main Parameters of the F/B Magnet

Parameters	LoI	EoI	Unit
Current	13.17	16.3	kA
Coil total voltage	57	153	V
Central field	.2	.3	T
Free length along beam	7.0	9.22	m
Conductor section	37x6	30x5	cm^2
Conductor weight	176	200	t
Iron weight	625	1,755	t
Coil DC power	.75	2.5	MW

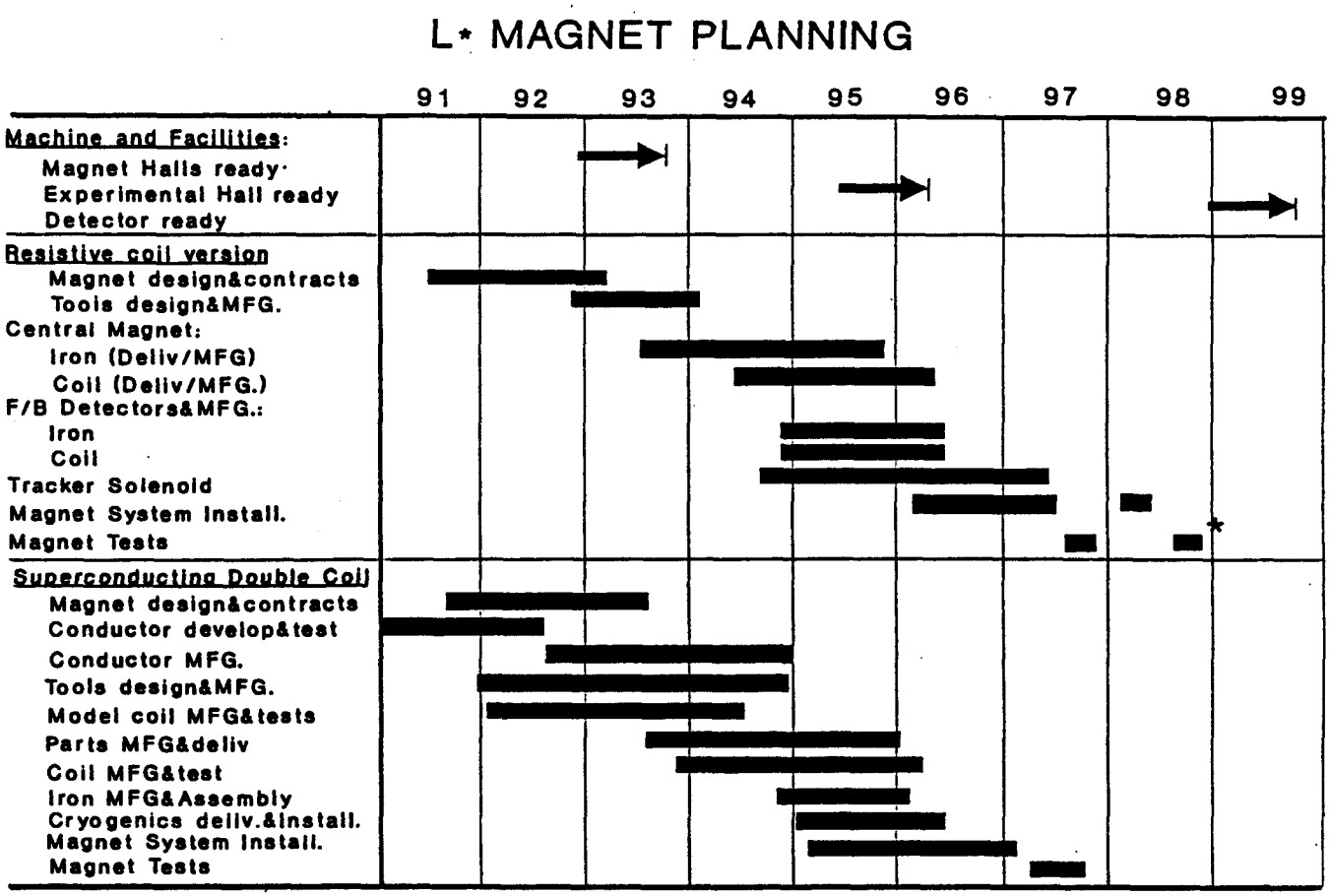

Figure III.12: Time schedule for the L* magnet construction. * Thin tracker solenoid test.

F Milestones

The schedules for assembly of both versions are presented in Figure III.12. The decision regarding which magnet type to build will be made at the end of 1991 after producing full scale conductor lengths and carrying out short sample tests at the Kurchatov Institute and at Lawrence Livermore National Laboratory.

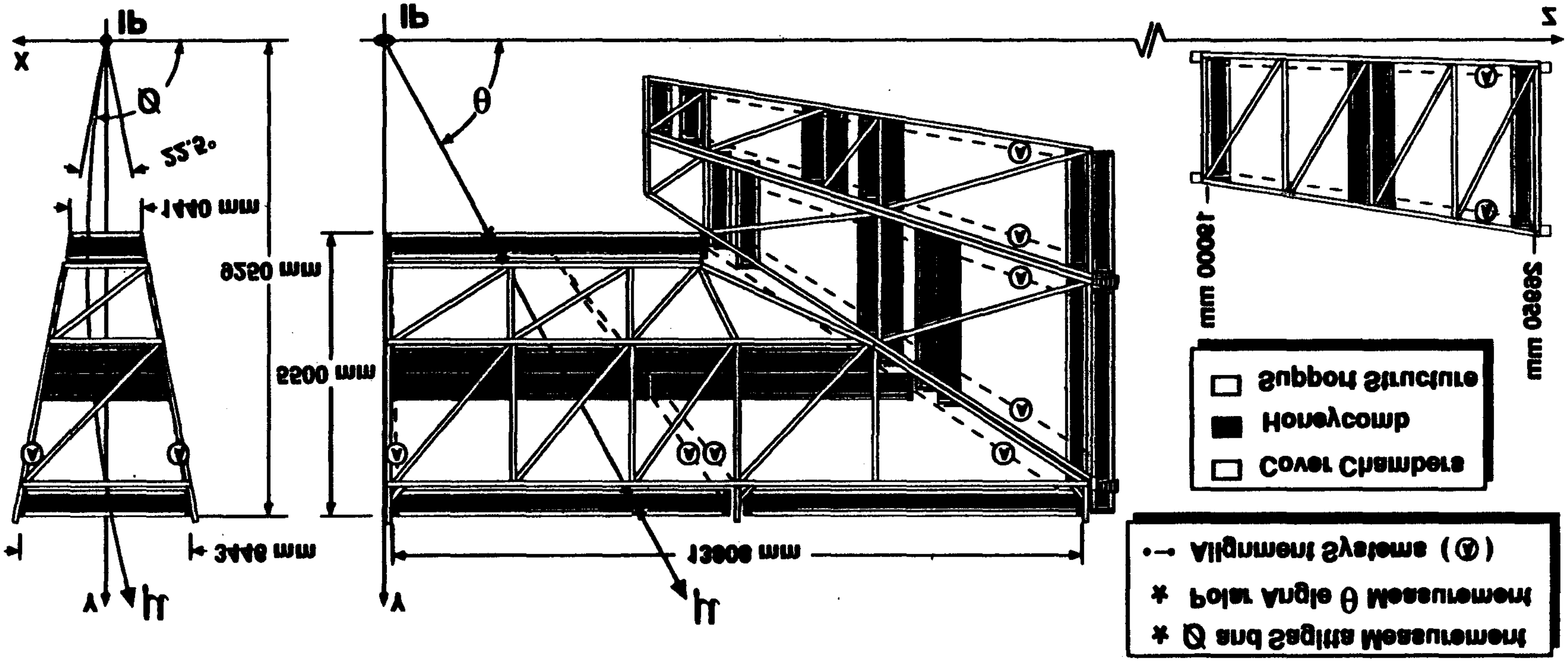

Figure IV.1 Sectional view of the L* Muon Detector

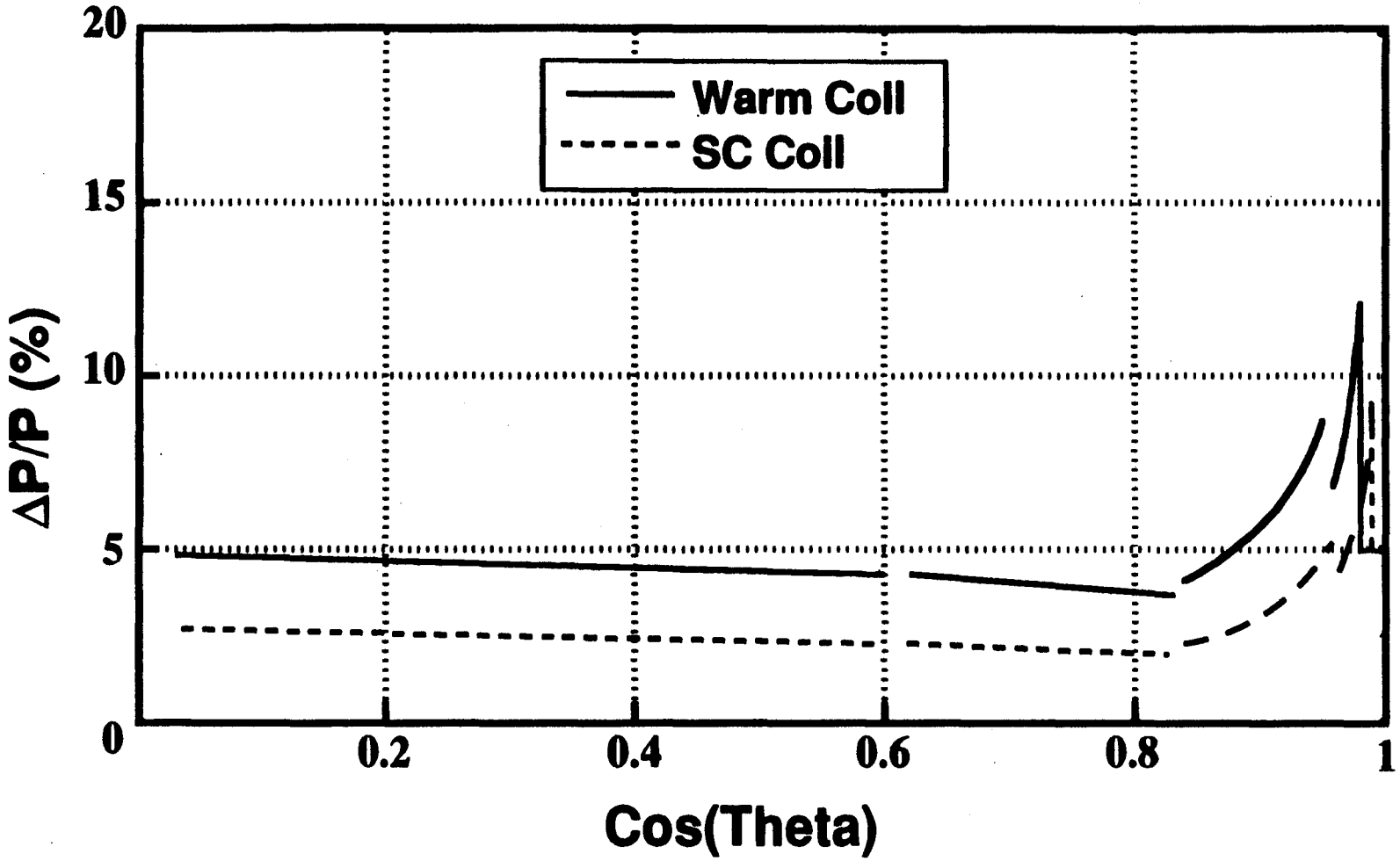

Figure IV.2 Momentum resolution as a function of cosine theta @ 0.5 TeV/c

IV MUON SYSTEM

A Introduction

The L* muon detector follows the principles and the experience proven in the L3 experiment and outlined in our EoI [1]. In response to the recommendations of the PAC both the design resolution and means for reducing the detector cost have been thoroughly re-examined. The muon detector proposed here, as shown in Figure IV.1, incorporates the following changes with respect to our EoI and to our Resource Requirement Report (RRR) [3]:

- Commensurate with the reduction in scope of L* we are proposing two possible versions for the muon spectrometer: one for a warm coil magnet with a field of 0.40 T and the other for a superconducting double coil magnet with a field of 0.83 T.
- The detector has been rearranged in the endcap region reducing the number of chambers by almost half, and allowing for a simpler support configuration.
- We have further reduced the number of electronic readout channels by linking sense wires together.
- We have reduced and postponed surface facility requirements at SSCL by assembling and testing large sections of the muon detector away from the SSCL.

The momentum resolution for 0.5 TeV/c muons at $\theta \simeq 90°$ is:

$$\Delta p/p = 4.9\%$$

in the warm coil version, and

$$\Delta p/p = 2.8\%$$

in the superconducting double coil version.

B Detector Description

The detector is symmetric about $\theta = 90°$. As shown in Figure IV.3, it is divided into a "central" region which covers from $32.9° \leq \theta \leq 88.1°$ and an "endcap" region which covers $9.0° \leq \theta \leq 32.4°$ in the version with a warm coil magnet and $7.5° \leq \theta \leq 32.4°$ in the version with the superconducting double coil. A "forward" region was detailed in the EoI (pp 33,39-40). It covers $2° \leq \theta \leq 9.0°$ in the warm coil version and $2° \leq \theta \leq 7.5°$ in the superconducting coil version.

The muon detector for the warm magnet is described below. Size and cost differences for the double coil magnet option are small.

The chambers in these three regions are arranged in modules. Within each module, the muon momentum is measured by three layers of precision multisampling drift chambers in the magnetic field. These modules allow the strict alignment tolerances necessary for precision momentum measurement to be met within one

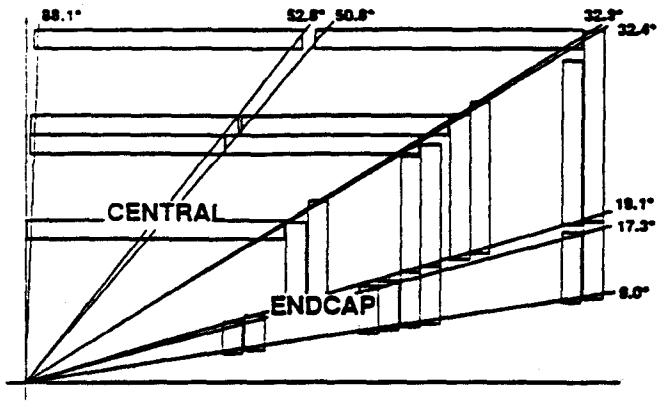

Figure IV.3: Side section of 1/4 of the detector.

structure. Muons with momentum greater than several GeV/c do not cross from one module to another.

The chamber wires are perpendicular to the muon bending direction, and measure the momentum component in the plane perpendicular to the beam. The first and third layers measure the track bending coordinate 32 times each and the middle layer measures the bending coordinate 64 times. Each of these 128 measurements has a single wire design resolution of 150 μm. We have shown [2] that these measurements are independent, so that the measurement of the bending coordinate in each layer improves as the square root of the number of measurements.

The figures show outlines of two chambers in the middle layer, which are mechanically joined as a single chamber for alignment purposes. The first 32 wires in the middle layer are offset by half a cell width with respect to the second 32. For legitimate tracks, the time sum of the measurements from the first and second sets of 32 wires must equal a standard value.

The polar angle, θ, between the muon direction and the beam axis is measured with less precise chambers (Figure IV.4). Their wires are roughly parallel to the bending direction, that is, perpendicular to the wires in the precision chambers. These "cover chambers" are double layered and are mounted as inner and outer cov-

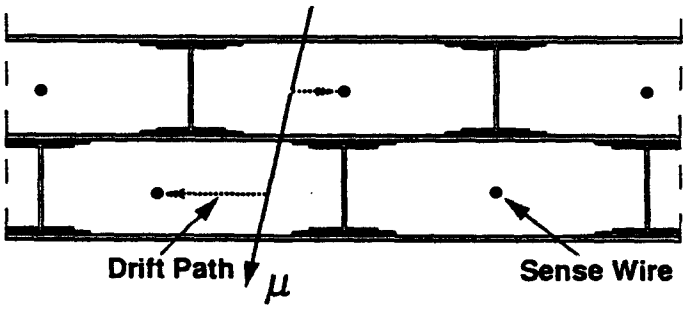

Figure IV.4: Cross sectional view of part of a cover chamber.

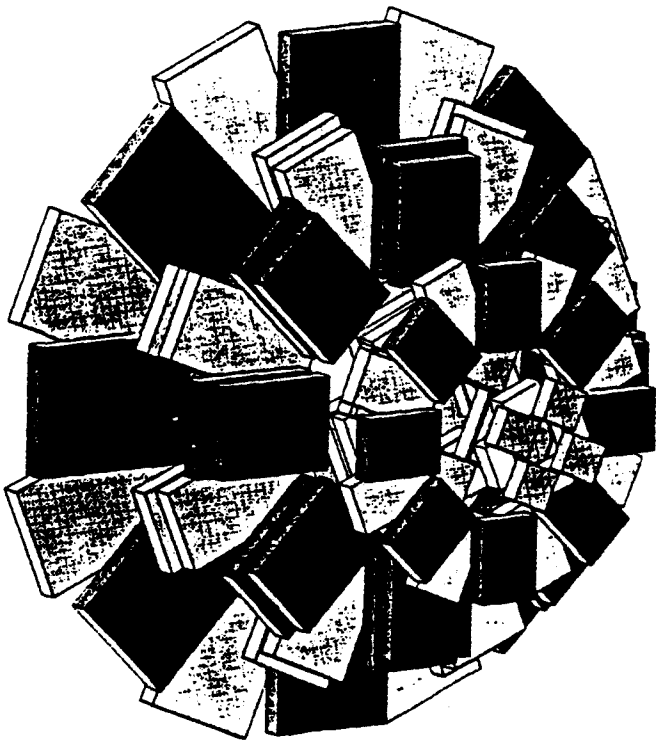

Figure IV.5: Radial arrangement of chambers in the endcap region.

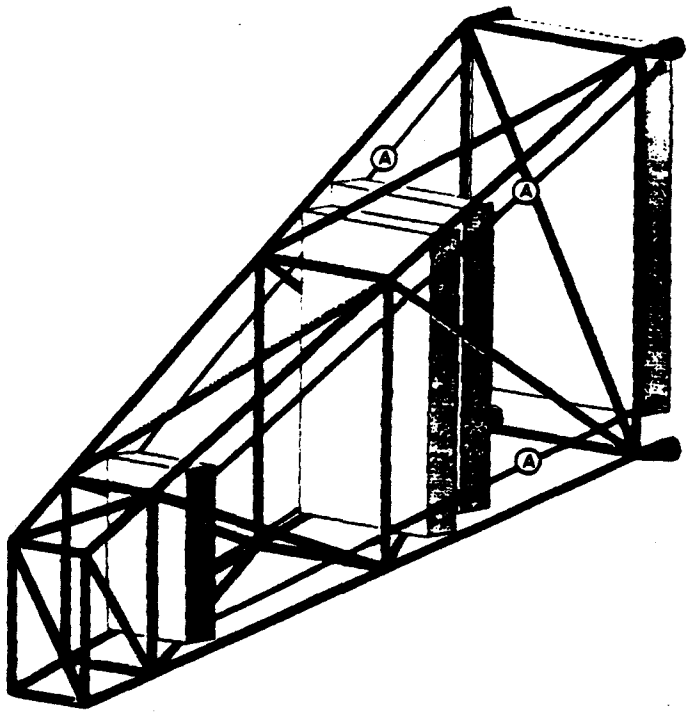

Figure IV.6: An Endcap Module. The lines denoted by (A) are alignment paths.

ers on the first and third layers of the precision chambers, measuring the non-bending coordinate of a track eight times. The chambers are constructed like the z-coordinate measuring chambers of L3. In these positions, multiple scattering produced by the cover chamber material does not significantly degrade the momentum measurement. To further reduce multiple scattering, the middle chamber passive covers are kept to the equivalent of 3 mm of aluminum by the use of low mass material such as honeycomb. The first level trigger is derived from resistive plate counters (RPC's) mounted on the chambers as described in the EoI (EoI p.35).

The central muon detector consists of 2×16 modules, as shown in Figure IV.1. Each module subtends $360°/16$ in ϕ, and from 32.9° to 88.1° (or from 91.9° to 147.1°) in θ. The modules contain five chambers each — one inner, two middle and two outer. The length of a module is 13.8 m.

In the endcap region we have chosen the radial chamber option (EoI p. 38). This version has substantially fewer chambers than the XY chamber option. The radial arrangement is shown in Figure IV.5. It has the principal advantage of being modular. An endcap module is shown in Figure IV.6. Each endcap module consists of two concentric cones of chambers arranged in a flower petal pattern, with wires nominally radial. As shown in Figure IV.3, on the plus-z side the chambers in the outer cone cover $19.1° \leq \theta \leq 32.4°$ and $\sim 360°/16$ in ϕ. Chambers in the inner cone cover $9.0° \leq \theta \leq 17.3°$ and $\sim 360°/8$ in ϕ. In both cones, alternate ϕ-sectors are stepped in z to provide full coverage with rectangular chambers (see Figure IV.5).

The forward detectors are shown in Figure IV.7. The wires are vertical, obviating problems from gravitational sag and resulting in less complex and less expensive chambers.

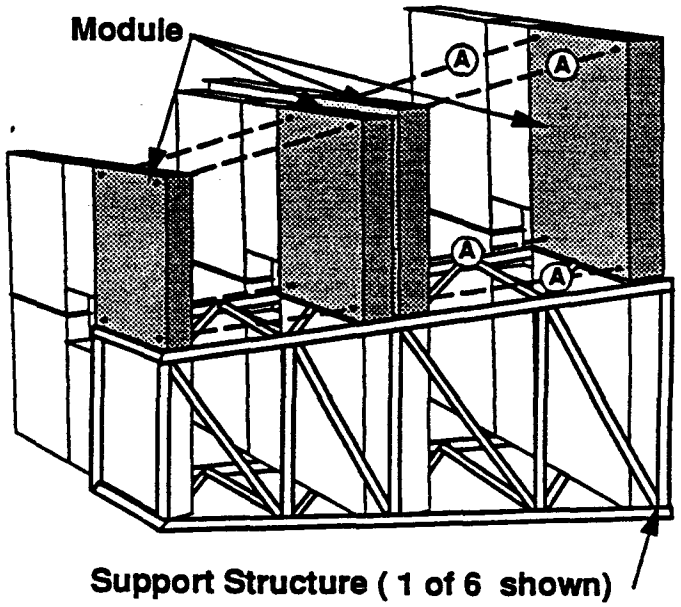

Figure IV.7: One of the forward muon detectors. The lines denoted by (A) are alignment paths.

The L* muon detector contains a total of 398 k sense wires. Since readout electronics and cabling constitute a sizable fraction of the detector cost, we will gang several sense wires into the same amplifier and readout chain to reduce the number of electronic channels to 110 k. This method was used in L3 to reduce the number of readout channels by a factor of two.

Figure IV.2 shows the resolution of the proposed muon detector at 0.5 TeV/c as a function of $\cos\theta$. The total solid angle coverage is more than 90% of 4π.

C Changes since the EoI

The changes described below are in response to the PAC's suggestions and also incorporate improvements and innovations from the ongoing R&D programs [5, 6].

In all regions we link precision wires by a factor of four to reduce costs. In the central region, for example, this linking reduces the number of electronic channels required by about 70%. In the endcap region the number of chambers is reduced from 80 to 48, due to the radial arrangement. These changes result in a reduction in the number of electronic channels, from 70 k to 41 k, with a corresponding reduction in cost. In the forward system we now plan active double-layer chamber covers for measuring the vertical coordinate.

Table IV.1 shows the most significant quantities affecting the cost of our current version as compared to the EoI configuration. We have reduced the L* SSCL resource requirements by adopting a plan to manufacture, assemble, and test most major muon system components off-site. We plan only to re-assemble and re-test these assemblies after transport to SSCL. This plan reduces the requirement for surface facilities at SSCL by more than 50%, resulting in cost minimization, relaxation of schedule requirements at SSCL, and reduction of schedule risk for L*.

Many improvements resulting from advances in the R&D program since the EoI are outlined in the following sections.

C.1 Chambers

The L* chamber design concept is shown in Figure IV.8. In order to maintain minimum technical risk, the R&D program is developing the required design early enough for verification prior to production. We are working toward incorporating automation and mass production techniques at the design stages, in order to maintain both minimum cost risk and minimum overall cost. Parts are being standardized and will be industrially produced in most cases.

Sense wire positioning, tensioning, and alignment must be done with a high degree of precision. Accurate wire positioning methods were developed for L3, and we are employing similar concepts for L*. Most importantly, the wires will be aligned by precision glass and carbon fiber bridges [4]. Tolerances of 5 μm can be maintained by the combination of precision bridges and the internal alignment system (see Figure IV.8 and Section C.4)

Studies to replace cathode wire planes by industrially produced mesh planes to increase chamber reliability have been carried out during the past year as part

Table IV.1: Muon System Inventory.

Parameter		EoI	Warm[a]	Cold
Number of Chambers				
Central	Inner	32	32	32
	Middle	64	64	64
	Outer	64	64	64
Endcap	Inner	80	48	48
	Middle	80	48	48
	Outer	80	48	48
Forward		36	36	36
Total		436	340	340
Thousands of Sense Wires				
Central		214	206	190
Endcap		215	153	145
Forward		55	39	39
Total		484	398	374
Thousands of Electronics Channels				
Central		127	58	53
Endcap		70	41	38
Forward		26	11	11
Total		223	110	102

[a] "Warm" refers to the option with a warm coil magnet, "Cold" refers to the superconducting double coil magnet option.

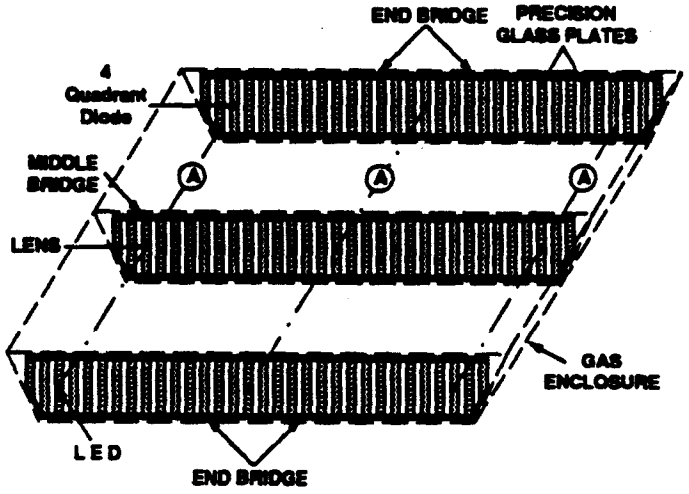

Figure IV.8: An L* multisampling outer chamber. The wires are aligned by precision glass and carbon fiber bridges similar to those in L3 [4]. Three bridges within a chamber are aligned with respect to one another by opto-electronic systems (A) consisting of a light source, a lens, and a quadrant photovoltaic detector.

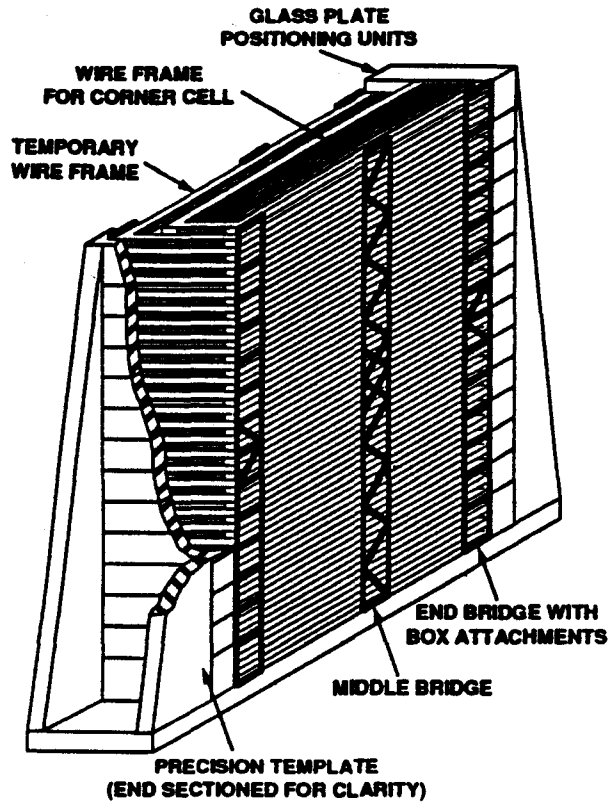

Figure IV.9: An L* muon chamber being fabricated by stacking wire planes in the template.

of the R&D program [5, 6]. Such a replacement reduces the number of wires by 60%. Incorporation of wire mesh cathode planes into the chamber design and chamber production process is underway. Several chamber production methods are under investigation, and optimization continues. One procedure for chamber manufacture is outlined below.

Wire mesh cathode planes will be mounted on temporary support frames at the factory. These frames will hold the cathode mesh and the sense wire plane. The temporary frames are loaded into a precision production template. Wire planes are precisely positioned, and then verified by a measuring system incorporated into the template (see Figure IV.9). Carbon fiber end frames are glued onto the wire support frames and wire positions are measured to verify the mechanical precision. The final chamber endframes and middle supports are created as a result of this process. This completed assembly precisely positions the wires, and maintains the wire planes in fixed positions after the template is removed. The central structure is surrounded by a frame which will support the wire tension and become part of the gas-tight outer envelope.

Wire loads are transferred from the support frame to the gas enclosure box through a flexible support structure. After the wires have been mounted in the gas enclosure, the temporary handling frames are removed and chamber covers are installed (see Figure IV.10). This construction method allows for an alignment procedure independent of the support frame, a low cost support structure, and minimizes adjustments during assembly and installation.

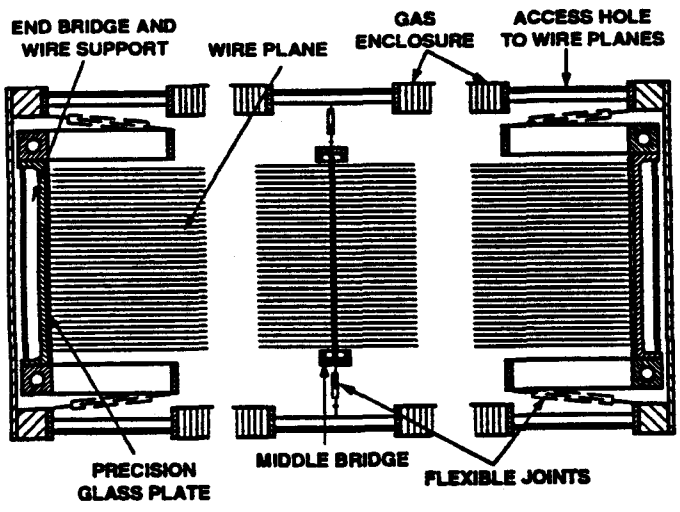

Figure IV.10: The completed wire plane assembly with carbon fiber bridges in the gas enclosure.

C.2 Gas

The L* muon detector gas must fulfill the following requirements:

- Insensitive to small changes in the electrical field or gas concentration.
- High accuracy by low diffusion.
- Non-flammable, since the volume is 2000 m^3.
- Sparkproof for reliable long term operation.
- Slow aging characteristics for long chamber lifetime.
- Small Lorentz deflection angle in the magnetic field.
- Affordable in the quantities needed.

An extensive R&D program has started. Most of the requirements are met by Ar:CO_2 mixtures, except for sparkproofness and slow aging. We have shown that these are significantly improved by the addition of isopropanol. Our present candidate gas for the chambers is Ar:CO_2:iC_3H_7OH in an 81:18:1 mixture at atmospheric pressure. Isopropanol largely suppresses the corona discharge seen in Ar:CO_2 mixtures. Figure IV.11 shows the drift velocity of electrons as a function of electric field E in different magnetic fields. At 1.8 kV/cm the drift velocity is insensitive to both the electric and magnetic fields. Figure IV.12 shows the deflection angle, α, due to the Lorentz force, as a function of electric field. Over this range of magnetic field strengths the angle is small and thus the contribution to the systematic error is minimal. Diffusion in Ar:CO_2 mixtures is known to be low, therefore we expect accurate operation. This gas is usable but not our final choice because the drift velocity is too sensitive to the CO_2 concentration. We have developed a systematic approach to determine the

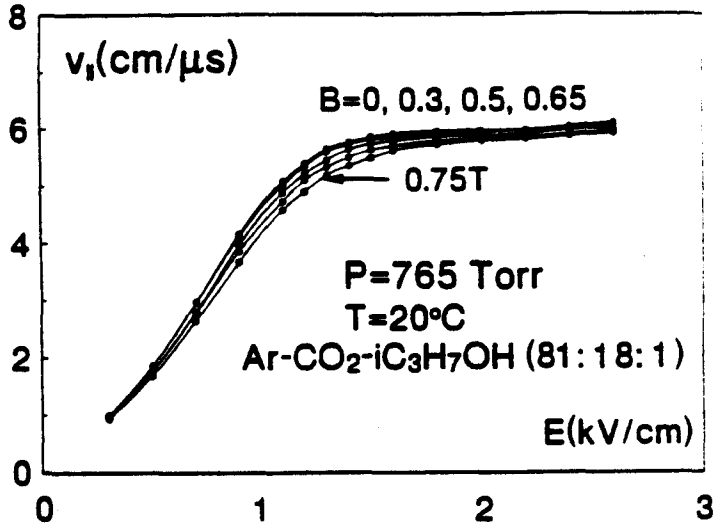

Figure IV.11: Drift velocity, v, as function of electric field, E, at various values of the magnetic field, B, for a 81:18:1 mixture of Ar:CO_2:iC_3H_7OH at atmospheric pressure.

improvement by admixtures and will pursue this in the R&D in the coming year [5, 6].

C.3 Structures

The design of the muon chamber structural support is essentially the same as described in the EoI (pp. 37-40). It remains a modular design based on the concept of a full truss composed entirely of aluminum. The selection of aluminum was confirmed after careful examination of alternative materials. These examinations compared our present design concept, where temperature variations are monitored and corrections are applied accordingly, to a design concept which would be relatively free of perturbation due to thermal disturbances. The effects

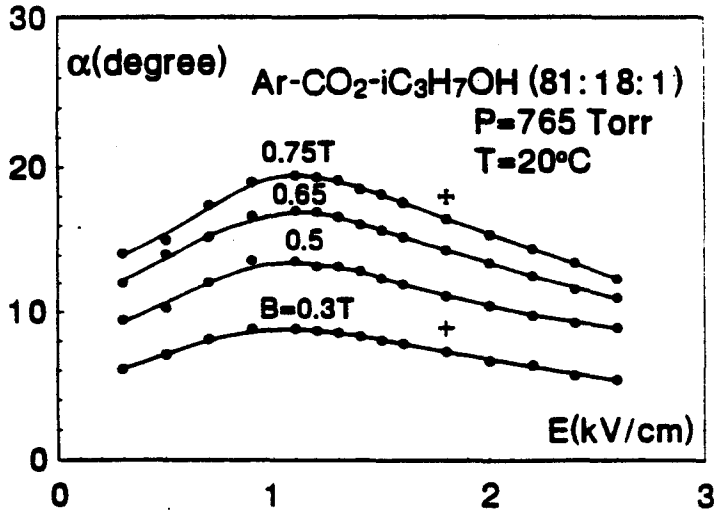

Figure IV.12: Lorentz angle, α, as function of electric field, E, at various values of the magnetic field, B, for the same mixture as in Figure IV.11. Crosses mark the operating points for the warm and cold magnet options respectively.

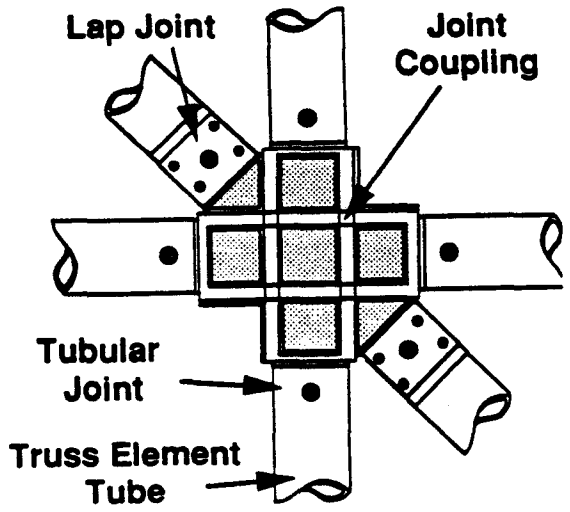

Figure IV.13: A Truss Joint Assembly

of thermal perturbations could be suppressed by the use of low thermal coefficient of expansion (CTE) materials, specifically carbon fiber epoxy or metal composites.

Many factors led to our decision to use aluminum for the support structure. Of major importance were the following:

- Linear Deformations — The present design concept (all aluminum, including chambers) provides isotropy of mechanical properties (CTE, Young's modulus, yield and strengths). Carbon fiber elements introduce the potential for asymmetric deformations and differential motions.
- Dimensional Stability — Carbon fiber composites show short and long term stability problems in our required range of accuracies due to moisture absorption.
- Cost — We estimate that a structure incorporating carbon fiber composites would at least double the cost. Even with the use of composites we would still require alignment monitors.

The key features of the design for the supporting structures in all regions are:

Truss Joint Assembly: The critical elements of the truss structure are the tube joints, which must be elastic and have low stress. This joint is used many times throughout the structure, and must be easily manufactured and inexpensive. The truss joint assembly is shown in Figure IV.13, and a cross sectional view of the tubular joint is shown in Figure IV.14. The joint is precisely located with a pin and strengthened with epoxy.

Removable Truss Elements: Chamber removal during fabrication and maintenance requires that the structure have removable struts that can be reinstalled precisely. A relatively inexpensive lap joint has been designed and is shown in Figure IV.14. This joint is also used to facilitate the initial structure assembly.

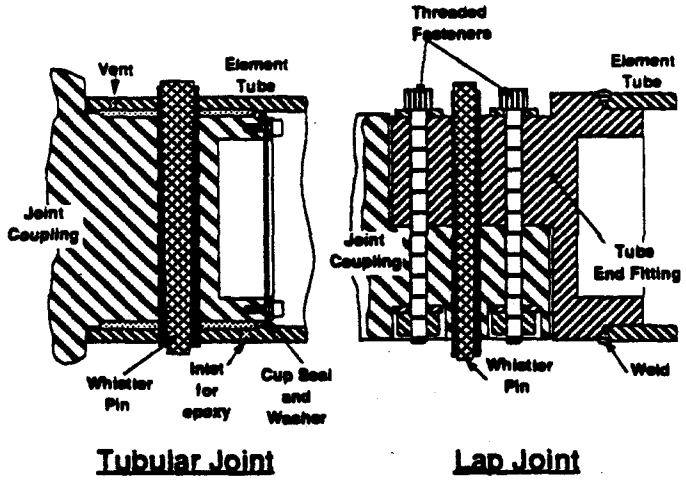

Figure IV.14: Cross sections of truss joints.

Kinematic Mounts: The attachment points to the magnet structure must permit deformations of the magnet without inducing additional stress into the module.

Flexural Feet and Cross Suspension: The design of the flexural feet that hold the chambers to the structure, and the design of the suspension to take the gravity load of the chambers crosswise to the feet was adopted from the L3 design. These are shown in Figure IV.15.

Central Region Support Structure

As described previously, the central muon detector is configured in modular form, with two sections of 16 modules each. The main structural elements are 3 inch aluminum tubes with 1/4 inch walls. Each module is supported from the magnet with 6 kinematic mounts.

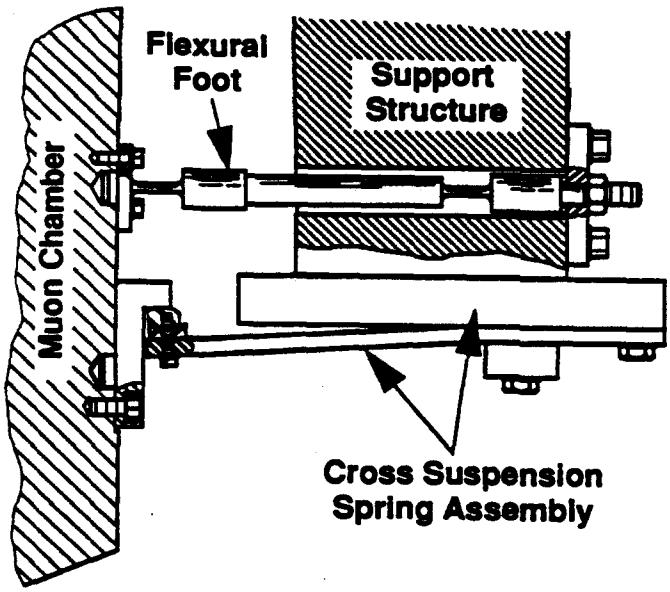

Figure IV.15: Flexural Feet and Cross Suspension.

Endcap Support Structure

Each endcap consists of 17 modules of three types. These modules are full truss structures constructed of 4 inch aluminum tubes with 1/2 inch walls for the primary structural elements. They are attached to the magnet pole pieces with kinematic mounts. The center module supports the inner ring of chambers and surrounds the beam pipe. It has the shape of a truncated cone, attaching at its large end to the magnet pole piece with 8 mounts. It supports 24 chambers. The outer ring of chambers is supported by 2 types of modules. At the periphery of the cone module, 8 modules of rectangular cross section are attached to the inner ring with kinematic mounts. Each module supports three chambers as shown in Figure IV.6. The module is also attached to the magnet pole piece at 2 mounting points. Alternating between the rectangular modules are 8 modules of triangular cross section with three chambers each. These are attached to the inner cone module and to the rectangular modules with kinematic mounts.

Forward Region Support Structure

The forward region muon detector support structure is only slightly different from the design presented in the EoI. These changes incorporate features to lower costs, and improve fabrication and maintenance procedures. The configuration is shown in Figure IV.7.

C.4 Alignment and Calibration

The alignment processes and systems are as outlined in the EoI (pp. 35-37). Changes in the geometry proposed in the endcap region diminish problems of lines of sight and reduce the number of required systems.

The global alignment, referring to the alignment of all measuring modules with respect to a common reference point close to the interaction point, is unchanged from the EoI. The global alignment of the muon detector must be continuously monitored since mechanical support is provided by the magnet which is not stable within our required precision. The geometrical instabilities of the entire experimental area with respect to the beam due to geology require adequate monitoring ranges.

The local alignment, referring to the alignment of the wire planes in the three chamber layers within a measuring module will be done with the opto-mechanical systems proven in L3 and described in the EoI. In Figures IV.1, IV.6 and IV.7 the symbols Ⓐ denote alignment paths. As in L3, the local alignment of the wire planes in the three chamber layers of a measuring module will be verified before the module is installed in the experiment. The alignment is achieved by a combination of mechanical tolerances and opto-mechanical measurements as described in the EoI. It will be verified by measurements of straight cosmic ray tracks and

of straight tracks produced by the ionization from UV laser beams fired through all three chambers of a module. The change from XY-chambers to independent radial modules in the endcap region enables us to easily verify endcap module alignment with cosmic rays before installation. Agreement to within 30 μm was achieved in L3 between the opto-mechanical alignment and the measurements with cosmic rays and UV lasers (EoI Figure IV.13, p29).

We are continuing our R&D efforts in the area of alignment and calibration. We allow a total of 20 μm wire positional error, as compared to a maximum error of 30 μm actually attained in L3. The limiting factor in the L3 positional error is tolerance build-up through the individual components in the system, as opposed to a fundamental performance limitation of any single component. For example, the L3 straightness monitor resolution is of the order 1 μm. The basic system concept can attain the required accuracy for L*. This is a modest extrapolation of existing technology. An active R&D program is underway to produce and verify the required designs.

Table IV.2: Design milestones.

Task	Completion Date
Chambers	
Fix mesh plane configuration	3/91
Define cell geometry	3/91
Define sense & mesh plane supports	6/91
Define mechanical & gas enclosure	6/91
Construct and test models	9/91
Gas	
Complete test set-up	9/90
Evaluate 10 candidate gases	9/91
Structures	
Refine truss geometries	3/91
Define global supporting element interface	3/91
Define interface system with chambers	6/91
Integrate alignment systems, services and access hardware	6/91
Construct and test models	9/91
Alignment Systems	
Translate global alignment requirements into global alignment tolerances	12/90
Define alignment processes and hardware	3/91
Integrate hardware into chambers, structures	6/91
Define module assembly	6/91
Test alignment systems	9/91
Construct and test models	9/91
Conceptual Design Review	10/91

D Milestones Toward a Detailed Design

Table IV.2 shows the main events leading to the detailed design. This schedule is consistent with the overall L* planning with the detector ready for physics in late 1999.

References

[1] Expression of Interest to the SSC Laboratory. (EoI) The L* Collaboration, May 1990.

[2] U. Becker, et al. NIM **180**(1981)61. P.Duinker, et al. NIM **201**(1982)351.

[3] L* Detector Resource Requirement Report. (RRR) Submitted to the SSC Lab, June 20,1990.

[4] The Construction of L3, the L3 Collaboration, NIM **A289**(1990)35.

[5] A Research and Development Program to Continue the Development of Precision Instrumentation for the Study of Muons in the TeVRegion. (Original Proposal) The Precision Muon Chamber Collaboration SSC PC-001, n.d. (rec'd Nov. 1989) 296pp. SSC Library Only.

[6] Progress on the Research and Development Program to Continue the Development of Precision Instrumentation for the Study of Muons in the TeVRegion with Second Year Request. Submitted to the SSC Laboratory by the Precision Muon Chamber Collaboration, September 1990.

[7] Letter from R. F. Schwitters to S. C. C. Ting, August 1, 1990.

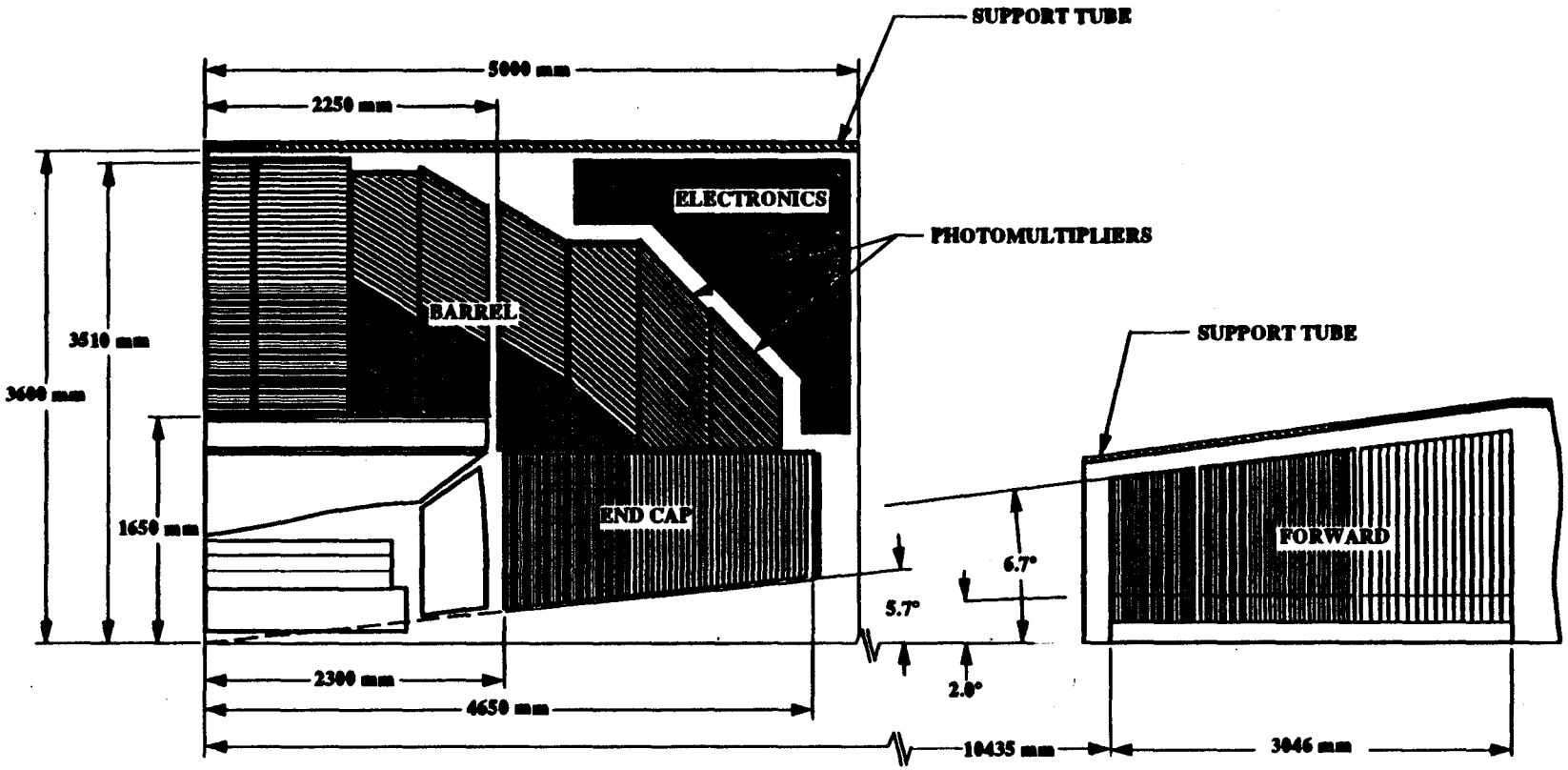

Figure V.1 L* Hadron Calorimeter: Barrel, Endcap and Forward Systems Side View

V Hadron Calorimeter

A Introduction

In accordance with the Program Advisory Committee suggestions to reduce the scope of the detector, the options proposed for the L* hadron calorimeter (Figure V.1) differ significantly from those presented in the EoI [1]. The primary differences are listed below:

1. The main option for the L* central calorimeter will utilize either liquid or solid scintillator sampling.
2. The main option for the entire forward calorimeter now consists of a tetramethylsilane (TMS) sampling medium.
3. The transverse and longitudinal segmentation of the central calorimeter has been changed, resulting in a decrease in the number of electronic readout channels from 180,000 to 50,000. For the forward calorimeter, the corresponding number of channels has been reduced from 155,000 to 33,000. Considerations leading to this design are outlined below.
4. The silicon detector option will be pursued by means of an action plan designed to reduce the production costs of silicon diodes by an order of magnitude. This plan will be implemented in close collaboration with L* collaborators from the USSR.
5. A liquid argon calorimeter option is under consideration as a backup option in case the R&D efforts do not yield positive results on an acceptable timeframe.

As was described in the L* EoI the energy measurement of hadronic jets is performed by a combined calorimetric system: a precision homogeneous electromagnetic device followed by a compensated sampling calorimeter with lead (or lead/iron) absorber and with either scintillator or silicon detectors.

High quality hadronic calorimetry is important particularly for compositeness studies and for two jet mass resolution necessary for Higgs and top mass measurements [2]. High quality implies that the energy independent term of the resolution is of the order of a few percent which is possible only if the system is effectively compensated. Our study [2] shows that for high energy jets the proposed L* system has the above characteristics.

We consider scintillator detectors, either liquid or plastic ("soft" or "hard" tiles), as our prime option since the technique itself has been used for many years for calorimetric measurements in large systems [3]. The design of the calorimeter lends itself to either option with minimal modifications since the geometry of the individual detectors and readout systems are quite similar. Technical questions related to the L* application of the scintillation method are the subject of an extended R&D program [4].

For the forward region we have chosen a warm liquid ionization sampling medium primarily for radiation hardness considerations. An extensive R&D program [5] will address specific issues of radiation damage, detector response (speed), and compensation.

B Central Calorimeter

The underlying physics of scintillator calorimetry is well understood [6] and experimentally established [3]. Its time response is adequate for the SSC rate environment.

B.1 Design Considerations

From our cost analysis and our L3 experience we note that, for a given technology, the calorimeter cost is driven by:

- number of electronics channels;
- cost of absorber and mechanical structure;
- manpower needed for design and assembly.

Rearrangement of the absorber structure by altering the sampling sequence changes the cost only if we reduce the overall thickness. However, in this case considerable performance deterioration takes place before noticable cost reduction occures. The manpower needed for design and assembly does not depend appreciably on the technology or sampling frequency chosen.

The reduction in the number of channels may affect the following:

- Jet pattern recognition deteriorates. This affects jet energy resolution, since jets are defined less precisely.
- Reduction in transverse granularity makes the lepton isolation less accurate (see EoI pp 86-87).
- A very fast muon trigger from the calorimeter may no longer be possible, see EoI (p 49)

After considering in detail the above effects, we have chosen a total number of readout electronics channels of 50,000. This corresponds to transverse segmentation of $\Delta\eta = \Delta\phi = 0.05$ with five longitudinal segments. The deterioration in performance depends on the specific pattern recognition algorithm used, and for the above configuration it was found to be acceptable.

B.2 Absorber structure and expected performance.

The total thickness of the hadron calorimeter of 11.7 λ_{int} at 90° and 14 λ_{int} in the forward direction provides 98% containment of 1 TeV hadron showers [7] and reduces hadron punchthrough rates in the muon system to a level below the rate of prompt muons coming from heavy quark decays (see EoI p 87). The thickness of the BaF_2, which serves as the front part of the calorimeter system, is 1.7 λ_{int}. The thickness of the sampling

hadron calorimeter section is 10 λ_{int}. As shown in Figure V.2, this section is subdivided into a fine sampling part (38 layers of 20 mm lead and 5 mm scintillator) and a coarse sampling part (20 layers of 40 mm lead and 5 mm scintillator).

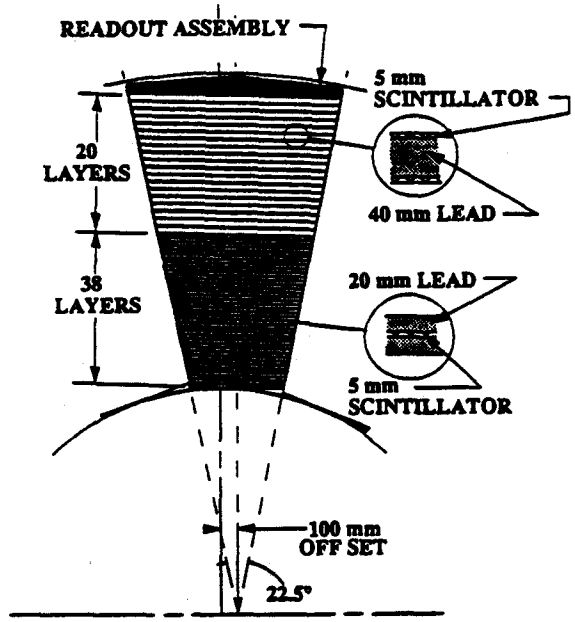

Figure V.2: Transverse sectional view of a barrel module assembly

The energy resolution of calorimeters of different configurations with the 1.7 λ_{int} of BaF_2 in front has been studied by Monte Carlo simulation with the GEANT-GHEISHA code [8]. The code was optimized with experimental L3 data on hadronic jets from Z^0 events. Figure V.3 illustrates how the Monte Carlo describes measured jet energy resolution.

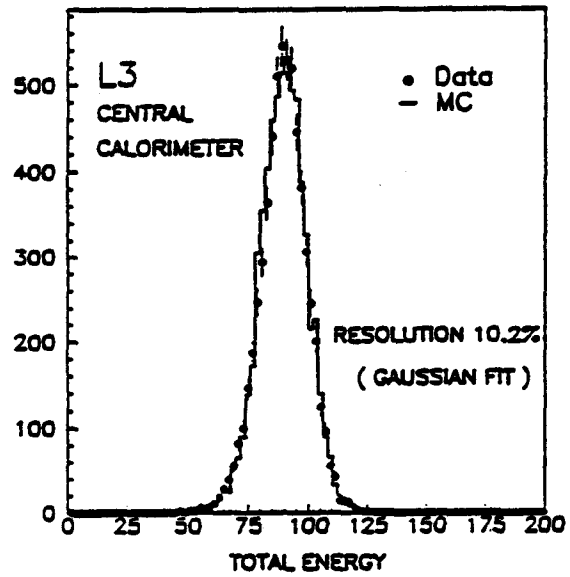

Figure V.3: Energy resolution for two-jet events measured by L3 hadron calorimeter compared with GEANT Monte Carlo simulation.

Results of these studies [2] show that the jet energy resolution depends only weakly on the sampling thickness and is close to $50\%/\sqrt{E}$ with a constant term of approximately 2%. The constant term is small because the system is effectively compensating. Fast compensation is achieved by enhancing the neutron component response through fine adjustment of both absorber sampling thickness and hydrogen density in the detector material. The jet energy resolutions for 1.7 λ_{int} of BaF_2 followed by two Pb/scintillator fine and coarse hadronic sections is shown in Figure V.4.

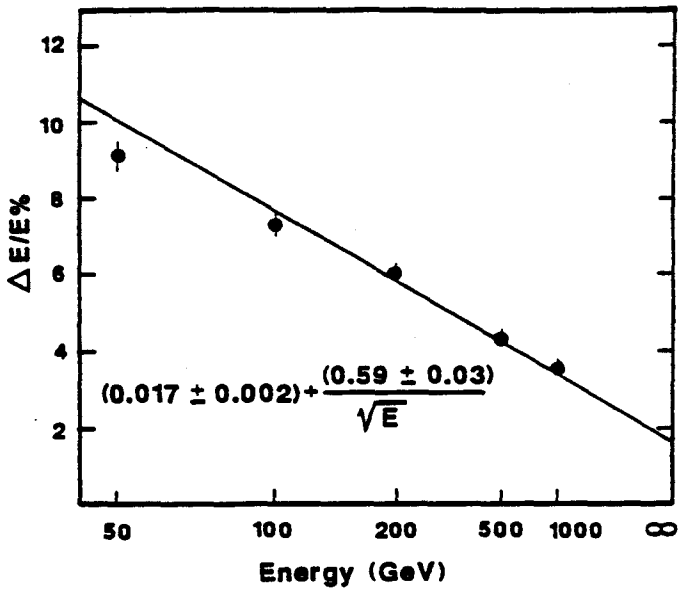

Figure V.4: The expected jet energy resolution of the proposed L* hadron calorimeter for with BaF_2 in front.

B.3 Scintillating media and light transport

For the **liquid scintillator option** light collection will be done with wavelength-shifting fibers (WLSF) immersed in the scintillating cell with diffuse reflective walls. The transport fibers have the same composition of the core and cladding except that the core is clear. Liquid scintillator can be exchanged if radiation damage occurred, though some liquid scintillators can withstand integral doses up to 100 Mrad [9]. Details are given in the EoI, p 52, and in References [2, 4].

Radiation hardness tests of scintillating fibers show that the 10 Mrad level has already been achieved and that further progress is expected [10]. One should note that radiation damage effects are less pronounced for clear fibers, as in our case, than for scintillating fibers.

Since expected radiation levels in the hadron calorimeter, shielded by BaF_2, are well below 10 Mrad (with the possible exception of some regions in the endcaps close to beam pipe which need refined design optimization) we conclude that the radiation hardness of the basic components of the proposed system should not be of serious concern.

A potential disadvantage of a liquid scintillator / optical fiber readout is a possible long-term chemical incompatibility. We have started an R&D program to find the optimum combination and we have obtained positive results for the scintillator BC-531 (Bicron) which exhibits reduced chemical activity to plastics [11]. Independent results obtained recently by Bicron [12] show that in a six month test of BC-517L scintillator, no indication of chemical incompatibility with a plastic fiber was observed. Our R&D program address compatability issues in a high-radiation environment.

In view of recent progress in the **scintillating tiles technique** [13] we also include this type of scintillation detector in our current R&D program. Many of the technical questions are similar to those for the liquid scintillator [4]. If the indicated radiation hardness of the tiles is confirmed, we will make a choice between them and the liquid scintillator at a later date.

B.4 Light collection optimization and response uniformity.

Optimization of light collection was studied with a Monte Carlo light transport code [14]. Use of diffuse reflective paint (reflection coefficient > 0.9) and spiral shape WLS fiber 1 mm in diameter for a cell of L* dimensions gives light collection efficiency of 50%. The light yield for a minimum ionizing particle at the end of a 2 m transport fiber is 50 to 150 photons. Uniformity of light collection within a cell is a few percent[4]. GEANT simulation has shown that the energy measurement is unaffected by this non-uniformity. A plastic scintillator-WLSF configuration has been reported to give similar results [15]

For calibration purposes we plan to equip every cell or tile with a radioactive source. Such a calibration system provides adequate control over detector uniformity. Our experience with the natural radioactivity of uranium used for calibration in the L3 hadron calorimeter [16] suggests that the calibration of the whole calorimeter system can be accomplished within 30 minutes, to accuracies of 1–2%. This approach has proved to maintain the uniformity and the stability of the L3 calorimeter system at a level better than one percent over a period of one year. In addition we are studying the possibility of using induced radioactivity for calibration purposes.

B.5 Segmentation and Readout

The total number of scintillation cells in the hadron calorimeter system (excluding the forward system) will be about 8×10^5 with an average cell size of $90 \times 90 \times 5$ mm^3. With a total number of readout electronics channels of 50,000, there are on average 16 fibers per readout channel.

One of the latest photodetector developments is a multichannel Hamamatsu phototube [17] with a 12 stage fine-mesh dynode system. It can operate in a magnetic field and has a gain of 10^4 in a field of 0.8 T. The photocathode has an effective diameter of 32 mm, with a quantum efficiency of 10% at 550 nm. A phototube can house 32 channels. A minimum ionizing particle produces about 50 photoelectrons in one readout channel, resulting in an excellent signal to noise ratio for muon detection. This photodetector will operate at a reduced gain of 1000–3000 will be followed by fast current amplifier with a gain of 10–100 . More details of photodetectors and electronics are given in the EoI, p 52.

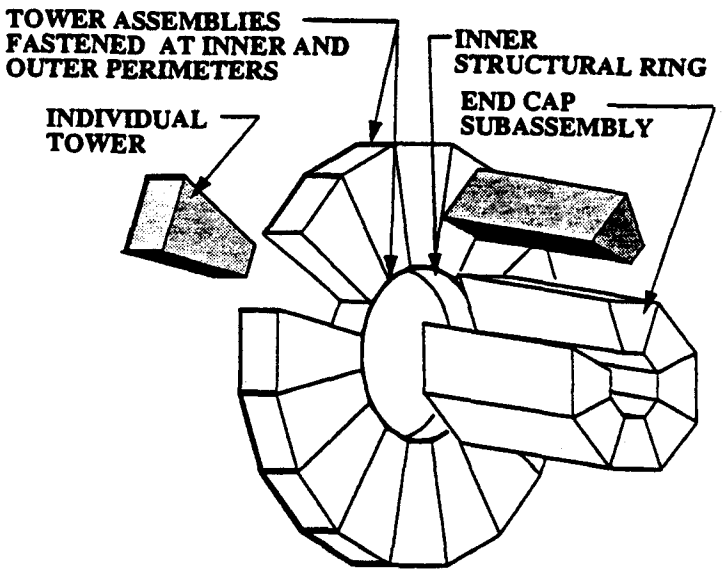

Figure V.5: Ring assembly of the calorimeter. The barrel consists of 15 rings with 16 individual modules each. The endcap configuration is also shown.

B.6 Mechanical structure

The general layout of the L* hadron calorimeter is shown in Figure V.1. The calorimeter is made of 15 structural rings and of two endcaps. Each ring consists of 16 modules and each end cap of 8 modules, as shown in Figure V.5. The total number of modules is 256. The total number of detector layers is 10528, with a scintillator volume of 29.1 m^3. The total weight of the device is 2075.5 t. A cross-section view of a calorimeter module and of the absorber/detector structure is shown in Figure V.2. Photodetectors are aligned along the magnetic field direction.

B.7 Progress in R&D

Cell and optical readout optimization.

Chemical compatability tests of liquid scintillator and plastic fibers have begun both at ITEP and at Livermore National Laboratory. Mechanically stressed and unstressed, as well as thermally shaped, fibers are exposed to liquid scintillator together with other compo-

nents of a cell and are checked for mechanical and optical damage.

Spectral characteristics of scintillators, fibers and photodetectors will be measured. Facilities [4] needed for these measurements have been set up at Livermore and Oak Ridge National Laboratories. Light yield optimization of the combined cell-fiber-photodetector system are performed at these facilities. In addition studies are performed at Tata Institute in Bombay.

Construction of prototype cells with liquid scintillator and scintillating tiles has began at ITEP, Oak Ridge, Livermore and the University of Mississippi. After the setup period, systematic measurements of light yield and of uniformity of light collection will be performed for the complete optical chain to select construction and optical materials.

After optimization of individual detector cells, a prototype detector plane will be constructed to optimize cell to cell uniformity, practical layout of WLS fibers, module sealing, calibration methods etc.

Prototype studies

A full-length calorimeter with a transverse size of 1 × 1 m^2 will be constructed and exposed to a high-energy particle beam to study compensation, energy resolution, calibration, fast data readout as well as other questions relevant for operation at the SSC. For these tests, we plan to use beams available at ITEP(Moscow) and IHEP(Serpukhov) accelerators. For higher energies FNAL beams will be used. At a later stage, we plan a combined test of the hadron calorimeter section with a BaF_2 or liquid Xe section in front. The results of these tests will be used for finalizing the design of the L* hadron calorimeter.

Radiation damage studies.

Systematic radiation damage studies will be performed by Oak Ridge, Livermore and Los Alamos Laboratories in the USA, as well as by ITEP in the USSR starting in early 1991. The aim of these studies is to select various components of the calorimeter system: scintillators, plastic optical fibers, glues, sealants and optical couplings, as well as to test radiation stability of the complete optical assembly which employs the combination of various construction elements and techniques. Similar studies will be independently carried out in Bombay.

The tests will continue after the selection of the technique has been made. The purpose will be to improve the radiation hardness of the scintillation technology to levels of SSC luminosity above 10^{34} $cm^{-2}s^{-1}$.

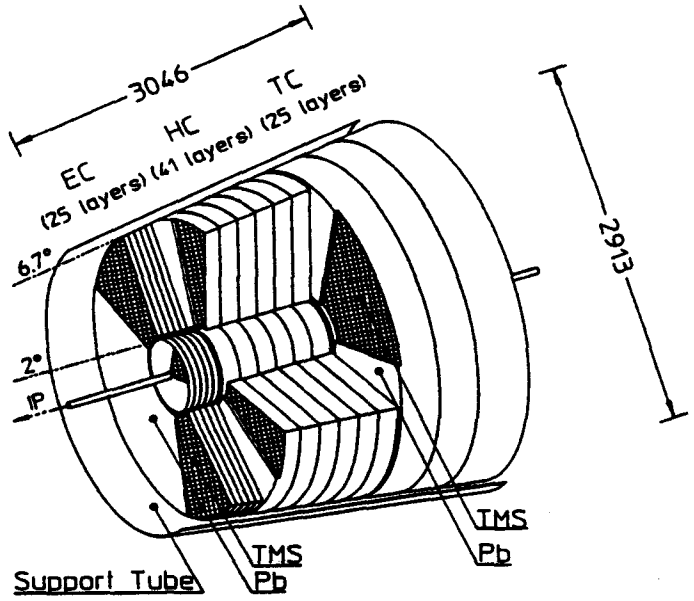

Figure V.6: Forward calorimeter system showing the electromagnetic and hadron calorimeter (TMS-Pb).

C Forward Calorimeter System

C.1 Choice of Detector Technology

The primary difference between the proposed design and the design described in the EoI is that the high-resolution BaF_2 electromagnetic section has been replaced by the tetramethylsilane (TMS) warm liquid technology for the entire forward calorimeter, thus replacing also the silicon portion of the earlier design. These changes are driven by cost and by radiation hardness considerations. In particular the elimination of the high-resolution electromagnetic section is in direct response to the need for a reduction in cost and scope. The implications are discussed in the Chapter VI. Warm liquids appear to satisfy most detector requirements for radiation hardness [18] since they can be recirculated and purified to remove decomposition by-products. Fast signals from TMS detector cells can be read out with relatively inexpensive radiation hard front-end electronics [19].

C.2 Forward Calorimeter Layout

The forward calorimeter shown in Figure V.6 covers the angular region from 6.7° ($\eta = 2.84$) down to 0.3° ($\eta = 5.95$) and extends between 10.4 and 13.4 m from the interaction point. The detector is divided into an inner and outer section, separated at 2°.

The front calorimeter consists of an electromagnetic section (25 X_0, 1.1 λ) with 25 layers of 1 X_0 lead absorber followed by a 13 λ lead hadron calorimeter section, both with TMS sampling media (dual 2.5 mm detector gap). The rear hadron calorimeter consists of a 6 λ front section composed of 41 layers of 22 mm absorber, and a 7 λ tail section composed of 25 layers of

45 mm absorber. The expected energy resolution for this device is $\sigma/E = 17\%/\sqrt{E} + 1\%$ (electromagnetic) and $54\%/\sqrt{E} + 2\%$ (hadronic). The total weight of each forward calorimeter unit is 170 t.

The forward calorimeter uses a detector pad size of (40×40) mm^2 in the electromagnetic and hadronic section, which corresponds to the same segmentation at 4°in $\Delta\eta$ (0.05) as in the central calorimetry. The corresponding number of detector elements is 2366 per layer. Each detector element (pad) will be equipped with its own amplifier mounted on or near the pad, which will guarantee an amplifier rise time between 5 ns and 10 ns for the maximum allowable pad capacitance (20 pF). Detector elements are grouped into tower segments. There are 2 and 5 longitudinal segments in the electromagnetic and hadronic sections, respectively. The total number of readout channels in both forward systems is 33,000.

C.3 R&D Issues

We propose an R & D program [5] to develop a radiation-hard prototype TMS calorimeter for the forward region, where a system engineering approach to the construction of a large calorimeter will play a dominant role. Tests of material compatability with TMS will be performed using the actual materials of the containers and electrodes for this calorimeter. Electron drift velocities and free electron lifetimes will be measured for a number of metals, plastics, ceramics, and epoxies exposed to TMS. Radiation damage tests of TMS with MeV neutrons and with other radiation will be performed to study radiolysis, changes in free ion yield, pressure buildup, and bulk contamination within the actual containers equipped with electrodes designed for this calorimeter. The next step will be to incorporate the necessary engineering and chemical safeguards in order to guarantee long term stability and accuracy of the measurement. Beam tests will allow the absorber structure to be finalized in order to obtain full compensation.

The following institutions will investigate the R&D issues described above:

- The University of Alabama System
- I Physikalisches Institut RWTH, Aachen
- The Tata Institute for Fundamental Research
- Oak Ridge National Laboratory

D Silicon Calorimetry Option

D.1 Introduction

The intrinsic advantages of silicon are described in the L* EoI (p 46). Recent results [20] also indicate that its radiation hardness characteristics may permit its use in trackers and calorimeters up to luminosities of 10^{34} [21] and that a fast silicon calorimeter can be made to compensate using electromagnetic suppression [22].

The single impediment to the widespread selection of silicon is the question of price and procurement. At the current lowest world market prices for silicon pad detectors in small quantities, the detectors alone for a large hadron calorimeter could cost from $80 to $200 million which would clearly prohibit use of the technology for such purposes. We outline below a plan aimed at reducing the production costs by an order of magnitude [23].

D.2 Silicon Procurement

Our most promising approach to minimize cost lies in cooperation with the USSR. The steps to cost reduction in detector manufacture are:

1. The cost of raw material must be low.
2. Labor costs should be reduced. The number of processing steps must be kept low and the cost per step carefully scrutinized.
3. Quality control must be introduced to maximize yield of finished detectors. In particular, failures late in the processing chain are most harmful.

Nearly all thick silicon detectors in use in high energy physics have been constructed from high-resistivity n-type float zone material from a few suppliers in Europe and Japan, notably Wacker, TopSil and Komatsu. Most have utilized minor variations of the Kemmer planar process of oxide passivation, employing the ion implantation technique. Other techniques are well known from experience with nuclear detector construction but have not been studied seriously from the viewpoint of mass production and low price. Nevertheless, some of these techniques show considerable promise with respect to simplification and reduction of the number of processing steps. The following are being pursued:

1. Procurement of silicon and detector fabrication in the USSR and Europe.
2. Use of alternative technologies for detector fabrication, e.g. diffusion and surface barrier processes with emphasis on procedures for process simplification and cost reduction. This includes the use of moderate to high resistivity Czochralski silicon as a replacement for float zone raw material. The high oxygen content of such material may result in improvement of the radiation hardness.
3. Study of the significant advantages in the USSR, of the division of the fabrication process. Advantage should be taken of reduced labor costs in the Soviet Union.
4. Use of p-type silicon, particularly in areas of calorimetry where extraordinary radiation hardness is required.

We describe briefly the specific steps to be taken in concert with Soviet scientists to establish the capability

of the Soviet silicon program and the assignment of responsibilities to specific organizations. A research team of over 50 physicists from 10 institutions has been organized. The goal is to check the entire chain of detector manufacture including the potential for mass production. Soviet specialties are described below and institutions involved are listed.

1. Silicon ingot production.
   - Zaporozhye Titanium Magnesium Factory, Zaporozhye, USSR.
   - State Institute of Rare Metals, Moscow.

   These institutions have the capability to produce 5–10 t of high resistivity silicon per year. (About 24 t of silicon are required for the L* calorimeter). Ingots from these producers will be introduced into the test program of detector fabrication both in the US and the USSR. The material will be bulk tested in the US prior to distribution to detector fabricators.
2. Wafer preparation (sawing, double-sided polishing, etc) and detector fabrication (passivation, gettering, surface barrier, diffusion, ion implantation, photolithograhy, etc.)
   - Joint Institute of Nuclear Research, Dubna
   - Institute of Electronics Machinery and Materials Research Institute, Zelenograd, Moscow

   These detector fabrication centers will be thoroughly evaluated with respect to capability and reliability.

D.3 Radiation Damage Studies

The following institutions will work on techniques to improve the radiation hardness of silicon detectors and the integration of the results into the detector manufacture process in the Soviet Union.

- Kurchatov Institute, Moscow.
- Leningrad State University, Leningrad.
- Byelorussian State University, its institutes for Nuclear Problems and for Applied Physics, Minsk.

D.4 US and other R&D

A program has begun in the US involving Oak Ridge, the University of Tennessee, IntraSpec Corporation, and a number of private detector manufacturers. In addition, several Italian groups centered around the SICAPO collaboration are also involved in R&D. The issues covered will be similar to those covered above. Close interaction between these groups and efforts in the Soviet Union will be maintained.

D.5 Progress on Prototype Construction and Beam Test Studies

Single-plane beam tests of silicon detectors are currently underway at ITEP. A fully-engineered full-scale prototype, consisting of a $\frac{2\pi}{16}$ azimuthal wedge of an $\eta = 0$ L* central hadron calorimeter section as described in the EoI (p 47) is under design and is planned for completion in mid-1993 with subsystem funding. The silicon detectors for this prototype will be provided by the USSR as a test of the procurement and production plan described in the previous section. Extensive beam tests in conjunction with the BaF_2 and LXe electromagnetic calorimeter prototypes will be done in late 1993.

E Liquid Argon Option

E.1 Introduction

The performance record of Liquid Argon Calorimeters (Mark II, TASSO, CELLO, NA31,SLD), [24] suggests that a safe extrapolation to the requirements of L* at the SSC can be done. Furthermore, the recent experience with the setup and calibration of the H1 [25] detector at HERA can serve as a guideline to estimate the engineering and calibration efforts required in the L* framework. In addition, one of the L* collaborating institutions, RWTH Aachen, has a longstanding experience in building and operating large liquid argon detectors at colliders [26].

The obvious disadvantage of this technology is the long signal duration from liquid argon ionization which results in a baseline shift and in additional noise, as well as in a higher occupancy of the detector cells [27]. There are, however, advantages to be exploited, such as radiation hardness, granularity, and inherent system stability. Using Pb as absorber, an energy resolution for pions of $45\%/\sqrt{E} + 3\%$ has been achieved [25] applying spatial weighting.

E.2 Description of the liquid argon calorimeter

Figure V.7 shows a cut through the containers and absorbers in a plane containing the beam. The assembly consists of three independent containers housing the central and the two endcap sections of the absorbers and ionization detectors, respectively. These three separate containers allow for installation and maintenance access to the inner detector from both ends of the L* detector. The system support services (pumps, cryogenerators, power, supplies for electronics etc.) are located outside of the magnetic field at the upper periphery of the L* detector. Services are run in the interstitial space between the endcap and the central muon chamber supports. The containers house absorber towers arranged in a way that is almost identical to the configuration described for our preferred technologies. Details of the

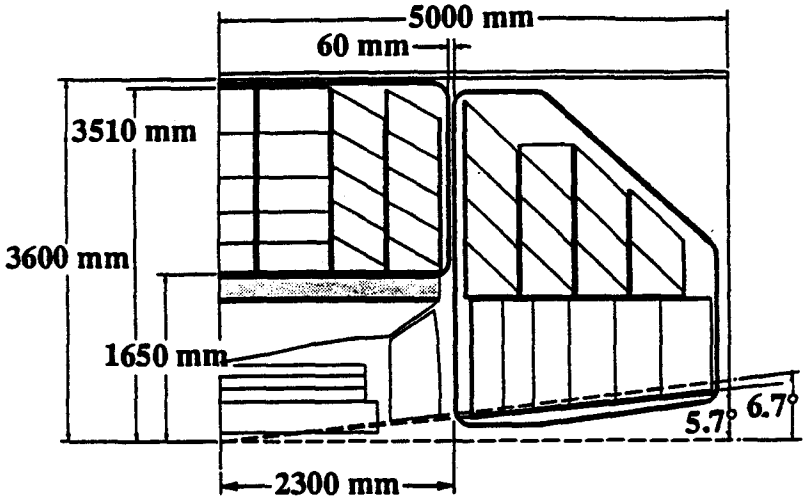

Figure V.7: L* hadron calorimeter with liquid argon ionization chambers

absorber structure, the expected performance as well as the structure parameters are given below:

Table V.1: LAr Calorimeter Absorber Structure

Absorber material	Pb
Number of layers and structure	$38 \times 4X_0 + 19 \times 8X_0$
Detector gap width	4 mm
Total thickness at 90°	9.8 λ_{abs}
Expected jet energy resolution (BaF_2 in front)	$4.5\% + 45\%/\sqrt{E}$

Signal pickup and drift-field generation will be integrated on single sheet-electrodes, as pioneered by the H1 collaboration [25]

The requirements of the central liquid argon calorimeter for electronics are very similar to those of the TMS calorimeter foreseen for the forward systems. The layout of the amplifiers for the forward system can be easily adapted to the liquid argon cryogenic environment. We foresee that the digitization will be performed directly on the detector. The trigger will require deeper pipelines and possibly more sophisticated background subtraction techniques than those foreseen for the faster calorimetry techniques.

F Schedule and Milestones

Table V.2 summarizes milestones and gives a schedule of decisions which will lead to the final selection of the central hadron calorimeter technology. The schedule for the overall assembly is given in Chapter IX.

G R & D Organization

The L* Hadron Calorimeter Project is an international collaboration of several Institutions from USA, USSR, Germany, Italy and India. The base of the collaboration is the L3 Hadron Calorimeter group which has constructed the L3 Uranium calorimeter now in operation at the LEP collider.

Since L* calorimetry has several options, the work to finalize the design will follow several lines before a final choice is made.

- ITEP, Oak Ridge, Livermore and the University of Mississippi will be responsible for both **the liquid scintillator and the scintillating tile options**. Details are given in Ref. [4] .
- JINR (Dubna), University of Tennessee, Oak Ridge, Universities of Florence and Milan in Italy, RWTH, Aachen will be responsible for **the silicon pads option**. The main question they will address is that of silicon procurement [23].
- The University of Alabama and RWTH Aachen will design **the forward systems**, including electronics [5].
- **Computational support** will be provided by Oak Ridge, University of Mississippi, and Tata Institute in Bombay, India, as well as by the University of Alabama, RWTH Aachen and Los Alamos.
- **Engineering design** work will be concentrated in Oak Ridge and Aachen.
- **Electronics** will be designed in Oak Ridge and Livermore.

References

[1] Expression of Interest to the SSC Laboratory. (EoI) The L* Collaboration, May 1990.

[2] Report to the PAC by the L* collaboration Submitted July 7,1990.

[3] F.S.Merritt et al., NIM A245 (1986) 27; T.Akesson et al.,NIM A262(1987)243; E.Bernardi et al.,NIM A262(1987)229.

[4] "Liquid Scintillator Calorimetry", A Research and Development Proposal, Submitted to the SSC Lab, June 20,1990; and "Development of a Compensating Scintillator Plate Calorimeter System for the SSC", SSC Subsystem Proposal R&D Proposal, June 1990.

[5] A R&D Proposal to Develop Fast Forward Calorimetry for the SSC, submitted to the SSC Laboratory (August 1990)

[6] R.Wigmans NIM A259 (1987) 389.

[7] D.Bintinger, Proceedings of the Workshop on Calorimetry for the SSC", Tuscaloosa, Alabama, 1990. R.Bock et al, NIM,186(1981) 533.

[8] GEANT version 3.13(September 1989);see R.Brun et al., GEANT3, CERN Report CERN DD/EE/84-1 (Revised)(September 1987).

[9] Bicron Application Note SC-115 and references therein.

[10] A.Maio, ECFA LHC Workshop, Aachen, 4-9 October 1990. H.Leutz et al, *ibid*, U.Holm et al, *ibid*.

Table V.2: Schedules and Milestones for the Central Calorimeter

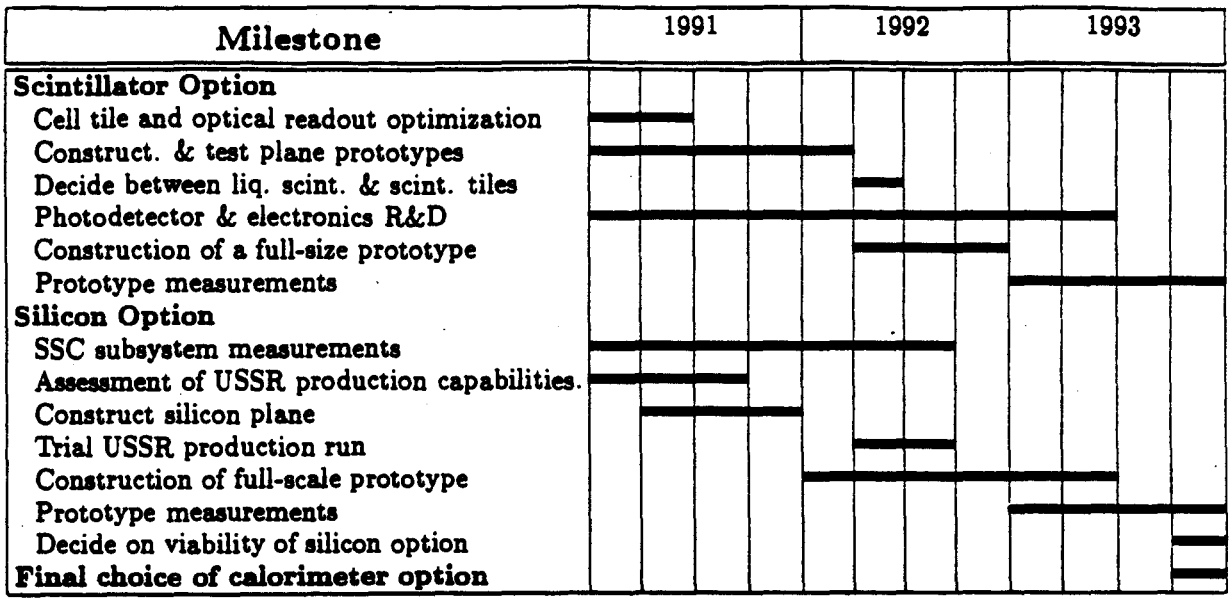

[11] Bicron BC-531 Data sheet.

[12] Ch. Hurlbut,BICRON Corporation, priv. comm.

[13] J.Harmon and J.Walker, Symposium of Detector R & D for the SSC, Ft. Worth,Texas, Oct.15-18,1990.

[14] Yu. Kamyshkov et al /in preparation/

[15] G.W.Foster, Symposium of Detector R & D for the SSC, Ft. Worth,Texas, Oct.15-18,1990.

[16] L3 Collaboration, NIM A289 (1990)35. O.Adriani et al, CERN-PPE/90-158, 1990.

[17] S.Suzuki, Hamamatsu Photonic K.K., priv. comm.

[18] D.M. Lee, W.W. Kinnison and W.B. Wilson, LANL internal report, Oct. 1990.

[19] D.DiBitonto et.al., NIM, A279(1989)100.

[20] R. Wunstorf et al., Proceedings of 2'nd International Conference on Advanced Technology and Particle Physics, Como, Italy,11-15 Jan.,1990.

[21] M.G. Gilchriese, Symposium of Detector R & D for the SSC, Ft. Worth,Texas, Oct.15-18,1990.

[22] F. Lemeilleur et al., Phys.Lett.B222(1989)4.

[23] SSC Detector Proposal for Development of an Endcap Electromagnetic Calorimeter Employing Silicon Detector Sampling. Oct. 1,1990.

[24] G.S.Abrams et al. IEEE Trans.Nucl.Sci.25(1978)309, & 27(1980)59, A.Ladage et al., SLAC report 250(1982)180, M.Altoff et al., Z.Phys. C26(1984)337, H.J.Behrend et al., Phys.Scripta 23(1981)610, H.Burkhardt et al.,NIM A268(1988)116, A.C.Benvenuti et al.,NIM A289(1990)463.

[25] W.Flauger et al.,NIM A289(1990)446, W.Braunschweig et al.,NIM A265(1988)419

[26] V.Kadansky et al., Physica Scripta 23(1981)680, U.Micke et al.,NIM 221(1984)495, W.Braunschweig et al., NIM A275(1989)246.

[27] C.W.Fabjan, CERN 89-10, p.535, C.W.Fabjan and R.Wigmans Rep.Progr.Phys. 52(1989)1519.

VI Electromagnetic Calorimeter

A Introduction

The method of precisely measuring inclusive photons and electrons in L* is based on many years of experience in the measurement of electrons in high background environments. To make a clean measurement of electrons and photons, it is important to eliminate the following two dominant backgrounds:

1. $\pi^0 \rightarrow \gamma\gamma(\gamma \rightarrow e^+e^-)$ background from photon conversion. This implies:
   (a) a minimum amount of material in front of the electron (photon) detector;
   (b) a precision tracking detector in a magnetic field to separate out $\gamma \rightarrow e^+e^-$ conversion pairs; and
   (c) a fine grained detector which can measure the e^+ and e^- separately and thus reject $\gamma \rightarrow e^+e^-$ pairs.
2. (π, e) confusion background. This occurs when a hadron enters the electron detector and gives a signal similar to an electron. This background can be most effectively rejected by measuring the electron momentum twice: once in a precision spectrometer measuring the momentum P_1 of the electron as it emerges from the interaction region, and again in a crystal detector measuring the momentum P_2. The constraint $P_1 = P_2$ effectively eliminates the (π, e) confusion background.
   It was a careful application of this technique that enabled the BNL-MIT group to construct the BNL-J particle spectrometer which had an $\frac{ff}{hh}$ rejection of 10^{10} and a mass resolution of $\frac{\Delta m}{m} \approx \frac{1}{1000}$.

Many advances have been made on the L* EM calorimeter options: Barium Fluoride (BaF_2), Figure VI.1, and Liquid Xenon (LXe), Figure VI.2. Indeed both options are very promising. The final choice can only be made after further detailed R&D work.

B Barium Fluoride

B.1 Introduction

Following the recommendations of the Program Advisory Committee (PAC):

- We have reduced the cost of the electromagnetic calorimeter by replacing the forward-backward BaF_2 calorimeter with a Pb-TMS sampling calorimeter which covers $|\eta| > 2.8$. See Chapter V.
- Production of large size BaF_2 crystals has been successfully demonstrated by the Shanghai Institute of Ceramics (SIC) and Beijing Glass Research Institute (BGRI). The first batch of crystals shows a UV light transmittance which meets our specifications.
- A firm commitment has been obtained from the managements of SIC and BGRI to ensure that the quantity of BaF_2 crystals required by L* will be provided at a fixed price of \$2.5/cm^3.
- The light collection uniformity of BaF_2 crystals from the first batch of BaF_2 crystals is ~2%.
- Tests of a new phototriode equipped with a K-Cs-Te photocathode suppressing the slow component in BaF_2 are under way.
- Systematic studies on BaF_2 radiation damage indicate that (a) radiation damage in BaF_2 is saturated after ~100 kRad, and (b) it is caused by externally introduced impurities. By controlling the level of impurities, therefore, radiation hard crystals can be produced.
- The first calibration Radio Frequency Quadrupole (RFQ) has been produced for the L3 BGO. This will provide real experience on precision *in situ* calibration starting in 1991.

In spite of the reduced angular coverage of the precision BaF_2 calorimeter, the overall detector performance is adequate to detect the intermediate mass Higgs in a mass range of 80 to 160 GeV by measuring the $H^0 \rightarrow \gamma\gamma$ decay channel (see Chapter X). This is the only channel which can be used to close the gap between the upper limit for Higgs detection at LEP (80 GeV) [1] and the lower limit at the SSC through four lepton final states (140 GeV) [2]. The details of this search are presented in the Report to the PAC [3].

B.2 Detector Design

Figures VI.1 and VI.3 show the conceptual design of the proposed barium fluoride calorimeter, which consists of two parts:

- A central barrel calorimeter with an inner radius of 75 cm and an outer radius of 140 cm, covering a rapidity range of $|\eta| \leq 1.45$ ($26° \leq \theta \leq 154°$).
- Two endcaps, located at z=± 150 cm, covering a rapidity range of $1.45 \leq |\eta| \leq 2.87$ ($6.7° \leq \theta \leq 26°$ and $154° \leq \theta \leq 173.3°$).

The total crystal volume of the BaF_2 calorimeter is 12.6 m^3, with a total crystal weight of 61.5 t. Table VI.1 shows the basic parameters of the BaF_2 calorimeter

The calorimeter has the following features:

- **Speed:** gating time is less than 16 ns;
- **Energy Resolution:** $\Delta E/E = (1.3/\sqrt{E} + 0.5)\%$;
- **Position Resolution:** Δx and $\Delta y \approx 1$ mm at the surface of crystals
- **Segmentation:** $\Delta\eta \approx \Delta\phi \approx 0.04$;

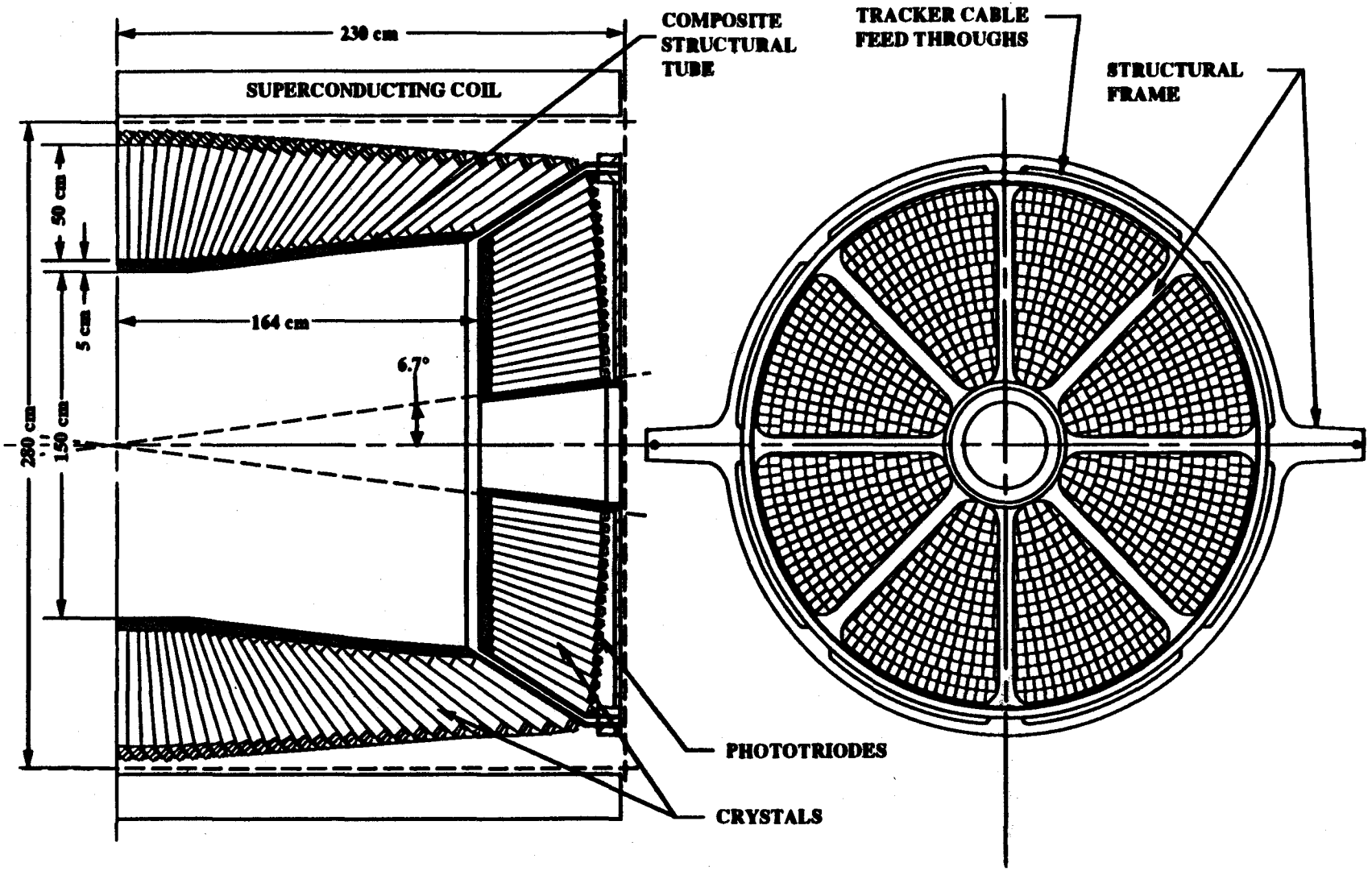

Figure VI.1 The side and end view of the L* BaF_2 calorimeter

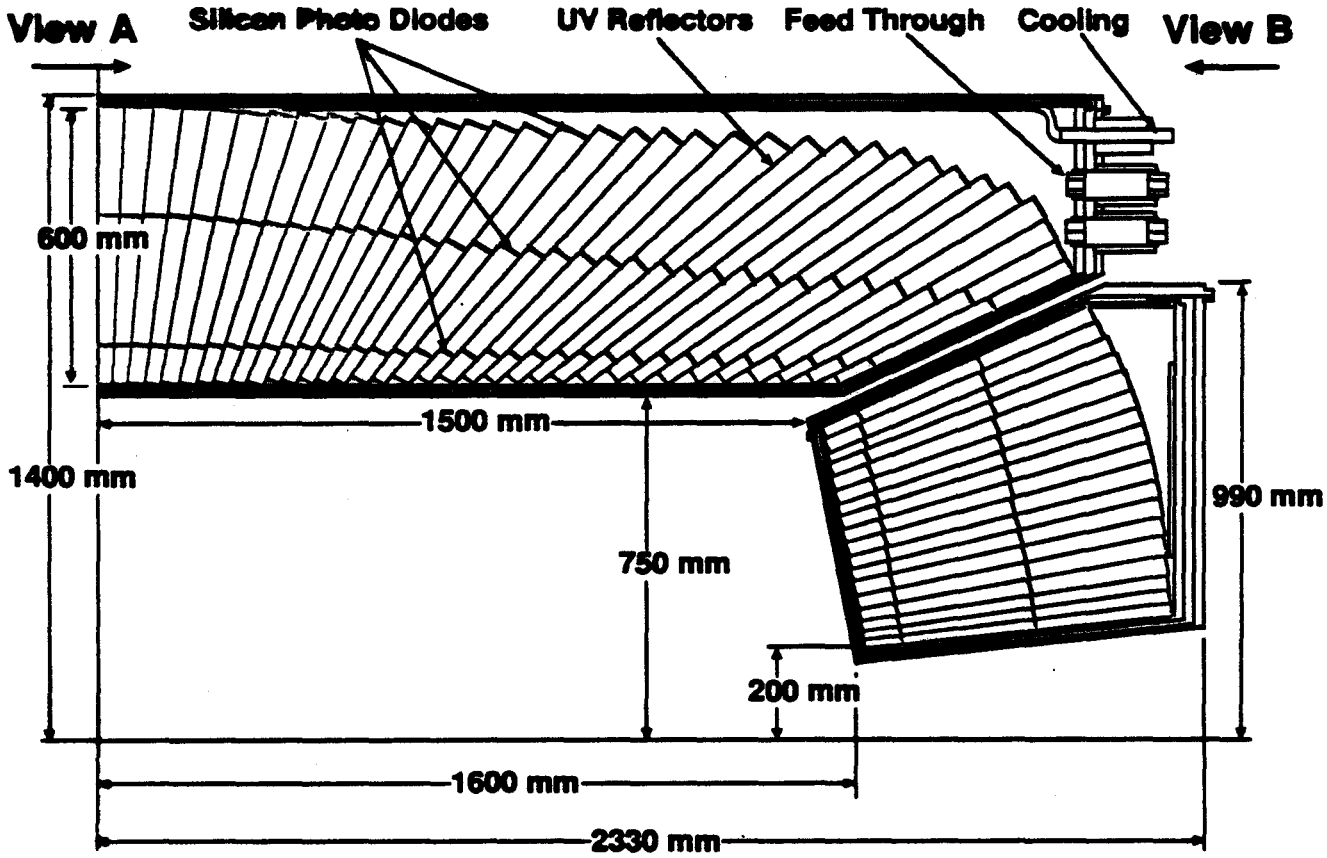

Side View of one quadrant of LXe EM detector

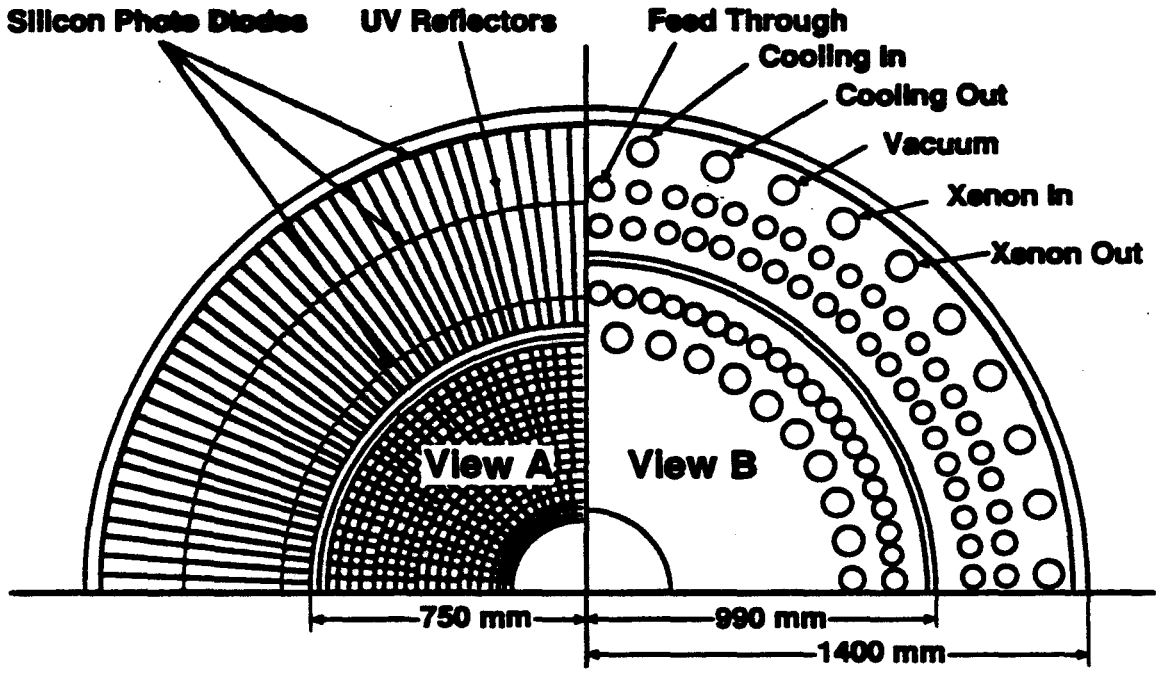

End Views

Figure VI.2 Side and end view of the L* LXe EM Calorimeter

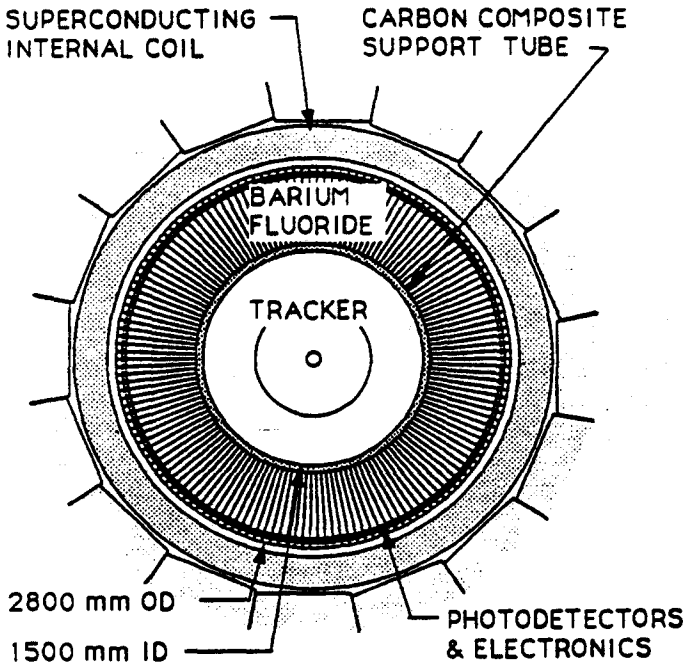

Figure VI.3: Middle section view of the BaF_2 calorimeter.

- **e/π, γ/jet, and e/jet Separation:** $\sim 10^{-4}$;
- **Radiation Resistance:** $\geq$ 10 MRad.

The details of the performance of the BaF_2 calorimeter have been presented in pp.59–61 of L* EoI [4], and in Section A.1–5 of BaF_2 subsystem R&D proposal [5]. Recent progress is summarized below.

B.3 Crystal Production

SIC and BGRI have set up a large joint technical effort [5] to develop a mass-production technique for high quality BaF_2 crystals at a cost of \$2.5/cm^3. SIC began the necessary studies in 1989, and has installed a large vacuum furnace facility. BGRI has many years of experience in BaF_2 crystal growth.

Using large vacuum ovens, they have successfully grown large-diameter BaF_2 crystals of 30 cm length. The first pair of large crystals was delivered to Caltech in August, 1990. Crystals for an array consisting of 49 crystal pairs will be delivered by March, 1991 [6]. The array will be tested at a CERN test beam in Summer, 1991. The management at both institutes has firmly committed to deliver BaF_2 crystals at \$2.5/cm^3 in the quantity needed.

We have also identified Leningrad State Optical Research Institute (LSORI) as another source of BaF_2 crystals at the same price. The LSORI has been able to grow large BaF_2 ingots in the form of disks up to 50 cm in diameter and 6 cm thick (58 kg), by the hydrothermal method, and to produce cut and polished crystals up to $4.7 \times 4.7 \times 35$ cm^3. An extensive R&D program will be carried out at LSORI together with physicists at the Leningrad Nuclear Physics Institute (LNPI) to develop BaF_2 crystals of the size and quality required.

Table VI.1: Features of the BaF_2 Calorimeter.

Barrel ($\lvert\eta\rvert \leq 1.45$)	
Crystal Front Face (cm^2)	3 × 3
Crystal Rear Face (cm^2)	5 × 5
Crystal Length (cm)	50
Total Crystal Number	10,944
Total Crystal Volume (m^3)	9.9
Total Crystal Weight (t)	48.4
Two Endcaps ($1.45 \leq \lvert\eta\rvert \leq 2.87$)	
Crystal Front Face (cm^2)	2.3 × 2.3
Crystal Rear Face (cm^2)	3.1 × 3.1
Crystal Length (cm)	50
Total Crystals Number	7,100
Total Crystal Volume (m^3)	2.7
Total Crystal Weight (t)	13.1

B.4 UV Transmittance

We have specified the transmittance requirement in terms of the minimum fraction of the light passing through a 25 cm long BaF_2 crystal at specified wavelengths:

- $\geq$ 75% at $\lambda = 200$ nm
- $\geq$ 80% at $\lambda = 220$ nm

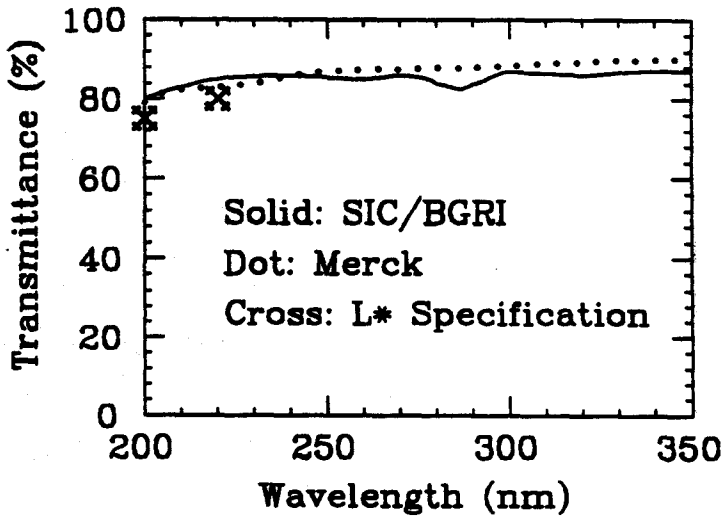

Figure VI.4: Optical transmission of 25 cm long crystals delivered by SIC and BGRI and by Merck, as a function of the wavelength. The crosses represent the transmission specifications required [5].

For simplicity, these specifications include ~8% loss at two interfaces between air and BaF_2. Figure VI.4 shows the transmittance of a 25 cm long BaF_2 crystal recently delivered by SIC and BGRI, together with the

L* specifications shown as crosses. This transmittance has met the specifications quoted above. The impurities of the raw materials used for crystal growth will be analyzed, to identify the cause and to remove the small dip around 285 nm. The transmittance of a typical Merck crystal is also shown in Figure VI.4 for a comparison.

B.5 Light Collection Uniformity

The light collection uniformity of BaF_2 crystals delivered by SIC and BGRI has been measured with a collimated ^{137}Cs source. Figure VI.5 shows the result of a measurement using a photomultiplier (PMT) with a Cs-Te solar-blind photocathode (Hamamatsu R3197). With simple aluminum wrapping, the measured response of the fast scintillation component shows a uniformity within ~2%. Given our experience with L3 BGO data, we conclude that this uniformity is better than necessary to maintain the specified resolution.

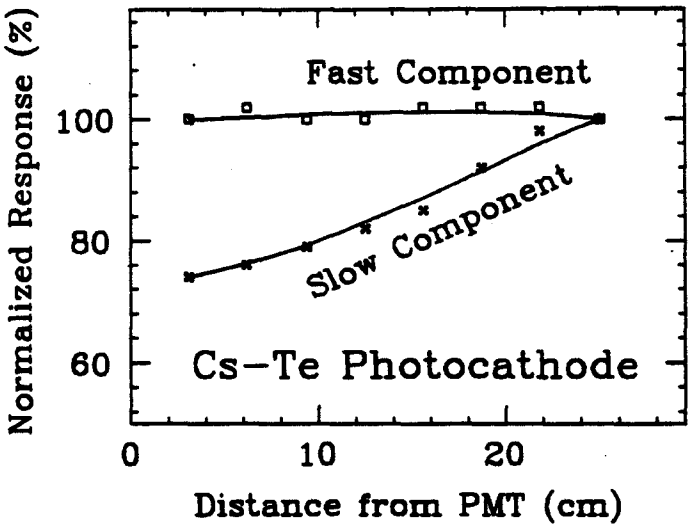

Figure VI.5: Light collection response measured with a collimated ^{137}Cs source running along the axis of a 25 cm long BaF_2 crystal, normalized to the far end.

The good light collection uniformity is a direct consequence of a compensation between two effects: the bulk light attenuation and the optical focusing caused by the tapered shape of crystals. Because of a longer light attenuation length, the response of the slow scintillation component shows an increase with an increasing distance from the PMT. This is also demonstrated in Figure VI.5.

Part of the BaF_2 subsystem R&D program will be devoted to the development of methods of controlling the light uniformity during mass production of crystals [5].

B.6 Photodetector Development and Slow Component Suppression

As detailed in p.60 of the L* EoI [4], the fast UV light from BaF_2 is read out by a vacuum photodetector with a K-Cs-Te photocathode and a quartz window. The K-Cs-Te photocathode suppresses the slow BaF_2 emission component (310 nm) by a factor of 50, resulting in an overall fast to slow component ratio of ~10. The residual slow component will then be further suppressed by a fast analog readout. The current version of the fast analog readout includes a low noise preamplifier mounted on the base of each photodetector and a shaper, with a peaking time of less than one beam crossing, developed at BNL [5]. A PSPICE simulation shows that the bipolar output of this fast analog readout will further suppress the tail due to the slow component, down to the 10^{-4} level after 35 ns.

Hamamatsu has commercialized the K-Cs-Te photocathode in a vacuum phototriode (R4406) [7]. As a conservative solution, we plan to use R4406 phototriodes together with a wedge shaped quartz window The wedge shaped window will allow the triode to be mounted at an angle of $\leq 45°$ to the direction of the L* magnetic field. With this arrangement, in a magnetic field up to 1 T, the triode will have a gain of $\geq$ 45% of the nominal value [7]. Figure VI.6 is a schematic showing the details of the triode installation at η=0.

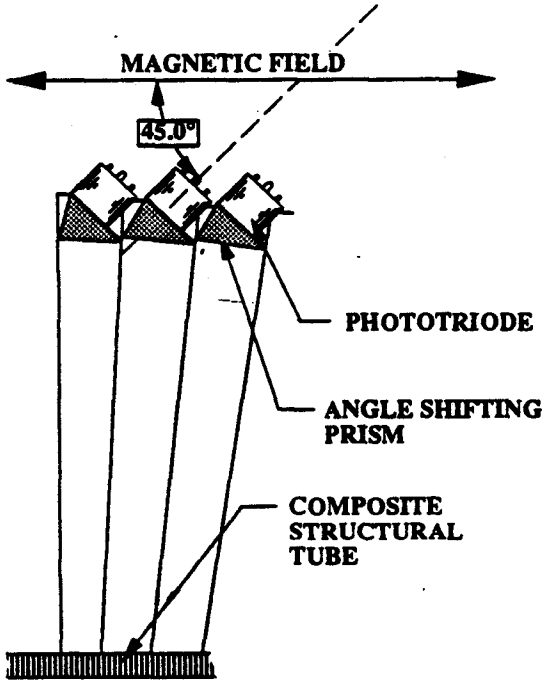

Figure VI.6: A schematic showing the installation of vacuum photodetectors on BaF_2 crystals at η=0.

Hamamatsu is actively developing a thin proximity-focused UV-selective vacuum photodiode with a K-Cs-Te photocathode. This diode will have a 1 mm gap between the cathode and the anode to allow a low anode capacitance (~10 pF). The applied voltage will be approximately 3 kV. A quartz wedge window will also

be used to make the photodiode follow the field direction [8]. This photodiode would be a natural choice for the final BaF_2 readout.

The first prototype series of the analog readout circuits is currently being built at Princeton, Oak Ridge and Los Alamos. It will be tested within the next 3 months [5], and will be used during the first BaF_2 beam test in the Summer of 1991.

B.7 BaF_2 Radiation Resistance

BaF_2 is one of the most radiation resistant crystal known. It is understood that the fast component in BaF_2 is produced by the "cross scintillation" mechanism [10]. Studies on other fluoride crystals have shown that this mechanism occurs in crystals with very high radiation resistance, and that it produces scintillation light with only a weak temperature dependence [10].

Systematic studies of the radiation damage mechanism in BaF_2 have been performed. Tests show that the radiation damage of BaF_2 caused by either γ-ray or neutron irradiation is recoverable by annealing the crystal at 500°C for 3 hours [11]. This measurement indicates that neutrons, as well as photons, do not cause permanent damage to BaF_2 crystals.

BaF_2 crystals irradiated with γ-ray doses up to 20 MRad, and at the UC Irvine reactor with doses up to 10^{14} neutrons/cm^2, show that a small initial damage occurs after the first 100 kRad and no further damage follows. This saturation effect indicates that the radiation damage in BaF_2 is not caused by an intrinsic color center in the bulk material of crystal, such as O^{--} vacancies in BGO [12], but by externally-introduced impurities.

The consequence of this initial damage has also been investigated. Figure VI.7 shows that the transmittance of a 2.5 cm long BaF_2 crystal decreased by ~1% after 2 MRad dose of ^{60}Co γ-rays [9]. This indicates a ~20% loss in transmittance for a 50 cm long crystal with existing quality. This loss will be further reduced by controlling the level of impurities in BaF_2 crystals.

Investigations of the correlations between the quantity and type of impurity in the crystal (down to the sub-ppm level for critical impurities such as Pb, Fe and other transition metals) and the initial damage are being carried out at SIC, BGRI, Carnegie Mellon University (CMU) and Caltech [5, 6].

B.8 Calibration and Monitoring

Precise, frequent calibration *in situ* is vital to maintain the high resolution of a precision detector. As shown in our GEANT study on BaF_2 resolution [4], the dominant contribution to the resolution of BaF_2 calorimeter is the uncertainty of intercalibration. Our primary calibration *in situ* will use a technique based on an RFQ accelerator [13]. The details of this technique can be found in

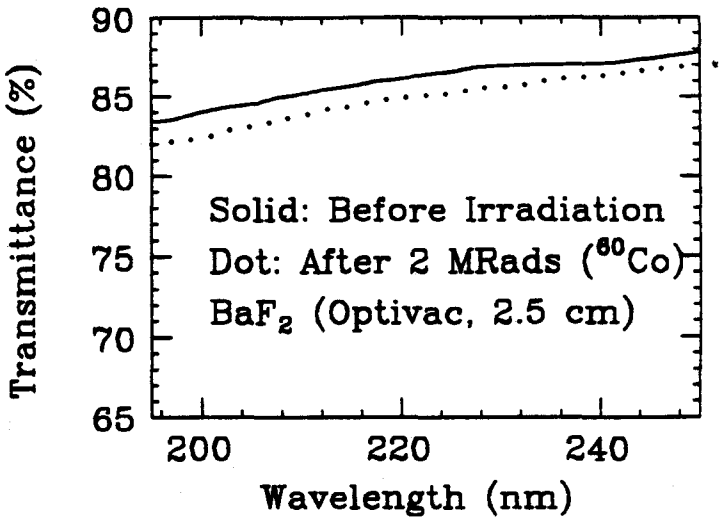

Figure VI.7: The transmittance of a 2.5 cm long BaF_2 crystal, as a function of wavelength, before and after 2 MRad dose measured by Woody *et al.*

Section A.6 of the BaF_2 subsystem R&D proposal [5]. The first calibration RFQ has been produced and tested at AccSys Inc. It will be installed in February, 1991, for the L3 BGO calibration.

Monitoring the BaF_2 crystals precisely with a UV laser and quartz fiber is being investigated. This will provide an additional means of maintaining the high precision of the BaF_2 calorimeter.

B.9 R&D Program

An extensive R&D program is being carried out to develop and to complete the engineering design for the BaF_2 calorimeter for the SSC. The R&D program will culminate in the construction of a high precision prototype composed of 144 production-quality BaF_2 crystals. The prototype will be tested and calibrated using high energy electron and pion beams together with a hadron calorimeter prototype, at either BNL, CERN or Serpukhov. The array will also be tested at an RFQ calibration test stand at Caltech or AccSys. The two year subsystem research and development program (1991-1992) will focus on the following aspects [5]:

- Mass production of high quality BaF_2 crystals at a fixed cost of \$2.5/cm^3 at SIC, BGRI and LSORI.
- Crystal quality control and radiation hardness tests at SIC and BGRI, LSORI and LNPI, Caltech, BNL, and CMU.
- UV selective readout development at Los Alamos, Caltech, Oak Ridge, BNL, Princeton, and RWTH Aachen.
- BaF_2 prototype crystal array construction at Caltech, Oak Ridge, Los Alamos, CMU, and RWTH Aachen.
- An accurate RFQ calibration facility at AccSys and Caltech; and a monitoring system with a UV laser

Table VI.2: Schedule and Milestones for BaF_2 R&D

Milestone	1991	1992
Crystal Production		
Delivery of the first 50 Crystal Pairs		
Delivery of the second 50 Crystal Pairs		
Delivery of the last 60 Crystal Pairs		
Photodetector & Readout Development		
Test Vacuum Photodiode		
Decision on Photodetector Choice		
BNL Design Readout Test with R4406		
New Readout Design		
Test New Readout Design		
Complete 160 Channel Readout		
Prototype Test		
Mechanical Support Design		
Construction of Mechanical Support		
Construction of a full-size prototype		
Test Beam & Data Analysis		
Physics and Detector Simulation		
Final Choice of EM Calorimeter Option		

and quartz fibers at CMU, RWTH Aachen and Caltech.

- Test beam and cosmic-ray test bench setups at Oak Ridge, Los Alamos, Caltech, CMU, and RWTH Aachen.
- Completion of the engineering design, including a section of the final carbon fiber support as part of the prototype array at Oak Ridge and Caltech.

Table VI.2 summarizes the major milestones of the BaF_2 R&D program, and gives a schedule leading to the final selection of the electromagnetic calorimeter option.

C Liquid Xenon

C.1 Introduction

Liquid xenon is radiation hard and its scintillation light for electrons and photons is fast (decay time 20 ns, cf. [14]) and intense (4×10^7 photons/GeV at 170 nm, cf. [15]). The inherently large light output naturally results in excellent total energy ($\sigma(E)/E < 0.5\%$) and dE/dx measurements even with rather simple detectors. For these reasons, large LXe detectors have recently begun to be used in collider experiments.

Our recent research work [16, 17, 18, 19, 20] using α and heavy ion beams with MIT/Waseda 5 cm diameter silicon photodiodes and fast amplifiers has shown:

- Windowless UV photodiodes:
  1. We have developed large windowless silicon UV photodiodes to detect UV light in LXe.
  2. both diodes and amplifiers work well inside LXe
  3. the effective quantum efficiency > 50%
  4. 10 ns peaking time
  5. $\sigma(E)/E < 0.5\%$ at $E > 2.5$ GeV.
- Calibration: LXe detectors have large light output and can be calibrated using α's in situ, which has been verified using heavy ions.
- Uniformity: Monte Carlo studies show that adequate uniformity can be achieved.

Four US companies have stated that each of them can produce the required quantity of LXe at a price of ~\$2.5/cm^3. In addition, we are exploring the possibility of leasing the xenon or obtaining part of it from USSR.

C.2 Design of LXe Calorimeter

Side and the end views of the proposed detector are shown in Figure VI.2. The detector consists of a barrel and two endcaps giving a total of 14256 LXe cells with 3 photodiodes per cell. The side view (top) shows the structure of the vacuum and LXe vessels for both the barrel and the endcaps and the 3 diodes surrounded by reflectors in each cell; the cells all point toward the interaction point. The end views are composite sections showing (A) the cell structures and (B) the pipings and feedthroughs on the back of both the barrel and the endcaps. The overall dimensions are 4.6 m in length and 2.8 m in diameter. The depth of the active volume is 24.5 X_0 except in the central region $-0.5 < \eta < 0.5$, where it is about 22 X_0. The LXe is typically operated at 1.2 atm and -108 ± 0.5°C with the system monitored by the scintillating light from one α source per photodiode, thermal sensors, and pressure gauges.

Using three layers of thin photodiodes and fast amplifiers submersed in LXe, the detector is capable of measuring 3-D shower profiles. The transverse shower center can be determined to 1.5 mm in the second and third layers, yielding a photon vertex determination of ~ 0.7 cm. This is useful in selecting the correct vertex of photons at high luminosities when multiple events occur in a single crossing. The longitudinal shower profile is also a measurement of the rear energy leakage; thus it can be used to improve the energy resolution by adding a correction term, dependent on the back/front energy ratio, $E_3/(E_1 + E_2)$ (Figure VI.8). The resolution for 100 GeV electrons is 0.5% σ and 1.2% rms without correction and 0.25% σ and 0.7% rms with correction. Similarly, for 100 GeV γ's, the resolutions are 0.6% σ and 1.9% rms without correction and 0.3% σ and 1% rms with correction. The longitudinal shower measurement, together with the total energy and transverse shower profile measurements, yields an overall π/e suppression better than 10^{-4}.

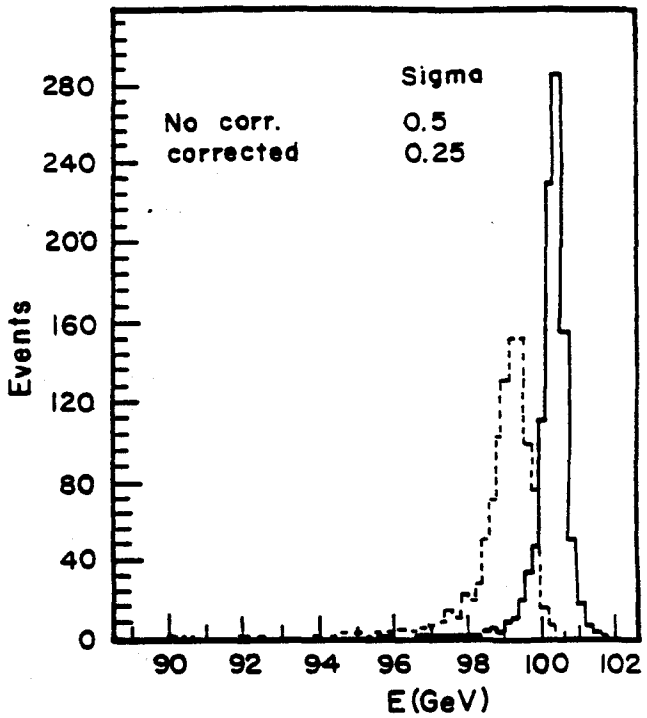

Figure VI.8: Monte Carlo predicted energy deposited in 22 X_0 of LXe for 100 GeV electrons. The dashed histogram is the sum of energy of 3 diodes, while the solid includes the correction due to back/front energy ratio.

The scintillation signals from nuclear spallation (e.g. slow protons) produced in hadron-nucleus inelastic scattering, are yet faster (light decay time of a few ns) and more intense ($7 \times 10^7\gamma$/GeV, cf. [15]) than those from electrons. Using a short gate (about 15 ns) to enhance the π signal relative to the electron signal to compensate the nuclear binding energy loss, it should be possible to make e/π ratio close to 1.

C.3 R&D Progress Since the EoI

Much work has been done since the EoI; the principal results are:

UV photodiodes

We have developed UV-sensitive windowless silicon diodes with a diameter of 5 cm. The diodes are 400 μm thick and the front surface is covered with fine gold meshes. The diodes are insensitive to magnetic fields and have an effective (i.e. average over the entire area of the diode, including gold mesh) quantum efficiency > 50%. Monte Carlo studies show that < 0.1% of the signal of an EM shower is due to particles passing through the three layers of silicon diodes in the proposed LXe calorimeter.

As shown in Figure VII.6 on p.69. of L* EoI, the leakage current of silicon detectors at −20°C increases only slightly after 10 Mrad of radiation. Tests of similar photodiodes show that the leakage current of diodes decreases by 10^6 in going from −20°C to −108°C (cf. [23]). We thus expect the leakage current at −108°C to be negligible even after this heavy radiation dose. The first 100 diodes for the beam test of the 5 × 5 cell LXe calorimeter are being produced at Waseda University.

Fast amplifiers

Fast amplifiers, developed by L* physicists at MIT ([16]), were used in beam tests at KEK and the Riken heavy ion accelerator, operate in LXe directly, and have a peaking time of 10 ns for the largest diode needed for the LXe calorimeter. The detector yields < 0.5% energy resolution for 2.5 GeV ^{27}Al ions. The fast amplifiers are situated behind the last (largest) diode. The present MIT amplifier is linear up to 2×10^9 electrons or 100 GeV. The first 100 amplifiers are being produced at MIT.

UV reflecting cell walls

We have constructed 3 × 3 UV reflectors using 100 μm aluminum foils, welded flat piece by piece using electron guns, and then expanded into shape. These metal reflectors also serve as Faraday shields for individual cells to reduce cross talk and noise. Assuming a reflectivity of 0.88 at 170 nm [21] for the mirrors in a 30 cm long section and darkening the ~ 1 cm nearest the diode, Monte Carlo studies show uniformity (Figure VI.9) better than the average for the L3-BGO crystals which have proven excellent energy resolution. The reflectivity of various mirrors is currently being measured using a VUV spectrometer at Osaka University.

Calibration using α Particles in situ

We have determined the photoelectron yield and studied calibration methods for LXe detectors using 5.49 MeV α's [16, 17]. The measured pulse height of photoelectrons corresponds to 4×10^4 electrons with a resolution, dominated by the electronic noise of the amplifier, of 6.6% (3 μs gate time) and 17% (20 ns). The temperature dependence of the scintillation yield, in the temperature

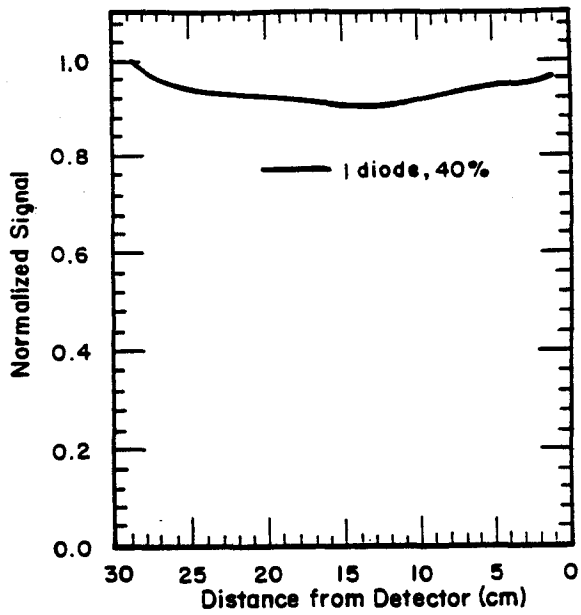

Figure VI.9: Monte Carlo prediction of signal uniformity versus distance from the large end of a 30 cm long cell section.

region around −108°C is about −0.4%/°C. When α's stop directly in the diode, the width of the pulse height distribution is 0.5% with 3 μs gate time and 1.5% with 20 ns [17]. The α spectra are very stable and, therefore, one can use two α sources, (one situated in LXe and the other directly on the diode), to calibrate in situ, after the detectors have been cross calibrated in beams Figure VI.10.

Resolution measured with Heavy Ion Beams

We determine the intrinsic energy resolution of a LXe detector equipped with full size (5 cm diameter) silicon photodiodes using ion beams from the Ring Cyclotron at Riken, Japan [16, 18]. The observed energy resolution was 0.6% rms for 1.64 GeV ^{14}N, and 0.7% for 2.65 GeV ^{40}Ar. The charge observed is 2.91×10^7 electrons for 2.65 GeV ^{40}Ar.

To estimate the intrinsic resolution of LXe detectors, to demonstrate the calibration method and to test the reliability of the detectors, we baked the same diode used for the above measurements until the quantum efficiency of the diode, calibrated using α's as described earlier, dropped to 50% of its previous value. We repeated the measurement using 2.47 GeV ^{27}Al ions 2 months after the previous Ar ion tests. Indeed the charge observed is reduced to 1.36×10^7 electrons (Figure VI.11), exactly corresponding to the decrease in quantum efficiency. The measured energy resolution without corrections improves slightly to 0.5% with 40 ns gate, due to better beam collimation. These results demonstrate that:

- the calibration method with α's does work;
- the measured energy resolution is mainly due to beam energy spread, not electronics or intrinsic

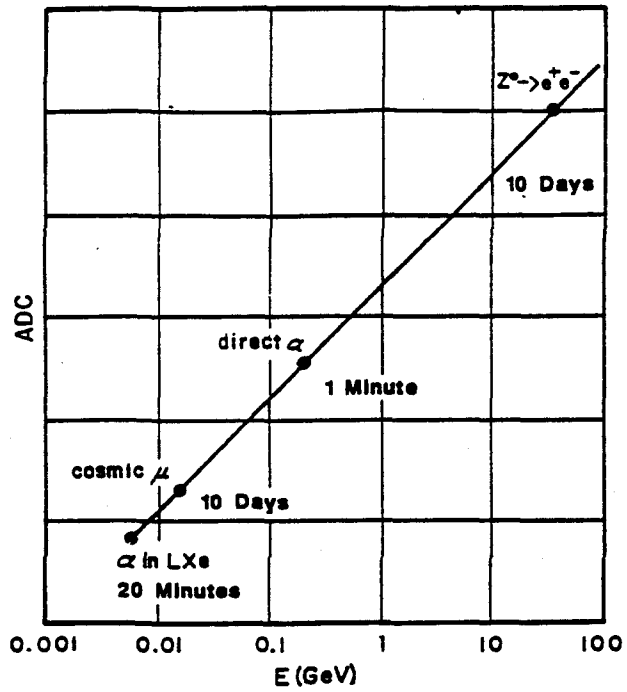

Figure VI.10: Calibration of liquid xenon detector using α particle in LXe and direct on the diodes, cosmic μ's, based on our measurements, and monitored by the RFQ and $Z \to ee$ events expected at the SSC. The time needed to achieve 0.5% accuracy of calibration is indicated for each data set.

photon statistics: the actual intrinsic energy resolution of LXe detectors may be much better.

Impurity Tests

We have studied the effect of impurities by filling two full size cells with commercial grade xenon with a few ppm O_2 equivalent impurity and found that scintillation works well even without any purification. The scintillation light yield of LXe remains stable at a level of a few times 10^7/GeV [20], for an impurity level from a few ppb to a few ppm. Our presently designed purification system, using getters, molecular sieves and oxysorbors should be adequate for scintillation. The purification system for the 5 × 5 cell detector is being built by Columbia University and Plasma Fusion Center of MIT.

C.4 Xenon Availability

Four commercial companies: Air Liquide, Matheson, Spectra Gases and Union Carbide, have submitted letters stating that each of them can produce up to 15 m^3 of additional LXe by 1999 at a price of about 2.5 \$/cm^3. For example, Air Liquide (cf. [25]) reported that it can produce up to 20 m^3 based on existing air liquefaction plants by 1999. We are discussing with vendors the possibility of leasing 16 m^3 of LXe as well as exploring the availability of LXe in the USSR.

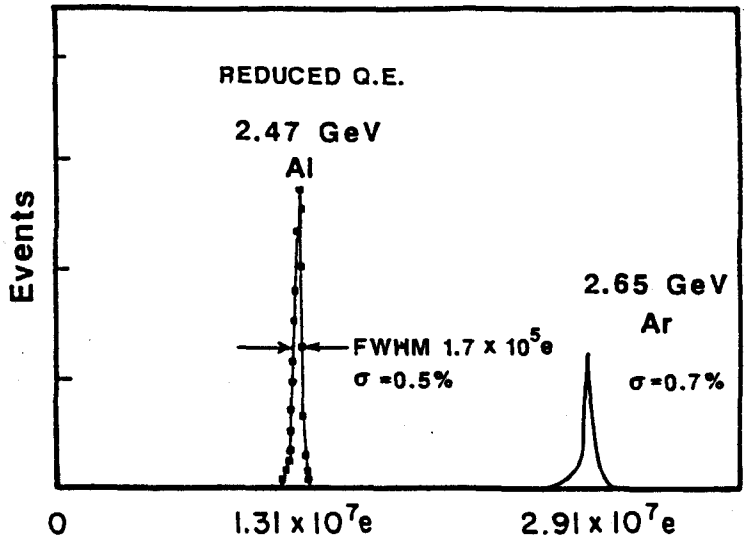

Figure VI.11: Measured numbers of photo-electrons for 2.65 GeV Ar ions (solid); and 2.47 GeV Al ions (connected points) with 50% reduced quantum efficiency, showing that the resolution is not limited by photo-electron statistics.

C.5 R&D Program

The present development program of the LXe Project is coordinated by MIT and aims at:

- measurements of fully contained high energy electron showers using a 5 × 5 matrix of LXe cells in 1991,
- fully contained 100 GeV pion showers using an 11 × 11 LXe cell detector (with a hadron calorimeter behind) in late 1992 and early 1993,
- these tests will determine the procedure for fabrication and assembly of the full EM calorimeter.

and is organized by tasks as follows:

1. Production of fast amplifiers at MIT and RWTH Aachen.
2. Mass production of UV photodiodes: Waseda University, MIT, SIC, Institute of Atomic Energy of China, and Hamamatsu.
3. α sources: Livermore and Los Alamos.
4. Purification: Columbia University and MIT.
5. UV reflectors: Aachen, NIST, Osaka.
6. Cryostats: MIT, KEK, ITEP and Aachen.
7. Procurement of xenon: MIT.
8. Radiation and magnetic field tests: MIT.
9. Beam tests: KEK, Riken, and CERN.

The development plan from current single cell full size LXe detector to L* EM calorimeter is summarized in Figure VI.12.

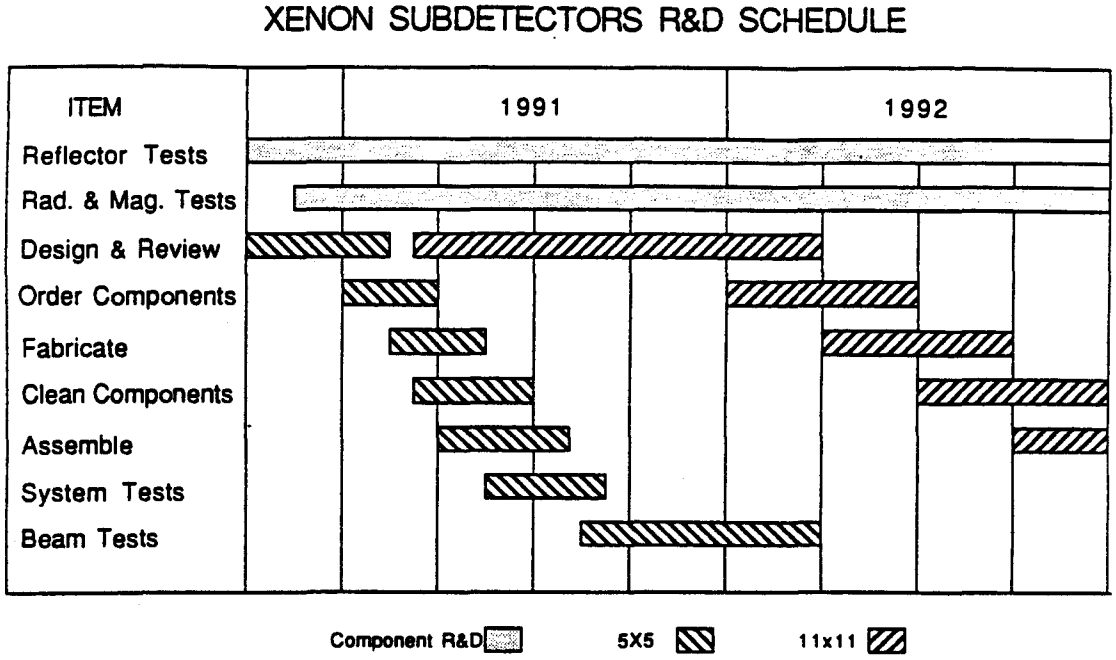

Figure VI.12: Development plan for LXe EM calorimeter

D Choice of Electromagnetic Calorimeter

We have discussed with the SSC Laboratory the latest time at which a decision on the choice of the electromagnetic calorimeter must be made. The choice of option will be made based on the R&D milestones of the two options. The final choice will be made in consultation with SSCL management on Dec. 1, 1992.

References

[1] CERN Green Book, *ECFA Workshop on LEP 200*, Aachen, September, 1986.

[2] *ECFA Workshop on LHC*, Aachen, October, 1990; *Snowmass Summer Study*, Snowmass, July, 1990.

[3] L* Collaboration, *Response to the Program Advisory Committee of the SSCL*, July 1990.

[4] L* Collaboration, *Expression of Interest to the Superconducting SuperCollider Laboratory*, May 1990.

[5] Caltech *et al.*, *A Precision BaF_2 Crystal Calorimeter for Superconducting SuperCollider*, a subsystem R&D proposal submitted to the SSCL, September 1990.

[6] SIC and BGRI, *Letter of Intent for Production of the Full Quantity of BaF_2 Crystals for the L* Detector*, September, 1990.

[7] Hamamatsu, *Technical Data for Triode R4406*, 1990.

[8] S. Suzuki, private communication.

[9] C. Woody *et al.*, SSC Detector R&D Symposium, Fort Worth 1990.

[10] See for example, P. LeCoq *et al.*, talk presented at the ECFA/LHC Meeting on Detector R&D, Aachen, 90.

[11] Z. Wei *et al.*, **CALT-68-1659**, 1990, submitted to *Nucl. Instr. and Meth.*

[12] Z. Wei *et al.*, **CALT-68-1628**, 1990, accepted by *Nucl. Instr. and Meth.*;
R.Y. Zhu *et al.*, **CALT-68-1392**, accepted by *Nucl. Instr. and Meth.*;
T.Q. Zhou *et al.*, *Nucl. Instr. and Meth.* **A258** (1987) 464.

[13] R.Y. Zhu *et al.*, *Super Collider I*, Plenum Press, edited by McAshan, (1989) 587;
H. Ma *et al.*, *Nucl. Instr. and Meth.* **A274** (1989) 113; and *Nucl. Instr. and Meth.* **A281** (1989) 469.

[14] T. Ypsilantis, ECFA/LHC Meeting on Detector R&D, Aachen, 90; and LAA Progress Report, CERN 90/1.

[15] M. Chen *et al.*, ECFA Workshop, CERN 89-10, 1989.

[16] M. Chen *et al.*, The Xenon Prototype Detector Subsystem Proposal, 1989 and 1990.

[17] M. Gaudreau *et al.*, MIT-LNS Tech. Rep. # 174, 1990;
T. Doke *et al.*, MIT-LNS Tech. Rep. #175, 1990;
S. Sugimoto *et al.*, OULNS 90-2, Osaka Univ., 1990.
M. Gaudreau *et al.*, OULNS Rep. 90-01, 1990;
S. Sugimoto *et al.*, OULNS Rep. 90-02, 1990.

[18] T. Doke *et al.*, SCH-PL Note KM-SIPD-3, July 1990.
T. Doke *et al.*, SCH-PL Note KM-SIPD-4, Oct. 1990.

[19] M. Miyajima *et al.*, Japanese Physical Society Meeting at Osaka, March, 1990.

[20] S.Sugimoto, M.Miyajima, S.Sasaki, and H.Tawara, Osaka Univ. OULNS 90-8, June 30, 1990.

[21] Measured mean reflectivity of the 300 RICH counters used by DELPHI at LEP, P. Baillon et al., Nucl. Instr. & Meth. A276 (89) 492 and 277 (89) 338.

[22] L3 collaboration, B. Adeva *et al.*, Nucl. Instr. and Meth. A **289** (1990) 35 .

[23] G. Hall, Prospects for Silicon Detectors in the 1990s. Blackett Laboratory, Imperial College preprint, 1990.

[24] K. Masuda *et al.*, NIM **188** (1981) 629; E. Aprile et al., submitted to NIM, July, 1990.

[25] D. Nachreiner, SSC Detector R&D Workshop, 1990.

Figure VII.1 L* Tracker System: Side View

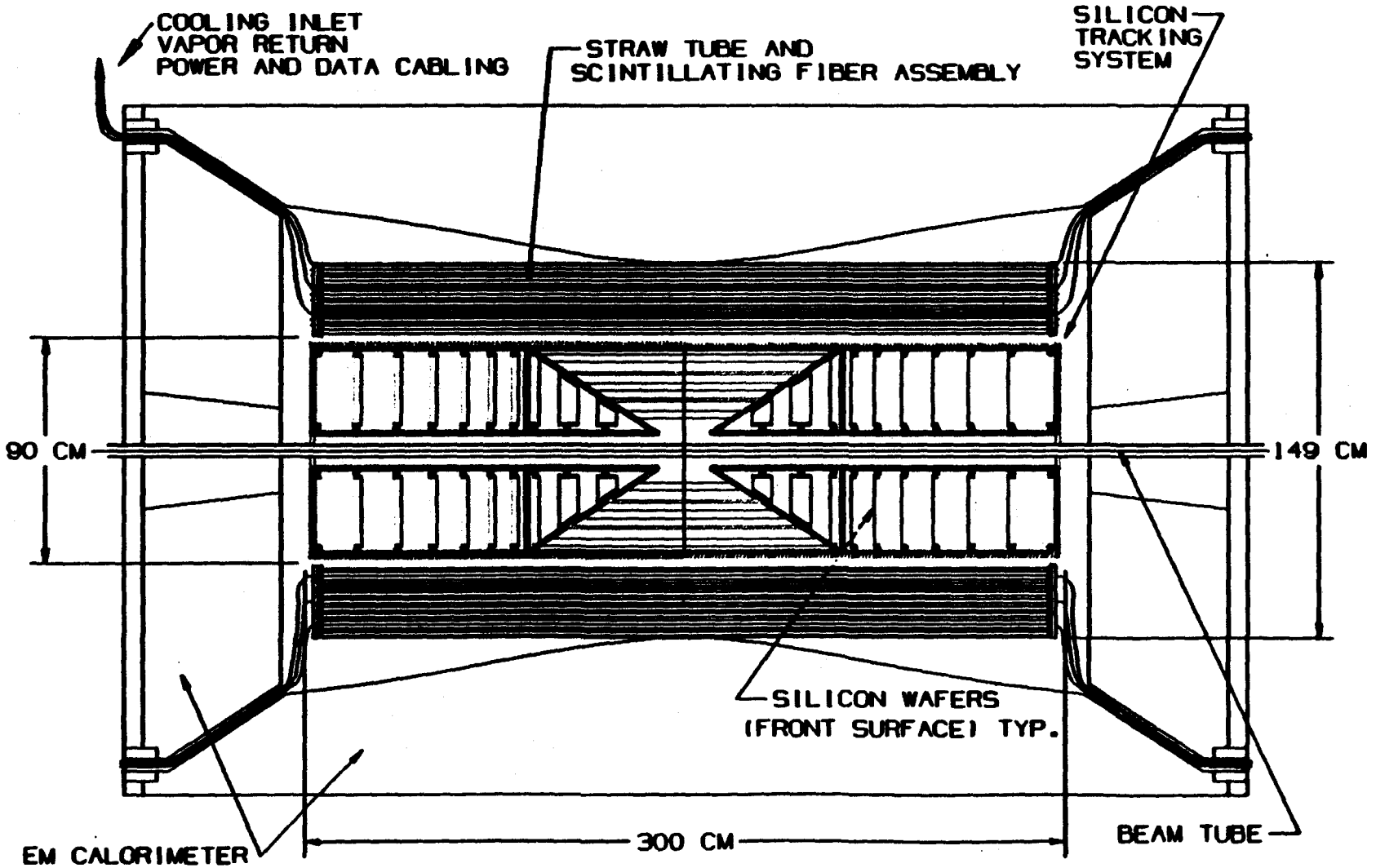

Figure VII.2 L* Central Tracker: End View

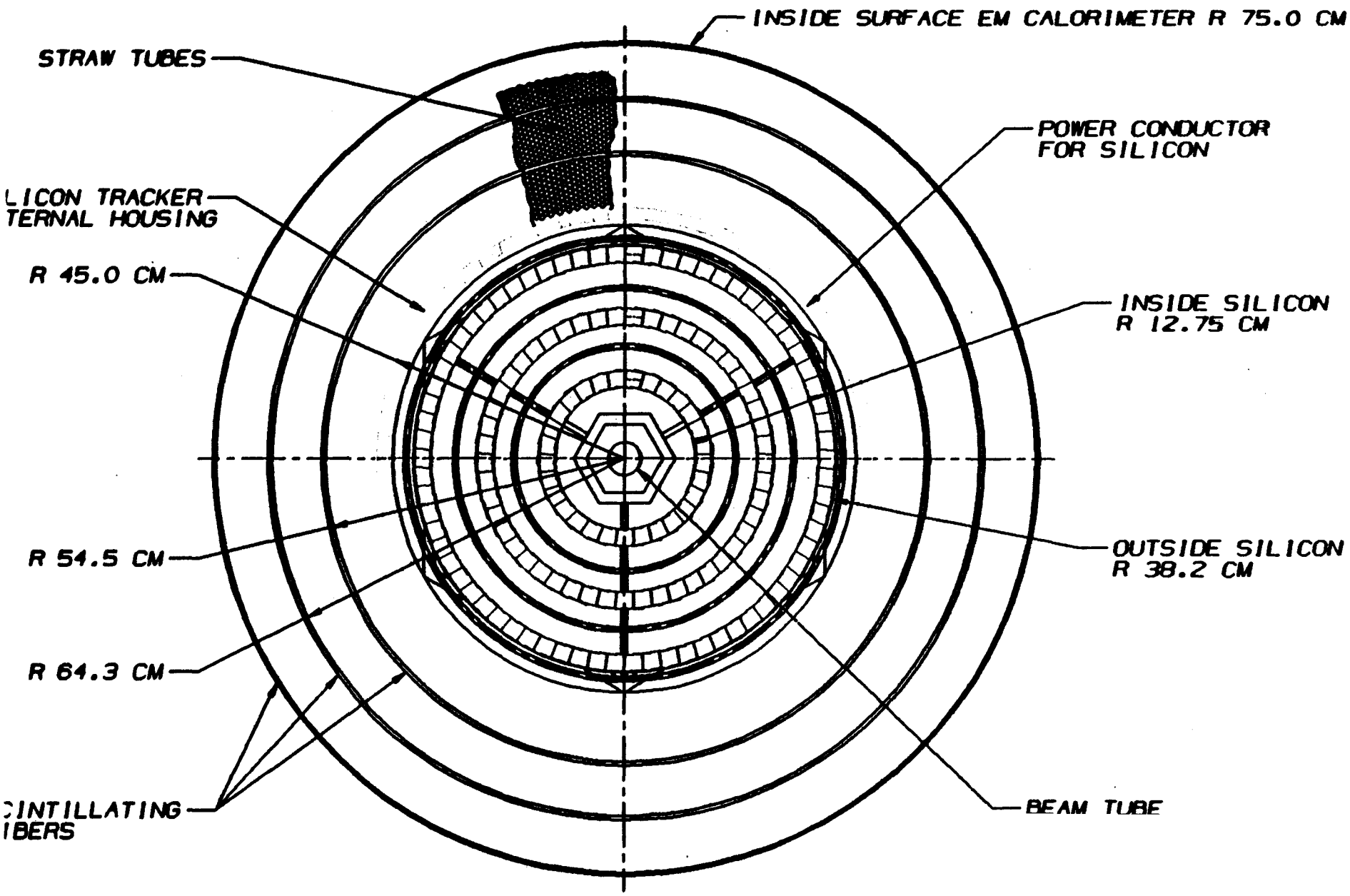

VII Central Tracker

A Introduction

Since the EoI [1] for L* considerable progress has been made in advancing the design of the central tracker. Modifications have been made to reduce the cost and the vulnerability to radiation damage.

The primary changes since the EoI are:

- The silicon inner radius has been increased from 10 cm to 12.75 cm to reduce radiation damage of the inner layers.
- The pitch of the outermost layers of the silicon detectors in the forward/backward regions has been increased, eliminating 15% of the strips and reducing cost.
- Our baseline design and cost estimate now assumes back-to-back single-sided silicon detectors, reducing the cost per unit area, and providing greater confidence of the radiation resistance.
- The number of fiber-superlayers has been reduced from 4 to 3, and the outermost layer will be constructed of 2 mm fibers, reducing costs and increasing light output and lifetime in the radiation field. This reduces the channel count by 25%, to 36,000.
- The number of straws has been reduced from 75,000 to 52,000 to reduce costs.

These modifications, and our active R&D programs, address the concerns expressed by the PAC.

B Configuration

The L* central tracker is shown in Figure VII.1 and VII.2. A summary of the key parameters of the L* central tracker is given in Table VII.1.

Table VII.1: Parameters for L* Central Tracker

ANGULAR COVERAGE:	5 degrees to 175 degrees
RADIATION LENGTH:	9% at 90 degrees
SILICON BARREL:	6 double layers from 12.75 cm to 38 cm from the beam 2 × 300 μm thickness/layer 25 μm pitch on inner 2 layers, 50 μm elsewhere 9.1 m^2 silicon area
SILICON END CAPS:	24 double annular discs (inner radius 10 cm, outer radius, 38 cm) with 12 discs from z = ±25 cm to ±140 cm 2 × 300 μm thickness/layer 50 μm pitch, except 100 μm pitch outer 4 discs 8.3 m^2 silicon area
STRAWS:	60 layers of straws from 45 cm to 72 cm from beam 4 mm straw diameter 2.8 m straw length single end read-out 52,000 straws
FIBERS:	3 superlayers (1 superlayer = 1u, 1v and 2z fibers) from 53 cm to 75 cm from beam 1 mm diameter fiber, except outer layer 2 mm 2.8 m fiber length double end readout with photomultiplier tube 36,000 fibers

C Physics Performance

The primary purpose of the central tracker is to provide charged particle tracking information for:

- Determination of the event vertex, to separate pile-up events from real events;
- Separation of photons from electrons;
- Measurement of charged particle multiplicity;
- Identification of secondary vertices of long lived particles;
- Measurement of charged particle momenta and charge sign to identify leptons, photons and hadronic jets.

The central tracker achieves these goals through the following features:

Speed: by gating the signal in less than 16 ns for silicon and scintillating fiber detectors, and about 20 ns for drift tube detectors;

Position Resolution: the vertex resolution in the r – ϕ plane, $\sigma_{r-\phi}$, is 20 μm and the z-coordinate, σ_z, is about 0.5 mm;

Pattern Recognition: track finding efficiency is larger than 96% for charged particle (p_T > 200 MeV) multiplicity up to 300;

Precision Momentum Measurement: momentum can be determined to $\Delta p/p$ = 55% at 500 GeV at 90 degrees by tracking particles in the L* central magnetic field (1.0 T).

The modifications described above have had a negligible effect on the central tracker performance, because of the increase in the magnetic field of the central tracker region from 0.75 T to 1.0 T since the EoI. The physics performance of the current central tracker is depicted in Figures VII.3 to VII.5. Figure VII.3 shows the momentum resolution at 90 degrees for magnetic fields of 1.0 T (conventional magnet with the thin tracker solenoid)

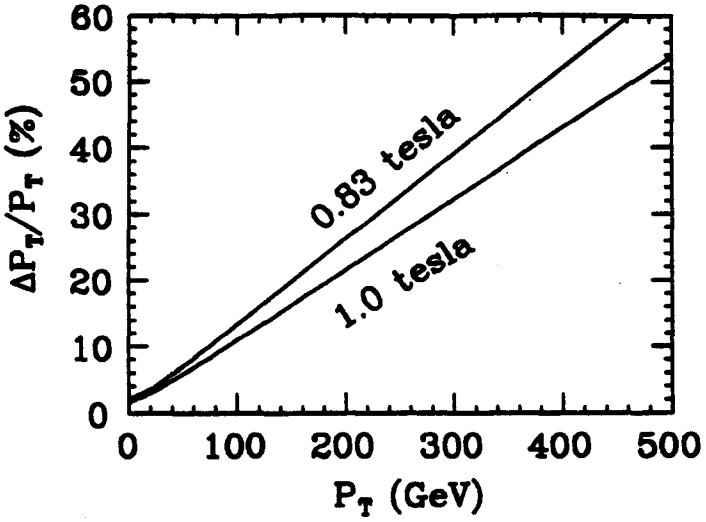

Figure VII.3: Momentum Resolution of the Central Tracker

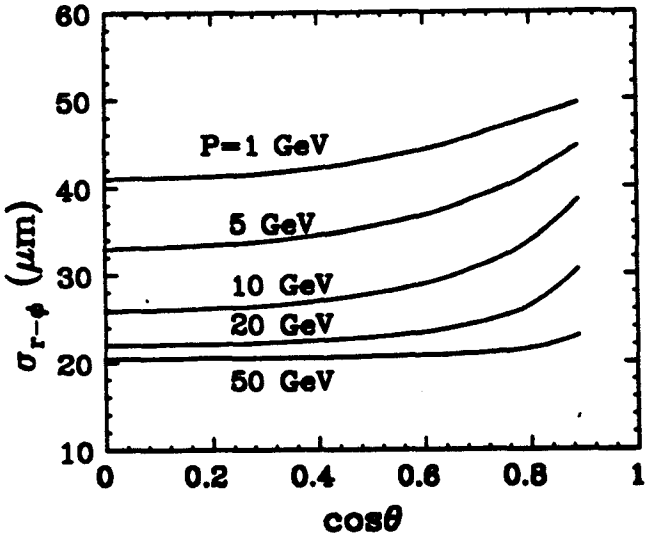

Figure VII.4: Vertex Resolution ($r-\phi$) versus $\cos\theta$, where θ is the angle with respect to the beam.

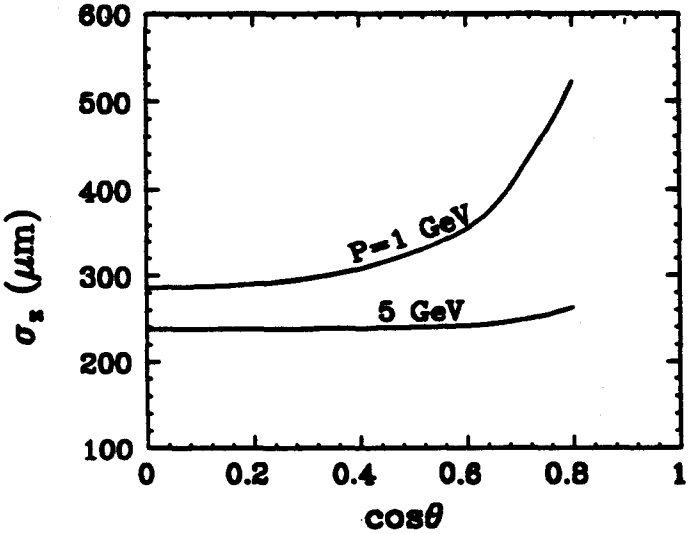

Figure VII.5: Vertex Resolution (z) versus $\cos\theta$, where θ is the angle with respect to the beam.

and 0.83 T (superconducting magnet). The vertex resolution is shown in Figures VII.4 (for $r-\phi$) and VII.5 (for z). In the transverse direction the resolution is about 20 μm at 50 GeV and the z resolution is about 1/2 mm.

The tracking system will provide an excellent means to identify leptons, photons, and hadronic jets at the SSC by measuring charged particle momenta and charge sign up to 500 GeV. This is necessary to search for the Higgs, new heavy quarks, new gauge bosons, and new phenomena in order to reject the very large background and to separate new sources of leptons or photons from QCD processes. From a detailed Monte Carlo study searching for new particles with more than 15 million simulated events, we have found that the only efficient way to reject fake muons (from punch-through or hadronic decays) and fake electrons (from neutral pion decay overlap with charged pions) is the matching of the momentum measured in the tracker with that measured in the outer muon chambers, or with the energy measured in the EM calorimeter. These results are described in Chapter X.

D Detector Quality Criteria

To achieve the various physics objectives described above requires the detector components to perform with precision and reliability and to be stable over several years at the SSC in the intense radiation environment encountered there. The performance criteria are shown in Table VII.2.

Table VII.2: Performance Criteria

SILICON:	Resolution = 7 μm (25 μm pitch), 14 μm (50 μm pitch), 29 μm (100 μm pitch) Systematic uncertainty = 10 μm Signal duration < 10 ns
STRAWS:	Resolution = 75 μm /straw Systematic uncertainty = 25 μm Signal duration < 10 ns Maximum drift time = 20 ns
FIBERS:	Resolution = 290 μm /fiber (for 1 mm diameter) Systematic uncertainty = 100 μm Signal duration < 10 ns Light level > 60 photons for near end hit, > 8 photons for mid-fiber hit (0.7 m attenuation length)

Short drift times in the straws can be achieved with an 80% CF_4–20% isobutane mixture (20 ns maximum drift time at B = 0.83 T). Since the diffusion limit for this gas mixture is 40 μm, we believe 75 μm resolution is a realistic goal. Preliminary engineering studies at Los Alamos and Oak Ridge indicate that the quoted systematic errors on position are acceptable after doses of neutrons and gamma rays expected at the SSC [2].

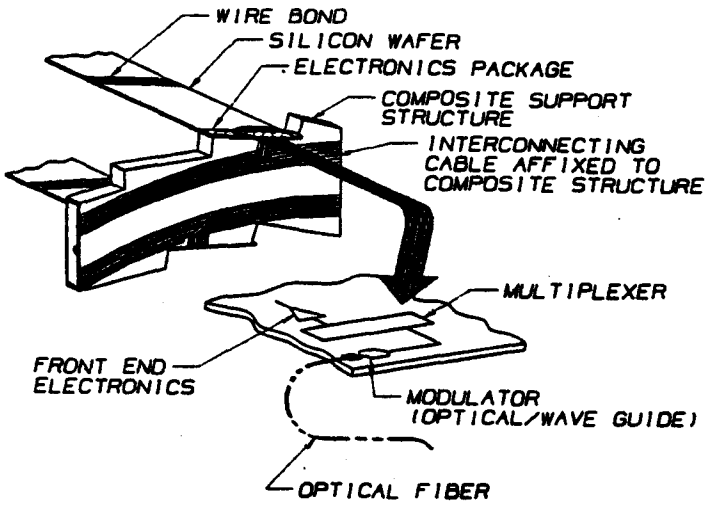

Figure VII.6: Electronics for power distribution and signal processing.

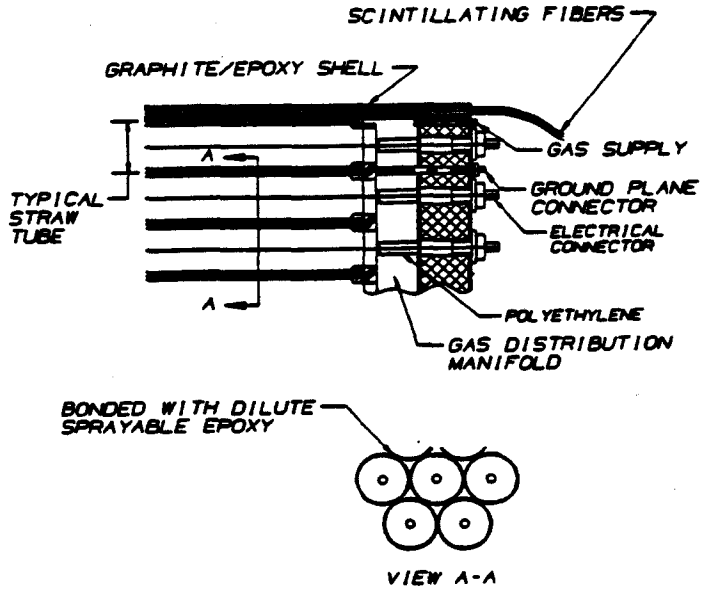

Figure VII.7: Straw/fiber components of the Central Tracker.

E Engineering for the Central Tracker

E.1 Silicon

The silicon wafers in the central and forward regions will be edge bonded into nominal 12 and 18 cm long strips. Electronics for power distribution and signal processing will be mounted at each end of the long strips (see Figure VII.6). The silicon layers in the central and forward region will be supported at discrete points between the end supports. The ends of the silicon will then be bonded to rings at each end which will provide support and passage for an internal heat pipe [3].

Integrating optoelectronics with the silicon microstrip detectors poses numerous system advantages; this development will be given high priority in our preconstruction R&D program. The key issues include the reliability and radiation resistance of the lithium niobate Mach-Zehnder interferometers and the GaAs alternative which control the transmission of optical signals. First radiation exposure tests of these modulators have been carried out at Los Alamos in October, 1990, with a more advanced test proposed in May, 1991.

E.2 Straws

An illustration of the straw/fiber component of the central tracker is shown in Figure VII.7. The baseline concept calls for graphite composite shells to support the wire tension of the straw system through graphite composite end plates. Mechanical engineering studies [2] have demonstrated that a carbon composite cylinder 3 m in diameter by 6 m long (twice as long and twice as large in diameter as the L* central tracker structural cylinders), having radial thickness of 0.3% of a radiation length, has a maximum deflection of about 10 μm, illustrating the suitability of such structures for maintaining the positional tolerance of a straw system.

E.3 Scintillating Fibers

Spiral wound scintillating fibers will be placed at the outer radial boundaries of each straw tube cluster. Each of these three superlayers will have two layers of fibers having a stereo angle of ± 6 degrees, and two layers of fibers at 0 degrees. The fibers will be integrated in the composite shells used for the straw support, maintaining the tolerances for fiber and straw placement.

We have two options for the readout of the scintillating fibers. One involves the use of Hamamatsu fine-mesh dynode multichannel photomultipliers (PMT's), which can be used in the L* magnetic field. The scintillating fibers would be connected to the PMT's by spliced clear optical fibers.

An alternative involves the use of avalanche photodiodes or solid-state photomultipliers. Disadvantages of this type of readout include the need for cryogenics and possible sensitivity to radiation.

Our baseline design currently relies on the PMT option, with readout of both ends of the fibers. This reduces the stringency of the attenuation length requirement for the fiber from a minimum value of 2 m to 0.7 m (assuring greater than 3 photoelectrons for hits anywhere on a 1 mm diameter fiber, 2.8 m in length). As seen below there is evidence for the reliability of a

two-end readout scheme for 10 years of operation at the SSC.

F Radiation Resistance

F.1 Silicon Strips

Los Alamos L* researchers, in collaboration with the silicon tracking subsystem R&D Program, have been involved with studies of the radiation resistance of silicon detectors. This work is addressing three issues:

1. The damage to the detectors themselves;
2. The damage to the front end electronics;
3. The effects of radiation on the mechanical properties of the materials that will be used to support the silicon detectors.

It has been found that radiation hard CMOS transistors are capable of withstanding up to 10^{15} neutrons/cm^2, and several Mrad of ionizing radiation [4]. It has also been found [5] that silicon microstrip detectors can be operated successfully up to several $\times 10^{13}$ protons (0.8 GeV)/cm^2 (about 1 Mrad), before increased leakage currents seriously degrade performance. By cooling the detector it is possible to extend lifetime by reducing leakage currents. This is a more effective method than annealing for extending the lifetime of a silicon detector in a large radiation environment.

F.2 Straw Tubes

It has been demonstrated that straw detectors are capable of surviving many years at the SSC (see [1, 6]).

F.3 Scintillating Fibers

Signal levels in straws and silicon are satisfactory as one has large numbers of primary electrons to work with, but this is a concern for fibers since the number of scintillation photons which are piped through a small fiber is low. However, several radiation hard fibers now exist which have good scintillation efficiency (Optectron S101S fibers, 1 mm in diameter, yield more than 16 photons with wavelength of 430 nm up to 2 m from the fiber end, with an attenuation length of 2 m) and adequate radiation sensitivity. Figure VII.8 shows measurements recently made by the Boston University L* group of attenuation length of Bicron RH-1 (a blue fiber 1 mm in diameter) for two neutron exposures. These are the first measurements made with neutrons of which we are aware. Figure VII.8 implies that no degradation occurs for a calculated [7] one year exposure in the L* central cavity (2×10^{13} neutrons/cm^2), and that fibers could be used for greater than ten years operation at the SSC with double end readout (damage would reduce the attenuation length to 1 m due to neutrons after 10 years).

Table VII.3 summarizes electron dose and neutron dose radiation studies of RH-1 fibers. It is seen that a dose of 0.26 Mrad of neutrons causes roughly equivalent damage as 1.2 Mrad of electrons.

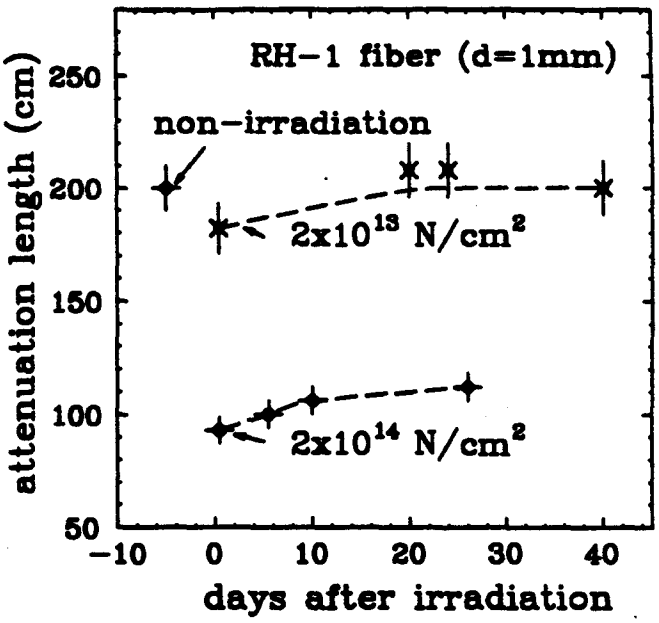

Figure VII.8: Measurement of neutron-induced radiation damage of scintillating fibers.

Table VII.3: Radiation Effects on RH-1 Fibers

Dose (Mrad)	Type	Recovery (day)	λ (m)	Light Loss (%)
0 (A)	e		2.00	0
1.2 (A)	e	2	1.00	1.6
3 (A)	e	2	0.55	3.0
10 (A)	e	2	0.60	10.0
0 (B)	n		2.00	
0.026 (B)	n	14	1.87	
0.26 (B)	n	10	1.06	

(A) Hybrid Central Tracking Collaboration results [2] for electrons

(B) Boston University L* Group results for neutrons

λ = Attenuation Length

G Calculations of Radiation Levels at the SSC

The Los Alamos L* group has carried out calculations of the neutron fluence in the central tracker region of L* to ascertain the surviveability of the central tracker over a several year period at the SSC [1, 7].

These calculations show that in one SSC year at 10^{33}cm^{-2}s^{-1} luminosity, total neutron flux in the central tracker region is of the order of 2×10^{13} neutrons/cm^2 (about 20% of these have energies in excess of 100 keV, the approximate threshold for inflicting serious damage to silicon detectors).

With the addition of several cm of a boron/polyethylene shield between the central tracker and the

Table VII.4: Durability of Straws and Fibers

Radiation Parameter	Standard SSC Conditions 45 cm from Beam	Tested And OK at:
Straw Charged Particle Rate	3.9 MHz	
Straw Photon Conversion Rate	0.4 MHz	
Straw Neutron Rate	10.1 kHz	
Total Straw Rate (A)	4.3 MHz	5.0 MHz
Straw Rate/cm (A)	0.02 MHz/cm	0.25 MHz/cm
Straw Ageing (B)	0.02 Coul/cm	1.4 Coul/cm
Straw Electronic Dose (B)	20 krad	500 krad
Straw Neutron Dose (A)	27 krad	860 krad
Straw Neutron Fluence (A)	$2 \times 10^{13}/cm^2$	$60 \times 10^{13}/cm^2$
Fiber Charged Particle Rate	1.0 MHz	
Fiber Photon Conversion Rate	0.1 MHz	
Fiber Neutron Rate	336 kHz	
Total Fiber Rate	1.5 MHz	20 MHz
Fiber Electronic Dose (B)	20 krad	1200 krad
Fiber Neutron Dose (A)	27 krad	260 krad
Fiber Neutron Fluence	$2 \times 10^{13}/cm^2$	$20 \times 10^{13}/cm^2$

NOTE:
(A) = Boston University L* Group
(B) = Hybrid Central Tracking Collaboration
Standard SSC Conditions = 10^7 sec at $10^{33}/(cm^2-s)$
Straw Length = Fiber Length = 2.8 m

Durability of Silicon

Radiation Parameter	SSC Year 13 cm From Beam	Tested and OK at:
Strip Charged Particle Rate	86 kHz	20 MHz
Strip Electronic Dose (SiTSC)	250 krad	1000 krad
Strip Fast Neutron Fluence	$4 \times 10^{12}/cm^2$	$20 \times 10^{12}/cm^2$

NOTE: SiTSC = Silicon Tracking Subsystem Collaboration
Silicon Strip Length = 41 cm,
Silicon Pitch = 25 microns

electromagnetic calorimeter it is possible to reduce the fast neutron flux from the calorimeter by a factor of 2.5. We may use such a shield. A neutron shield would also improve the effective lifetime of scintillating fibers at the SSC.

Based upon existing radiation damage data [8], assuming use of neutron shielding, reading out scintillating fibers at both ends (to reduce sensitivity to deterioration of attenuation length), and by optimizing the neutron leakage paths out of the central tracker region, one can operate the L* central tracker for 10 years at the SSC with no further improvements in detector radiation resistance. Summaries of radiation durability of straws, fibers and silicon (without a neutron shield) are given in Table VII.4.

Table VII.5: Occupancies of Straws in L* Central Tracker

Radius (cm)	Length (m)	Diameter (mm)	Rapidity range	Occupancy (%)
45	2.8	4	3.7	7.3
55	2.8	4	3.3	5.3
65	2.8	4	3.0	4.1
75	2.8	4	2.8	3.3

Finally, we show straw occupancies at several radii in Table VII.5. We calculate these using the technique of [9], assuming a 20 ns resolving time for a drift tube (this would be 30 ns for a 2 T field, and 18 ns for no magnetic field), 10% photon conversion probability in the silicon tracker, and negligible numbers of loopers ($\lesssim$ 3% calculated due to the relatively small radius and magnetic field of the L* central tracker).

H R&D Organization and Milestones

The institutions which are participants in the R&D programs for the central tracker and their responsibilities are listed in Table VII.6. Table VII.7 shows the schedule for R&D which will lead to the final design of the central tracker.

Table VII.6: Tasks and Institutes for L*Central Tracker

Tasks	Institutes (Lead Institute First)
Silicon Detector Development	Los Alamos in collaboration with Sandia Lab
Straw System Development	Boston U., Indiana U., Los Alamos
Fiber System Development	Boston U., U. of Utah, ITEP, Los Alamos, in collaboration with UCLA
Mechanical Engineering	Los Alamos, Boston U., Lawrence Livermore National Laboratory
Development of Radiation hard electronics and optoelectronic readout	Los Alamos, Indiana U. in collaboration with Sandia Lab.
Computer Simulations	Los Alamos, Boston U., Indiana U.

References

[1] L* Collaboration, Expression of Interest to the SSC, Chapter 7 (May, 1990).
[2] The Hybrid Central Tracking Collaboration, Progress Report for 1990 (August, 1990).

Table VII.7: R&D Milestone

1991	1992	1993
• Evaluate Silicon Detectors • Optimize straw materials • Optimize Gas • Evaluate Fibers • Optimize Structural Components • Evaluate Front End Electronics for Silicon and Straws • Evaluate Fiber Readout • Evaluate Optoelectronic Readout for Silicon and Straws	• Complete readout design for silicon and straws • Select fiber type and Select readout option for fibers • Preliminary design of entire system • Stress and thermal analysis of preliminary design • Construction of prototype assemblies	• Final design of mechanics and electronics of Central Tracker • Resolution tests of prototype • Radiation tests of prototype • High rate tests of prototype • Detailed computer simulation for final design

[3] W. Miller, et.al., Superconducting Supercollider Silicon Tracking Subsystem Research and Development Interim Report, Los Alamos National Laboratory.

[4] J. Kapustinsky, H.F.-W. Sadrozinski et al., Symposium on Detector Research and Development for the Superconducting Super Collider, Ft. Worth, Texas, October 15–18, Nucl. Instr. Meth. Phys. Res. A288, 76 (1990).

[5] C.S. Mishra et al., preprint, 1990.

[6] B. Zhou et al, IEEE TNS Nucl. Sci. 37, #5, 1564 (1990); S. Ahlen, et.al., Particle World, Vol. 1., No. 6 (1990) 168.

[7] D.M. Lee, W.W. Kinnison, W.B. Wilson, "A Prediction of Neutron and Charges Particle Backgrounds in the L* Detector", Symposium on Detector Research and Development for the Superconducting Super Collider, Fort Worth, Texas, October 15–18, 1990.

[8] W. Dawes, Nucl. Instr. Meth. Phys. Res. A288, 54 (1990).

[9] G. Hansen et al, Nucl. Instr. Meth. Phys. Res. A283, 735 (1989).

VIII Data Acquisition and Trigger

A Introduction

There have been no significant changes in the trigger and data acquisition system philosophy since the EoI was published. Channel counts for all the detector subsystems have been reduced, following the instructions of the SSCL director and of the Program Advisory Committee to lower the L* subdetectors costs. Better estimates have also been developed of the electronics requirements in terms of rack space needs, power dissipation, and overall costs. The triggers will be based on E_t, P_t, missing P_t, isolated γ, e, μ, and jets, as was described in the EoI.

B Channel Count Summary

The channel count requirements are given in Table VIII.1.

Muon Chambers. Channel counts for the high precision muon chamber system have been reduced to 110,000 channels. Resistive plate chambers (RPC) will be used for fast trigger detection of high P_t particles. There will be 19,000 channels in this subsystem.

Hadron Calorimeter. The channel count has been reduced to 83,000, largely by reducing the longitudinal segmentation. The change in emphasis to the liquid scintillator technology has modified the requirements for front-end electronics, but shaping, pipelining and trigger requirements remain largely the same as in the EoI.

Electromagnetic Calorimeter. Channel count has been reduced to 18,000. This subsystem still has the most exacting speed and dynamic range requirements.

Central Tracker. The central tracker consists of a combination of 5,065 channels of silicon microstrip vertex detectors and a mixture of 52,000 channels of straw tubes and 36,000 channels of scintillating fibers to form the tracker outer layers.

Table VIII.1: Summary of Channel Count Requirements

Subsystem	Channel Count LoI	Channel Count EoI	Data Type
Si microvertex	5.1k	76k	Hit
Sci Fi tracker	36k	50k	Hit
Straw tube	52k	75k	TDC
Muon Chambers	110k	223k	TDC
RPC	19k	20k	Hit
Hadron Cal	83k	335k	ADC
EM Cal	18k	25k	ADC

C Trigger Philosophy

First Level (Prompt). We will continue to pursue a prompt first trigger with a latency time of less then one microsecond. This will place major constraints on the location of this trigger electronics, forcing it to be as close to the detector as possible. It will, however, reduce the length of pipeline storage. This will be crucial for the calorimetry subsystems, especially the EM section, with its very large dynamic range requirements.

Second Level. Over the next five years, while R&D and planning are being carried out, two generations of electronics will have come and gone in terms of speed, power, and signal density. Although we can visualize a general technology layout for the implementation of the higher level triggers, such as table lookup, fast digital signal processors (DSP), and neural networks, we cannot presently select the optimum technologies.

Data Routing. Because of the large number of signals and the very high data bandwidths, event data will be sent to a massively parallel array of computers via a switching network called the event builder. This intelligent network will route data from the various detector subsystems to the appropriate processors for each event.

Processor Farm. This is presently envisioned to be a large, massively parallel array of small computing elements. One present candidate is based on the "Transputer" concept of highly linkable processors.

Mass Storage. The writing of data to mass storage is foreseen to be $\sim$ 10 Mbyte/s. With advances in technology, data will be stored on just a few mass storage volumes per day. The storage medium may be either magnetic or optical.

D Rack and Counting Rooms

An estimate of the rack space requirement has been completed, including estimates of locations and power dissipation (cf. Table VIII.2.

Table VIII.2: Rack Count

	racks	dissipation [kW]
Experimental Hall	86	291
Counting room	184	941
Control room	45	45
Computers		100
Summary	315	1377

IX Engineering Integration

L* Planning

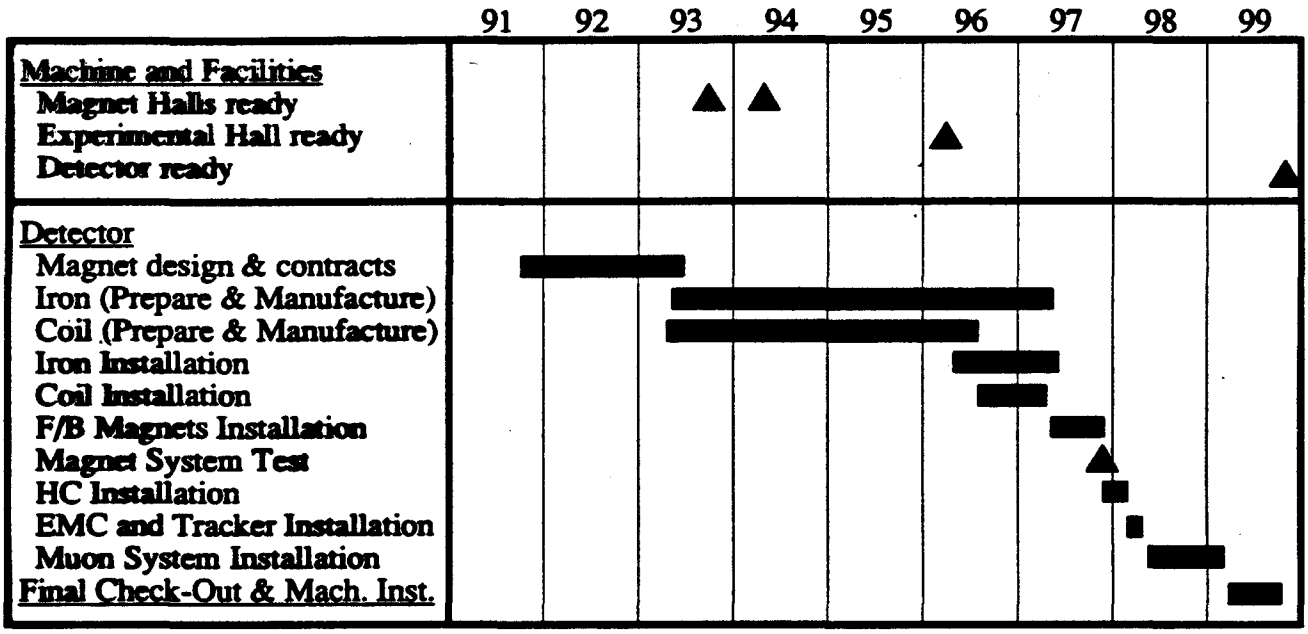

Figure IX.1 Construction and Installation Time Sequence

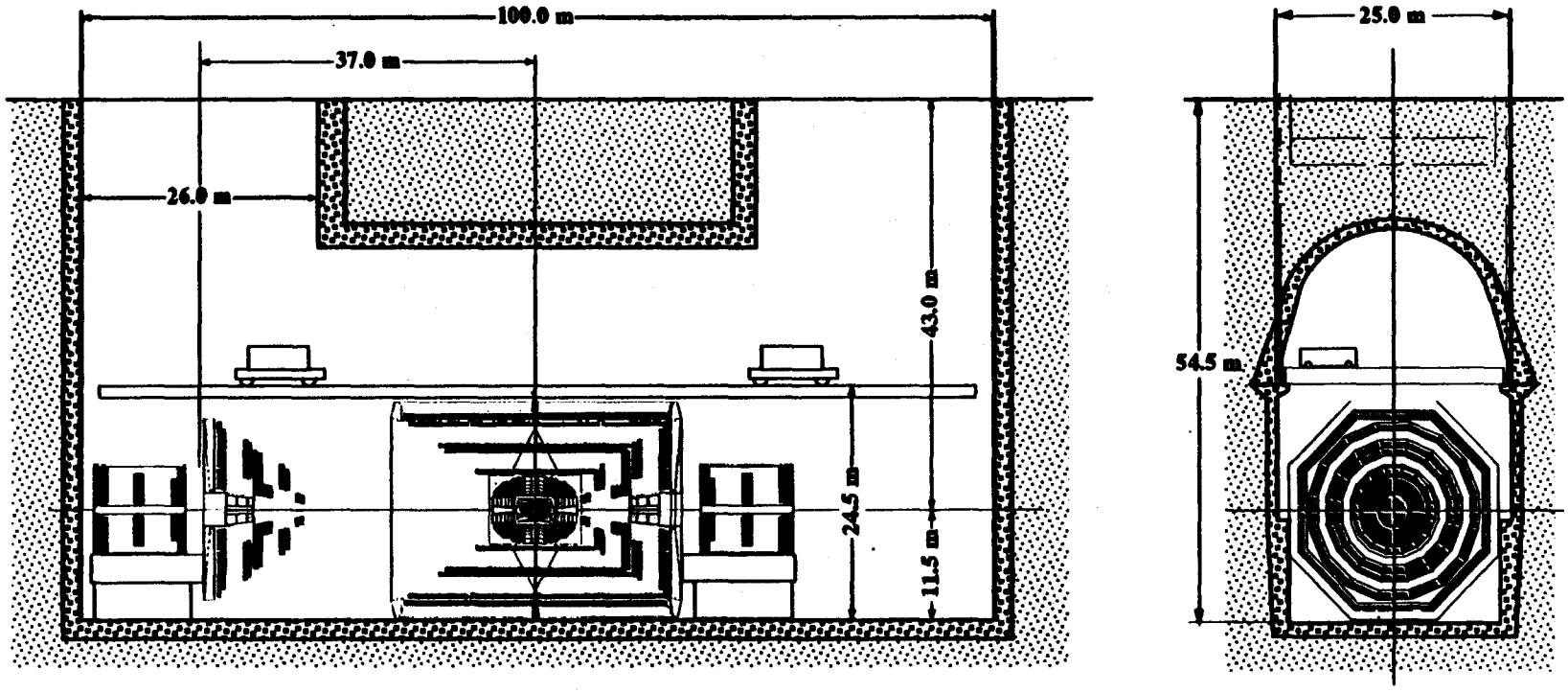

Figure IX.2 L* Underground Experimental Hall: Side and End Views

IX Engineering Integration

A Introduction

At this stage in the design process, the engineering integration activity has been primarily involved with technical issues relating to the fabrication, installation and assembly of the subsystems of the detector in the experimental hall and integration with the planning and schedule needs at the SSC site. In preparation for the construction project, a formal process has been defined to plan, execute and control the L* project. The approach is based on the use of a work breakdown structure (WBS) developed to be compatible with DOE guidelines and the system already in use at the SSCL. The WBS system has been used to organize the cost estimate given in Chapter XII.

B Work Breakdown Structure

The work breakdown structure for the L* project starts at the level of detector systems, 5.2.1 in the SSCL breakdown. The top two levels of breakdown for L* are listed in Table IX.1. Additional levels have been defined for the detector systems that are not shown here.

Table IX.1: L* Work Breakdown Structure

5.2.1.1.0	Project Management
1.1	Quality Assurance Program
1.2	Systems Engineering
1.3	Safety and Environment
1.4	Finance
1.5	Personnel
5.2.1.2.0	Detector Systems
2.1	Central Magnet Systems—Resistive Coil
2.2	Forward/Backward Magnet System
2.3	Muon Detector System
2.4	Hadron Calorimeter System
2.5	Electromagnetic Calorimeter System
2.6	Central Tracker System
2.7	Structural Support Systems
2.8	Trigger and Data Acquisition System
2.9	Central Magnet Systems—Superconducting
2.10	Tracker Coil
2.11	Forward Calorimeter System
5.2.1.3.0	Interface Systems
3.1	Experimental Hall
3.2	Surface Facilities
3.3	Process Utilities
3.4	Control Systems

C Facility Integration

The experimental hall arrangement is shown in Figure IX.2. There are several differences from the EoI design. The major difference is due to the reduction in the outside diameter of the magnet iron because 25 m has been chosen as the maximum experimental hall width in order to stay within conventional experience in civil engineering excavation.

Design of the underground hall has also been modified in order to reduce structural problems in shafts and openings required for assembly and access. The hall design described in the EoI had a large central opening in which the major magnet components were lowered for assembly. The new configuration with a maximum width of only 25 m, has a central cavern structure with access on either end by circular shafts. The advantage of this new design is that the majority of the underground excavation can be accomplished with tunnel drilling techniques, providing an alternative to open pit construction.

The installation and assembly of the magnet system is the only major difference from the overall assembly described in the EoI. The magnet system will now be installed from either end, with the magnet iron and aluminum coil sections lowered and translated into position. Once the magnet systems are installed and tested, the central tracking systems and muon chambers will be installed as described in the EoI.

D Planning and Schedule

The planning and schedule has been revised to take into account changes in the L* design and in the major milestones at the SSCL construction site. The construction milestones for the L* planning are given in Table IX.2.

Table IX.2: SSC Construction Milestones

2nd stage approval of the L* Experiment	12/15/91
Concrete Slab for Magnet Iron	08/01/93
First Magnet Fabrication Hall	10/01/93
Second Magnet Fabrication Hall	04/01/94
Muon Testing Hall	05/01/94
Experimental Hall	02/19/96

Using the L3 installation times as the model, detailed planning for the fabrication, assembly and installation of each detector subsystem has been laid out. A summary bar chart is shown in Figure IX.1. We have studied the planning in considerable detail since the EoI to show that it is feasible to meet the new SSC physics operation date of 10/99. The facilities required to meet this plan have been identified for preparation of the SSCL portion of the cost estimate. The information is

included in the update of the Resources Requirements Report.

E Milestones and Key Events

As requested in the Guidelines for the LoI, the key events that must occur to define the detailed design of the detector have been identified. For L*, the key events are related to the choice of technology options for the major subsystems. These events are described in the individual chapters of this report. As part of the project planning activity described above, the timing required for making the choices was integrated with the overall planning logic. A summary of the required dates for option selection is given in Table IX.3.

For the central magnet system, the choice between normal and superconducting technology must be made very early, since the magnet fabrication and assembly is the pacing item on the critical path of the schedule. The final decision must be made by the time the Technical Proposal is submitted, assumed to be October, 1991. All other technology choices as described in this report will be made as a part of the subsystem R&D programs.

Table IX.3: Key Decision Dates Required for Detailed Design

Choice of Central Magnet Technology	10/01/91
Choice of EM Calorimeter Option	12/01/92
Choice of Hadron Calorimeter Option	10/01/93

F Proposed Funding

We have previously reported to the PAC, in answer to Generic Question 6, the tasks and funding estimated to complete the Technical Proposal in FY 1991. Table IX.4 is a summary of that request. We have added to the table the names of the institutions and the lead engineer that will be responsible for each task area.

Table IX.4: FY 1991 Request for Engineering Design and Coordination

Task	Funding ($k)	Responsible	
Magnet	800	SSCL	I. Horvath
Muon Chambers	750	MIT	C. Grinnell
		LLNL	G. Deis
Hadron Calorimeters	800	ORNL	M. Rennich
EM Calorimeter	520	Caltech	H. Newman
		MIT	M. Chen
Central Tracker	520	LANL	G. Sanders
Data Acquisition	700	MIT	S. Ting
Coordination	500	ORNL	T. Shannon
Administration	395	MIT	F. Eppling
TOTAL	**4985**		

X Physics

A Introduction

We have studied the capabilities of the L* detector for various physics processes as requested by the PAC. Our results can be summarized as follows.

- L* will be able to detect the Higgs boson in one year at the SSC ($\int Ldt = 10^{40} cm^{-2}$) for masses above 80 GeV. The most promising decay modes are $H^0 \rightarrow \gamma\gamma$ for 80 GeV< M_{H^0} <160 GeV, and the four charged lepton channel for 140 GeV< M_{H^0} <800 GeV. In the high mass region ($M_{H^0} \sim$ 800 GeV), where the production cross section is small, we can also use the $\ell^+\ell^-\ \nu\bar{\nu}$ and $\ell^+\ell^-$ jet jet final states to increase the statistical significance of the signal.
- L* will be able to find a top quark with M_t = 250 GeV in one day with nominal SSC luminosity. We have studied events with multi-leptons and multi-jets. The top quark mass can be measured from hadronic jets with a precision of 2%. The top quark decay into charged Higgs bosons can be detected in one year for branching ratio product $Br(t \rightarrow H^+ + b)Br(H^+ \rightarrow c\bar{s}) > 0.5\%$. The charged Higgs mass can be measured with a precision of 2%.
- We have studied the jet energy resolution for a 800 GeV Higgs boson decay into Z^0Z^0 with one of the Z^0s decaying into jets. The Z^0 mass can be reconstructed with a resolution of 6%. The mass resolution for a 1 TeV Z' decaying into jets is 3%.
- We have analyzed Z' decays ($M_{Z'}$ = 4 TeV) into electron, muon and tau pairs. The acceptances are 93.6%, 97.8%, and 26.0%, respectively. The experimental Z' mass resolution is 0.5% in the e^+e^- channel and 17% in the muon channel. With 1000 Z' decays into each charged lepton channel we can measure the asymmetry with an error of 3%.

In the simulation of physics processes we have assumed a baseline design for the L* detector, which consists of a warm magnet, precision muon chambers, a lead liquid scintillator hadron calorimeter, a BaF_2 or LXe electromagnetic calorimeter, and an inner tracker. For some processes we also give the results for the superconducting coil option. The properties of the detector can be summarized as follows: The momentum resolution for muons with p=500 GeV is $\Delta p/p = 4.9\%$ at $\theta \approx 90°$ for the resistive coil and 2.8% for the superconducting coil option. The precision muon detector covers the angular range $2° < \theta < 178°$($|\ \eta\ | < 4.0$). The momentum resolution as function of $cos\theta$ is shown in Figure IV.2. The energy resolution for electrons and photons is $\Delta E/E = 1.3\%/\sqrt{E} + 0.5\%$ for $6.7° < \theta < 173.3°$, and $\Delta E/E = 17\%/\sqrt{E} + 1\%$ for $0.3° < \theta < 6.7°$. Hadronic jets can be reconstructed with an energy resolution of $\Delta E/E = 50\%\ /\sqrt{E} + 2\%$ for $0.3° < \theta < 179.7°$ ($|\ \eta\ | < 5.95$). The calorimeters have a granularity of $\Delta\eta \times \Delta\phi = 0.04 \times 0.04$ for the electromagnetic part and $\Delta\eta \times \Delta\phi = 0.05 \times 0.05$ for the hadronic part. The central tracker reconstructs particle momenta with a momentum resolution of $\Delta p/p$ = 11% for p=100 GeV at 90°.

The momentum of muons is measured in an air spectrometer after passage through the hadron absorber. This spectrometer allows us to identify muons reliably and measure their momentum precisely, even for muons inside hadronic jets. The comparison of momenta measured with the inner tracker and the muon spectrometer provides us with a powerful method to reduce background from π and K decays and punch through and muon background from the beam. Similarly a reliable identification of electrons is possible by requiring agreement between the momentum measured in the tracker and the energy deposited in the calorimeter. This also rejects electromagnetic background from the beam.

The L* detector allows a precise measurement of missing transverse energy, because of the large calorimeter coverage and the fine granularity. Pile-up effects are reduced due to the short pulse integration time (15 nsec).

In this study we have used similar methods as described earlier in the L* EoI [1] and the reply to the PAC [2]. For details of the simulation we refer to these reports. Present results differ slightly from earlier results due to modifications in the L* detector and improvements in event generators. We have used the Pythia 5.4 code[3] for $H^0 \rightarrow \gamma\gamma$ and Z' production, and the ISAJET 6.32 program [4] for other reactions.

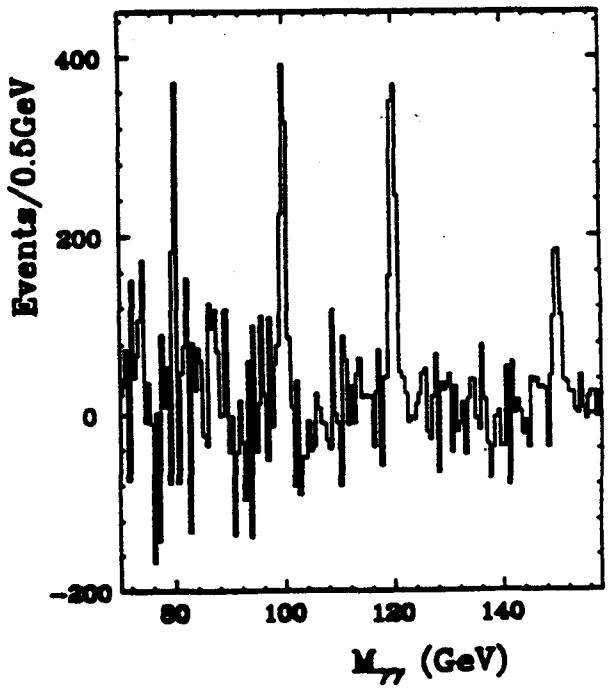

Figure X.1: Reconstructed $\gamma\gamma$ mass from $pp \rightarrow H^0 + X \rightarrow \gamma\gamma + X$ after background subtraction.

B Search for the Higgs Boson

The L3 detector at LEP will be able to set a mass limit up to M_Z before the start-up of the SSC. The unique physics potential at SSC will be to explore Higgs masses up to the TeV range. Our aim with the L* detector is to cover the complete mass region above 80 GeV, and to perform a definitive test of the symmetry breaking mechanism of the Standard Model.

B.1 80 GeV < M_{H0} < 180 GeV

For the mass region 80 < M_{H^0} < 180 GeV we use the following physics processes in the search for the Higgs boson.

- $p + p \rightarrow H^0(\rightarrow \gamma\gamma) + X$
  for the mass range 80 < M_{H^0} < 160 GeV.
- $p + p \rightarrow H^0(\rightarrow ZZ^* \rightarrow \ell^+\ell^-\ell^+\ell^-) + X$
  for the mass range 140 < M_{H^0} < 180 GeV.

$H^0 \rightarrow \gamma\gamma$

The task in this measurement is to reduce two types of background. The first is the so called *irreducible* background ($gg \rightarrow \gamma\gamma$ and $q\bar{q} \rightarrow \gamma\gamma$) and the second the copious production of π^0's and single hard photons in hadronic jets. The irreducible background can be suppressed with rapidity, energy and angular cuts ($|\eta_\gamma| < 2.8$, $|\eta_{\gamma\gamma}| < 3$, $E_T^\gamma > 20$ GeV, and $|\cos\theta_\gamma^*| < 0.8$). For the reduction of the second type of background isolation requirements are applied. They are used in our analysis to reduce background from hadronic jets. A particle (photon, electron or muon) is isolated if $\sum_R E_T - E_T^P < E_c + 0.1E_T^P$, where E_T^P is the transverse energy of the particle, E_T is the transverse energy of clusters found in the calorimeter, and E_c is the energy cut. The sum is taken inside a cone around the particle with radius $R = \sqrt{(\delta\eta)^2 + (\delta\phi)^2}$. In our isolation requirement for photons we use the parameters R=0.6 and E_c = 5 GeV.

The result of the analysis is shown in Figure X.1 for Higgs masses of 80, 100, 120 and 150 GeV after background subtraction. The expected significances of the signal in one year at the SSC ($\int Ldt = 10^{40} cm^{-2}$) are 5, 9, 15 and 14 standard deviations, respectively. The good energy resolution of the electromagnetic calorimeter is crucial to extract the narrow Higgs signal from the large background.

$H^0 \rightarrow ZZ^* \rightarrow \ell^+\ell^-\ \ell^+\ell^-$

The best signal for the Higgs boson in the mass range from 140 GeV to 180 GeV is the four lepton channel via the ZZ^* intermediate state. We have studied final states with *ee ee*, *ee* $\mu\mu$, and $\mu\mu$ $\mu\mu$. We select leptons with $p_T > 5$ GeV and $5° < \theta < 175°$. As explained earlier [2] the background from QCD jets and from $Z^0q\bar{q}$ production is suppressed by requiring that the leptons be isolated (R=0.3, E_c = 5 GeV). The Higgs mass spectra collected in one SSC year for the 4-lepton final state are shown in Figure X.2 for M_{H^0} = 150 GeV. Backgrounds are included in the figure. The Higgs signal is clearly separated from the background distribution. The figure shows the Higgs mass spectra for both magnet options. They are narrower for the superconducting version due to better muon resolution.

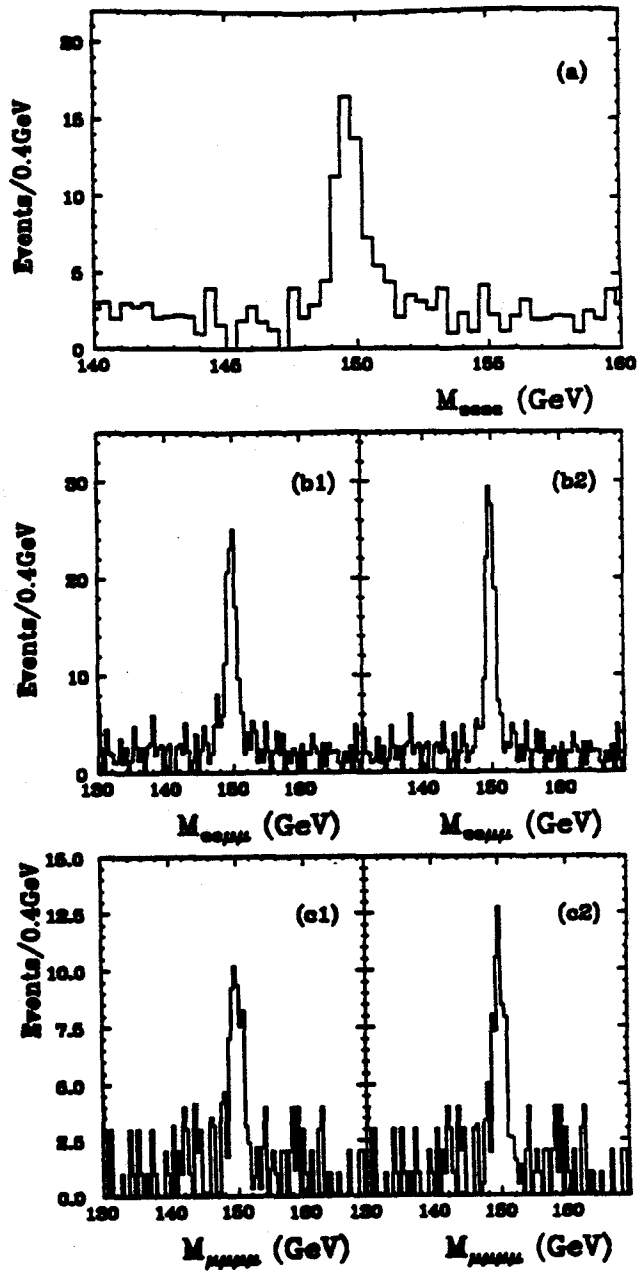

Figure X.2: $H^0 \rightarrow ZZ^* \rightarrow$ 4 leptons together with backgrounds for M_H = 150 GeV, (a) *ee ee*, (b) *ee* $\mu\mu$ and (c) $\mu\mu$ $\mu\mu$ decay channels. Figures b1 and c1 correspond to the resistive coil option, and b2, c2 to the superconducting magnet.

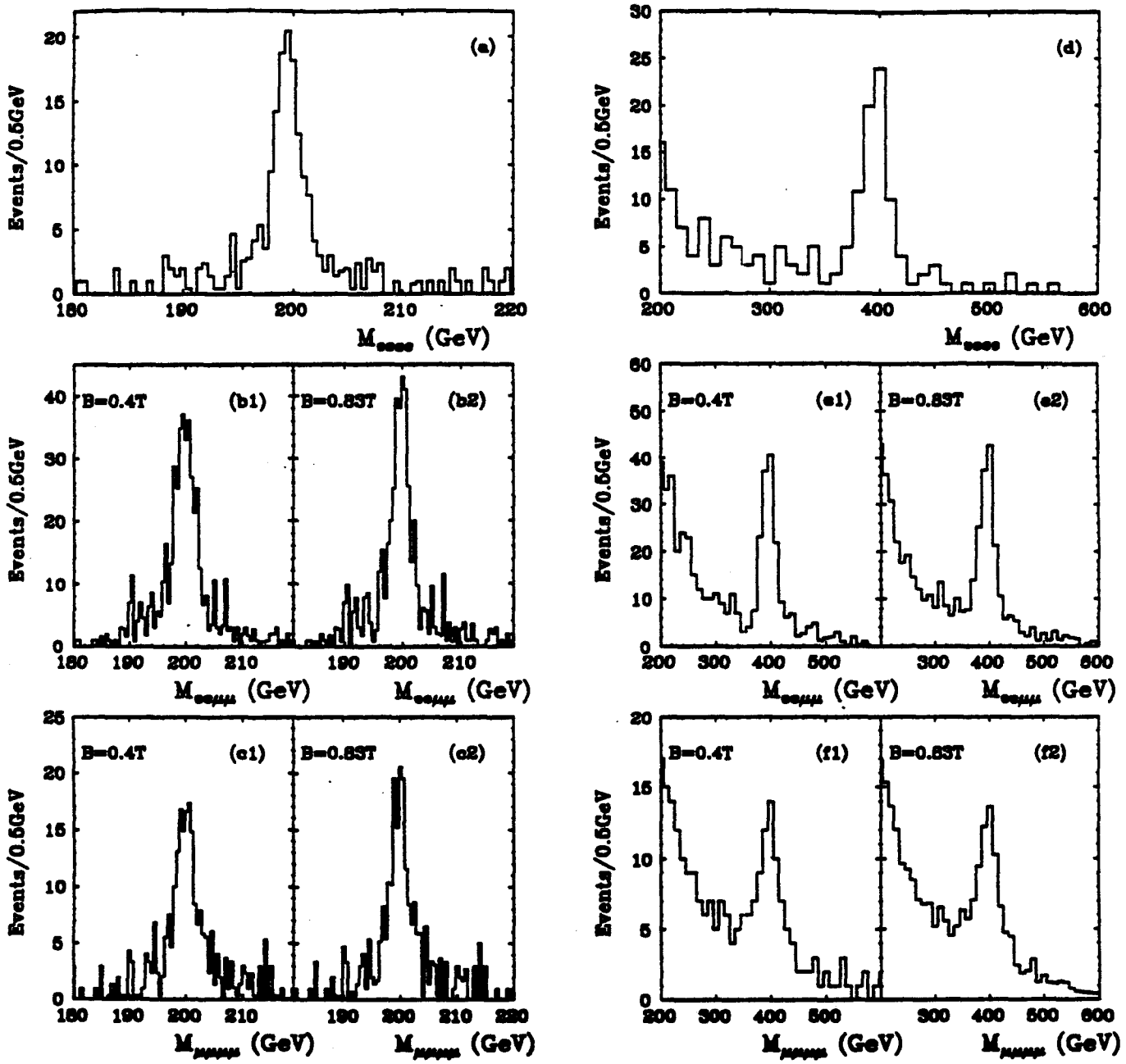

Figure X.3: $H^0 \rightarrow ZZ^* \rightarrow$ 4 leptons for (a-c) M_H = 200 GeV, and (d-f) M_H = 400 GeV. The mass spectra are shown for both magnet options (B=0.4 T and B=0.83 T).

B.2 $M_{H^0} = 200$ *GeV and* $M_{H^0} = 400$ *GeV*

We have investigated backgrounds from jets, heavy quark decays, and W and Z^0 boson production. We require all four leptons to have $p_T > 10$ GeV, to be isolated (R=0.3, E_c=5 GeV), and to be inside the angular range, $5° < \theta < 175°$ for muons, and $6.7° < \theta < 173.3°$ for electrons. Lepton pairs should have an invariant mass $M_{\ell\ell} = M_Z \pm 2$ *GeV* for M_{H^0} = 200 GeV and $M_{\ell\ell} = M_Z \pm 5$ *GeV* for M_{H^0} = 400 GeV.

The result of our study is shown in Figures X.3(a-c) and (d-f) for Higgs masses of 200 GeV and 400 GeV, respectively. The Higgs signal is clearly seen above the background. The mass resolution improves for the high B field option at 200 GeV. Due to the large natural width of the Higgs the spectra are very similar at 400 GeV.

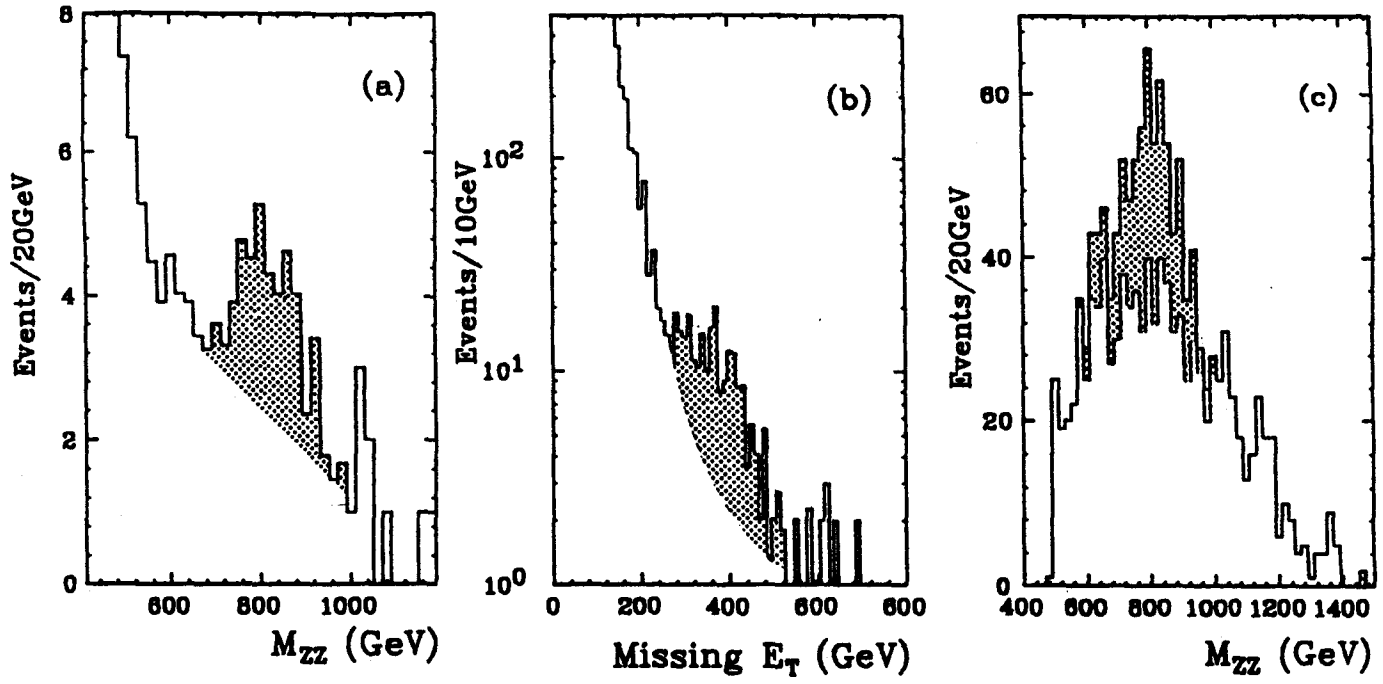

Figure X.4: Reconstructed Higgs mass (M_H=800 GeV) from (a) $H^0 \rightarrow Z^0Z^0 \rightarrow$ 4 leptons (μ,e); (b) missing E_T spectrum from $H^0 \rightarrow Z^0Z^0 \rightarrow \ell^+\ell^-\nu\bar{\nu}$ together with background. Figure (c) shows the $H^0 \rightarrow Z^0Z^0 \rightarrow \ell^+\ell^-$ + jet jet mass spectrum with background. The shading indicates the expected Higgs contribution.

B.3 M_{H0} = 800 GeV

We consider three decay modes to discover a Higgs boson with mass 800 GeV:

$H^0 \rightarrow Z^0Z^0 \rightarrow$ 4 charged leptons,

$H^0 \rightarrow Z^0Z^0 \rightarrow \ell^+\ell^- + \nu\bar{\nu}$, and

$H^0 \rightarrow Z^0Z^0 \rightarrow \ell^+\ell^-$ + jet jet.

The decay into 4 charged leptons (e or μ) provides the cleanest Higgs boson signal, but at large Higgs masses (800 GeV and higher) the expected number of events per SSC year is small. The neutrino decay mode cross section is ~ 6 times larger. This decay mode is characterized by large missing energy. The cross section of the third channel, into two charged leptons and two jets, is ~ 22 times larger than the 4 charged lepton channel. Searching for the Higgs boson in this channel requires a strong reduction of hadronic backgrounds.

$H^0 \rightarrow Z^0(\rightarrow \ell^+\ell^-) + Z^0(\rightarrow \ell^+\ell^-)$

We have used the same cuts as for the 400 GeV Higgs boson. The result is shown in Figure X.4a. Between 600 GeV and 1000 GeV we expect in one year 50 events from the H $\rightarrow$ 4 lepton decay, and about 30 events from the background $pp \rightarrow ZZ \rightarrow$ 4 lepton. This corresponds to a 6 standard deviation effect. The signal to background ratio is the same for both magnet options.

$H^0 \rightarrow Z^0(\rightarrow \ell^+\ell^-) + Z^0(\rightarrow \nu\bar{\nu})$

For the neutrino decay mode we consider backgrounds from production of Z^0Z^0,WW, Z^0+X, and heavy quarks (c,b,t). The characteristic of this decay channel is the large missing transverse energy (Figure X.4b). Details of this analysis and a complete list of selection criteria have been given earlier [2]. After all cuts we expect 180 Higgs events per SSC year, and 220 background events (70 from Z^0Z^0 and 150 from associated production of a Z^0 and a heavy quark). This corresponds to a 12 standard deviation effect for one year.

$H^0 \rightarrow Z^0(\rightarrow \ell^+\ell^-) + Z^0(\rightarrow$ jet jet)

This decay mode requires good energy resolution for hadronic jets in order to reconstruct Z^0 bosons and suppress the dominant backgrounds from Z^0 production with high p_T jets (see section X.D for details on the jet reconstruction and energy resolution). We have considered backgrounds from production of Z^0 Z^0,W W, Z^0+X, and heavy quarks (c,b,t). A detailed description of cuts has been given earlier [2]. Important requirements are that the reconstructed lepton and jet masses should agree with the Z^0 mass ($|M_{\ell\ell} - M_Z| \leq 5$ GeV and $|M_{jj} - M_Z| \leq 7$ GeV). In one year we expect about 210 Higgs events, 640 background events from Z^0 + X and 10 events from Z^0Z^0. No background is expected from WW and $t\bar{t}$ production. The Higgs signal corresponds to an 8 standard deviation effect.

C Search for the Top Quark

The L* detector's ability to measures leptons and jets precisely gives it excellent sensitivity for discovering the top quark in multilepton and multijet final states. By triggering on isolated leptons, L* will be able to discover the top quark with small background, and with small systematic uncertainty. The ability to clearly identify muons inside jets is crucial in this analysis.

The mass of the top quark can be determined by two independent methods: (1) from the di-lepton mass spectrum of the cascade decay of the top, and (2) from the mass reconstruction with hadronic jets. We have studied top quark decays into W^++b and H^++b. The H^+ is assumed to decay into $c\bar{s}$ or $\tau^+\nu$. The cross section for $t\bar{t}$ pair production, for a top quark mass of 250 GeV, is about 1 nb for $P_T^{top} > 100$ GeV, corresponding to approximately 10^7 events per SSC year. The large production rate allows us to select a clean sample of events, with a topology which is unique to heavy top quark decays. We have studied the following event topologies:

1) Events with one isolated e-μ pair and one inclusive muon.

$$
\begin{array}{l}
\qquad\qquad\qquad\qquad\qquad\qquad \longrightarrow \ell^- \bar{\nu} \\
\qquad\qquad\qquad\qquad\quad \longrightarrow W^- + \bar{b}\ (\rightarrow \mu^+ + \bar{c}) \\
(1)\ \ pp \rightarrow t\ \ \bar{t} + X \\
\qquad\qquad\quad \hookrightarrow W^+ + b\ (\rightarrow \text{jet}) \\
\qquad\qquad\qquad\ \hookrightarrow \ell^+ \nu
\end{array}
$$

where the two leptons from the W-decays are isolated, and the muon from the b-quark decay is inside a jet.

We require that both leptons in the pair are isolated (R=0.3, E_c=5 GeV) and have $p_T > 30$ GeV. The inclusive muon from the b-decay should have $p_T > 5$ GeV. Using the above cuts we expect 2.2×10^4 events per SSC year with a background of 1930 events (625 from W+X, 1200 from $b\bar{b}$ and 105 from Z+X). L* will be able to discover the top quark using this channel in less than one day of SSC running at design luminosity. The top quark mass can be determined from the shape of the invariant mass spectrum of the inclusive muon,μ^+, and one isolated lepton, ℓ^-. Figure X.5a shows the di-lepton spectra for top masses of 200 GeV, 250 GeV, and 300 GeV. An accuracy of $\approx$ 10 GeV in the top mass can be achieved with this technique.

2) Events with one isolated e or μ and two inclusive muons.

$$
\begin{array}{l}
\qquad\qquad\qquad\qquad\qquad\qquad\qquad\qquad \longrightarrow \mu^+ + \text{jet} \\
\qquad\qquad\qquad\qquad\quad \longrightarrow \ell^+ \qquad \longrightarrow \mu^- + c \\
\qquad\qquad\qquad\quad \longrightarrow W^+ \quad + \quad b \\
(2a)\ \ pp \rightarrow t\ \ \bar{t} + X \\
\qquad\qquad\quad \hookrightarrow W^- + (\bar{b} \rightarrow \text{jet}) \\
\qquad\qquad\qquad\ \hookrightarrow \text{jet jet}
\end{array}
$$

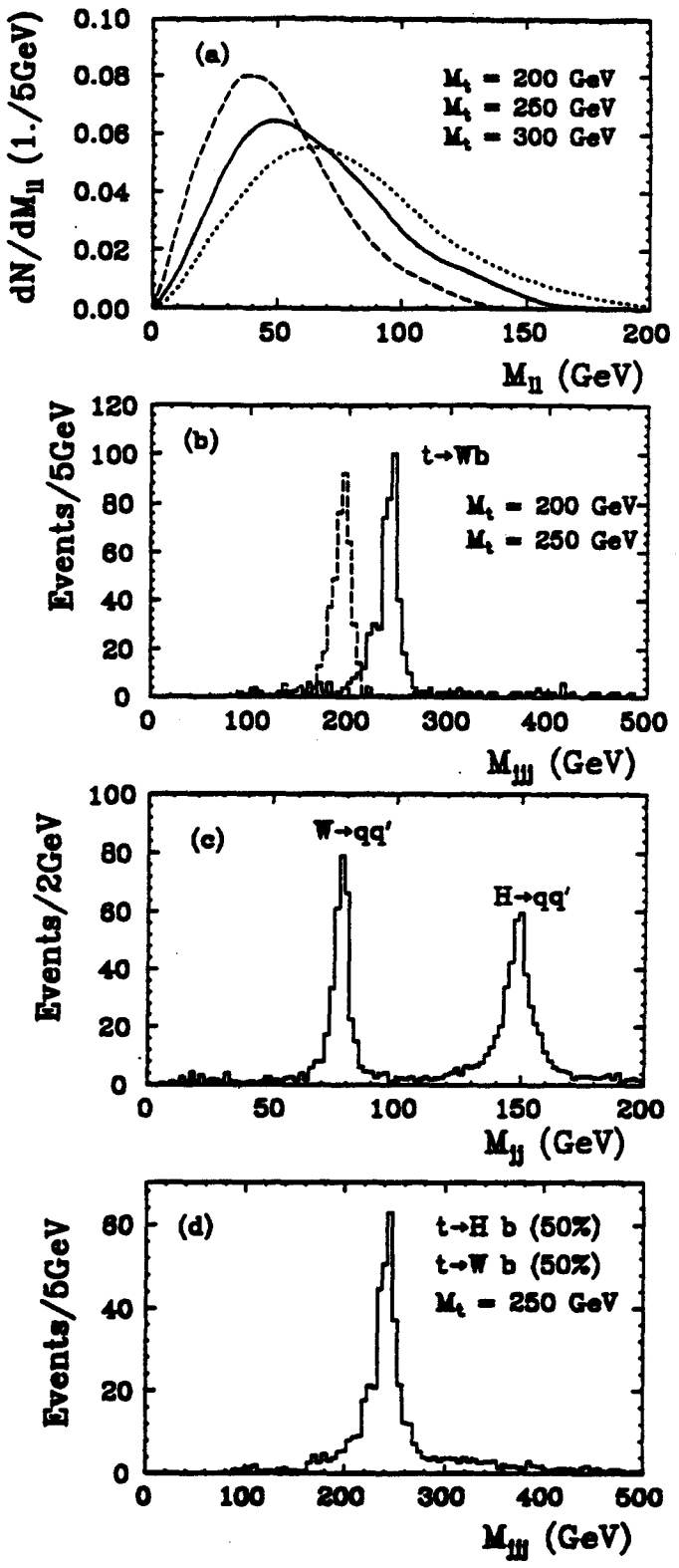

Figure X.5: Mass determination of the top quark from (a) lepton pair invariant mass (reaction 1). (b) reconstructed 3-jet mass spectrum for a 200 GeV and 250 GeV top quark (reaction 2a). (c) Reconstructed $W^\pm$ and $H^\pm$ mass spectrum (reaction 2b). The figure corresponds to equal branching ratios for the top decay into $W^\pm$ and $H^\pm$. The reconstructed top mass for these events is shown in figure (d).

where the lepton ℓ^+ from the W decay is isolated. Both muons from the cascade b decay are in the same jet. The signature of reaction (2a) is one isolated high p_T lepton with mean p_T of about 70 GeV, and at least 3 hadronic jets with mean p_T between 70 GeV (for the jets from W decay) and 100 GeV (for the b jet). Two of the jets have an invariant mass of the W. Many events in this channel have a very distinctive topology, in which the three leptons are in one hemisphere. We apply similar cuts as for reaction (1) and require that all three leptons be in one hemisphere and three jets be in the opposite hemisphere.

In one year we expect 8.2×10^3 events, compared to a background from W+X, Z+X and $b\bar{b}$ of 9 events. Thus running less than one day at design luminosity is sufficient to discover the top quark. Figure X.5b shows the reconstructed top mass from these three jets for 200 GeV and 250 GeV top quarks. The mass resolutions are ≈6%. L* can reconstruct the top mass with a resolution of ≈10 GeV, and with an expected error on the central value of ≈ 2%.

If there is a charged Higgs, $H^{\pm}$, with a mass of 150 GeV, the observable signal for a 250 GeV top quark in the L* detector includes the following reactions:

$$
\begin{array}{lll}
 & & \longrightarrow \mu^+ + \text{jet} \\
 & \longrightarrow \ell^+ & \longrightarrow \mu^- + c \\
 \longrightarrow W^+ & + & b \\
\text{(2b)}\quad pp \rightarrow t & \bar{t} + X & \\
 \hookrightarrow H^- + (\bar{b} \rightarrow \text{jet}) & & \\
 \hookrightarrow \text{jet jet} & &
\end{array}
$$

for $H^{\pm}$ decaying into a pair of quarks ($H^- \rightarrow \bar{c} + s$), and

$$
\begin{array}{lll}
 & & \longrightarrow \mu^+ + \text{jet} \\
 & \longrightarrow \ell^+ & \longrightarrow \mu^- + c \\
 \longrightarrow W^+ & + & b \\
\text{(2c)}\quad pp \rightarrow t & \bar{t} + X & \\
 \hookrightarrow H^- + (\bar{b} \rightarrow \text{jet}) & & \\
 \hookrightarrow \tau^- \nu & &
\end{array}
$$

for $H^{\pm}$ decaying into $\tau + \nu$.

Reaction (2b) yields a more precise determination of the Higgs mass than (2c). Therefore if the branching ratio of $H^{\pm} \rightarrow \tau\nu$ is not close to 100%, we can use (2b) to detect the Higgs and determine its mass. The signature of reaction (2b) is one isolated lepton with mean p_T of about 70 GeV, two inclusive muons and at least 3 hadronic jets with mean p_T between 70 and 100 GeV, where two of the jets have the invariant mass of the charged Higgs (150 GeV). Figure X.5c shows the reconstructed Higgs and W mass spectrum for Br(t→ H^++b) = Br(t→ W^++b) and Br($H^+ \rightarrow c\bar{s}$)=100%. The reconstructed 3-jet mass from hadronic decays of the $H^{\pm}$ or $W^{\pm}$ and the b-jet is shown in Figure X.5d. The top mass can be determined with a precision of ≈ 2%.

We have performed a study assuming various branching ratios for the top decay into charged Higgs and for the Higgs decay $H^+ \rightarrow c\bar{s}$ or $\tau^+ + \nu$. The conclusion is that L* will be able to find the charged Higgs in one SSC year for Br(t → H^++b) Br(H → $c\bar{s}$) > 0.5%. The mass of the top-quark and the charged Higgs can be measured with a precision of ≈ 2%.

We have also studied the case when Br($H^+ \rightarrow \tau^+\nu$) ≈ 100%. We have selected events with one isolated lepton, one inclusive muon and a τ jet. For the τ jet we require $p_T > 70$ GeV, $\theta > 20°$, more than 30 GeV deposited energy in the hadron calorimeter, and an acoplanarity angle $\Delta\phi > 100°$ with respect to the isolated lepton. The τ-jet should have less than 4 charged tracks inside a cone of R< 0.3 around the jet axis. We expect 4.6×10^3 events per year in this channel for Br(t→ H^++b)=50%. No background is found from pp→W+X. Out of 1.1×10^6 pp→ $b\bar{b}$ + X events no event satisfies the cuts. In this decay mode the top mass can be determined from the invariant di-lepton mass as described earlier. The charged Higgs mass is similarly determined from the invariant mass of the τ-jet and the b-jet.

In summary L* will be able to find a top quark with $M_t = 250$ GeV in one day with nominal SSC luminosity. The top quark mass can be measured from hadronic jets with a precision of 2% or from the di-lepton spectrum with ≈ 5%. The charged Higgs boson can be detected in $c\bar{s}$ and $\tau\bar{\nu}$ decays, independent of the branching ratios.

D Jet Energy Resolution

In the search for the Higgs boson, the top quark and the charged Higgs we have utilized the good jet resolution of the L* detector. We reconstruct jets in the detector by starting with the calorimeter segment which has the largest energy deposit. Then neighboring cells (in pseudorapidity η and ϕ) are added to form a jet. A calorimeter cell is the seed for a new jet if the closest distance to a jet exceeds ΔR=0.6. In this analysis we consider only jets in the central region ($10° < \theta < 170°$). This reduces background contributions from initial state hard gluon radiation and from beam jets.

D.1 $Z^0 \rightarrow$ jet + jet

As an example for the reconstruction of Z^0s from jets we use the Higgs production (M_H = 800 GeV) with $H^0 \rightarrow Z^0Z^0 \rightarrow \ell^+\ell^-$ + jet jet decay. The jet resolution is crucial in this process as discussed in section X.B. Figure X.6a shows the jet-jet invariant mass from the Z^0 decay with background. We obtain a Z^0 mass resolution of 6%.

D.2 $Z' \rightarrow$ jet + jet

Similarly we have analyzed the process p + p → Z' → jet + jet ($M_{Z'}$=1 TeV). The natural width of the Z' is

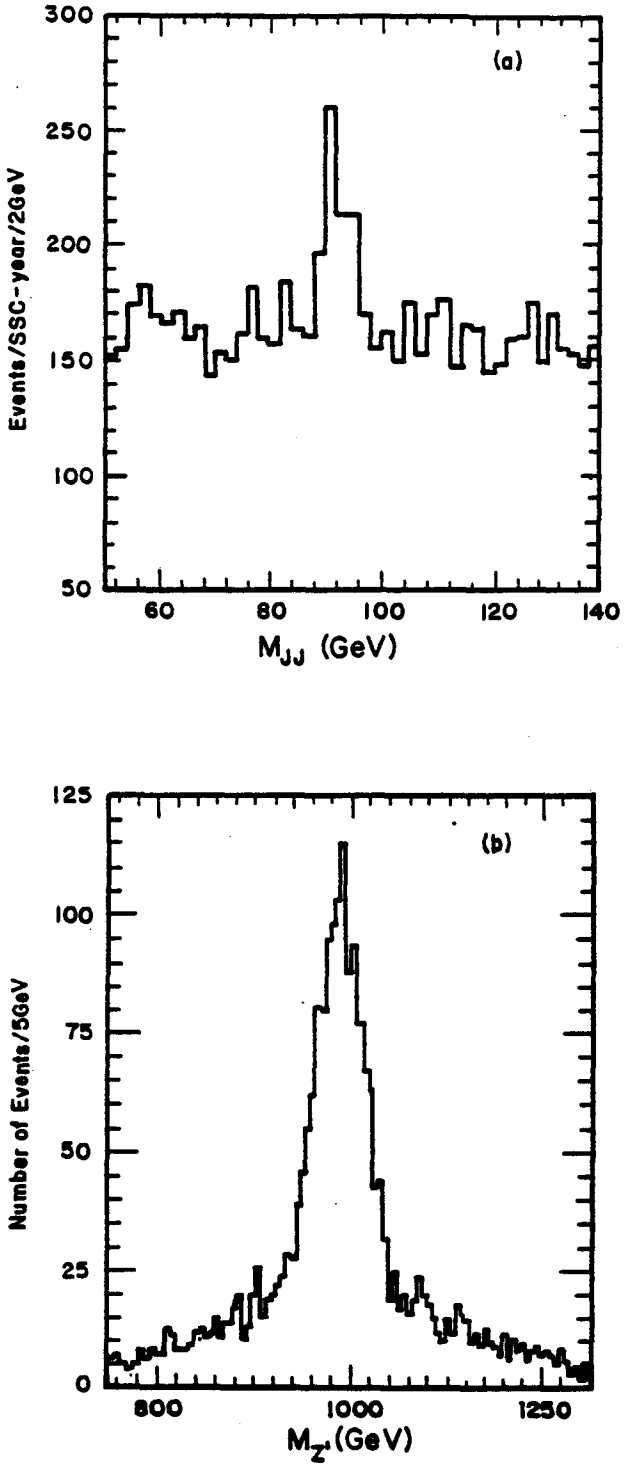

Figure X.6: (a) Mass spectrum of $Z^0 \rightarrow$ jet + jet from a 800 GeV Higgs decay and background. (b) Mass spectrum of $Z' \rightarrow$ jet + jet.

assumed to be 10 GeV. Only jets with $p_T > 300$ *GeV* have been used for this analysis. Figure X.6b shows the reconstructed jet-jet invariant mass. The FWHM/2.3 of this distribution is 30 GeV, corresponding to a mass resolution of 3%.

E Z' Reconstruction

We have generated $p + p \rightarrow Z' \rightarrow e^+e^-, \mu^+\mu^-$, and $\tau^+\tau^-$ events with $M_{Z'}$=4 TeV. We have assumed a $\Gamma_{Z'} = 10$ *GeV* and a branching ratio $Br(Z' \longrightarrow \mu^+\mu^-)$ = 3.0%. For electron pairs the invariant Z' mass can be reconstructed close to the natural width of the Z'. We require that the e^+ and e^- are inside the angular range ($6.7° < \theta < 173.3°$). Figure X.7a shows the e^+e^- mass spectrum for 1000 $Z' \rightarrow e^+e^-$ decays. We obtain a mass resolution of 0.5%. Even at these high energies shower leakage contributes less then 0.1% to the electron energy resolution. The acceptance of the electromagnetic calorimeter for this process is 93.6%.

For the decay into muons we have perform a detailed simulation of the detector response taking into account gaps in the muon chamber coverage, measurement uncertainties and muon energy loss in the calorimeter. Large energy loss from bremsstrahlung,pair production and photonuclear interactions is recovered by adding the calorimeter energy to the reconstructed muon momentum. The hadron calorimeter resolution for electromagnetic showers is $30\%/\sqrt{E}$ for the fine sampling part and $46\%/\sqrt{E}$ for the coarse sampling. On average a muon from the decay of a 4 TeV Z' deposits 50 GeV in the calorimeter.

We require that both muons are measured in the precision muon detector, and that both tracks be isolated (R=0.3, E_c=5 GeV), we obtain an acceptance of 82.2%. We can increase the acceptance for this process by selecting events where one muon is well measured in the muon detector and the second in the central tracker with a corresponding track in the hadron calorimeter and the RPC trigger counters. The transverse momentum measured in the tracker should exceed 200 GeV. We assume that the second muon has opposite charge and the same transverse momentum as the first well measured muon. Then the acceptance for $Z' \rightarrow \mu^+\mu^-$ is 97.8%. The $\mu\mu$ invariant mass distribution is shown in Figure X.7b. The mass resolution is 16% for the resistive coil and 9% for the superconducting coil option.

For the Z' decay into τ-pairs the substantial background from $t\bar{t}$ production has to be reduced. We require one isolated electron or muon (R=0.4, E_c=5 GeV) in the detector with $p_T(\ell) > 200$ GeV and $|\eta| < 2.5$. We require an additional jet or electron with $p_T(jet) >$ 200 GeV, $|\eta| < 2.5$, and less than 4 charged particles (with $p_T > 10$ GeV). The jet is required to be narrow, i.e. more than 90% of the jet energy should be inside a cone of R=0.3 around the jet axis. The sum of the transverse momenta, $p_T(\ell)+p_T$(jet), should exceed 800 GeV.

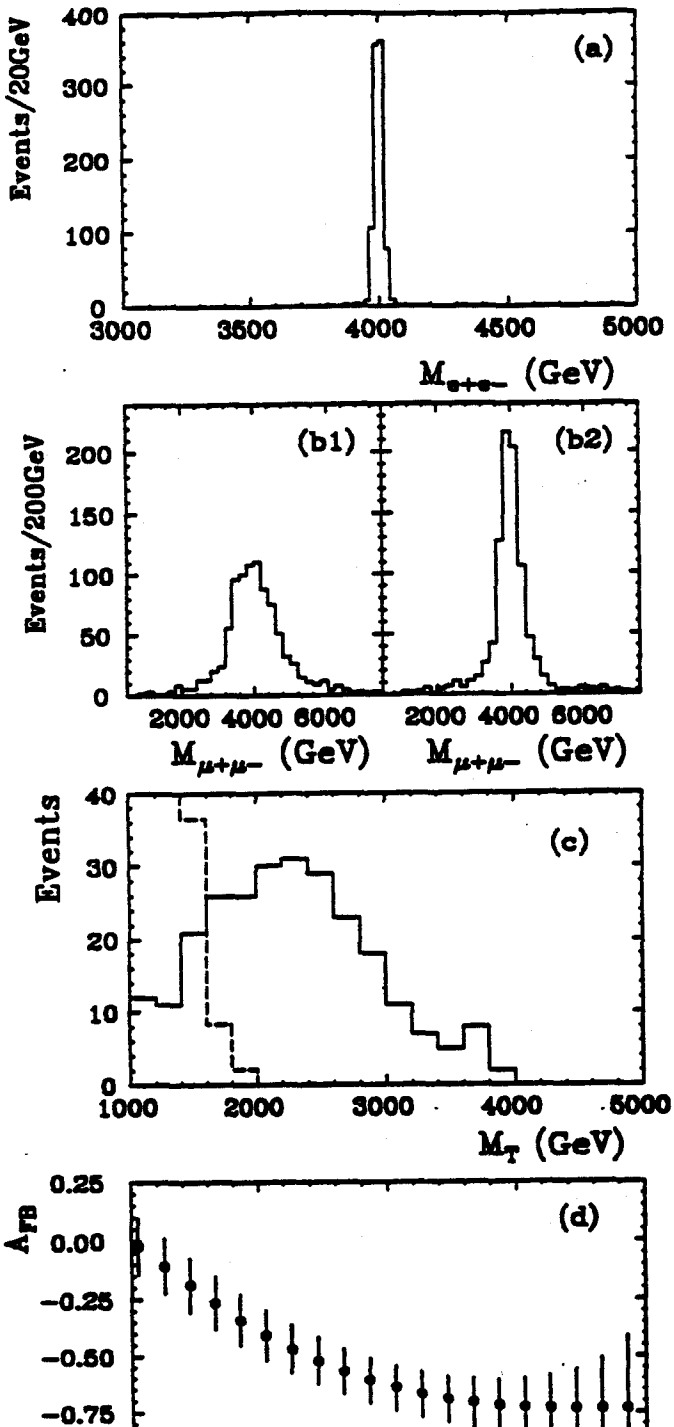

Figure X.7: (a) Z′ mass reconstruction with electrons and (b) muons. (b1) corresponds to the resistive coil and (b2) to the superconducting coil option. (c) Transverse mass spectrum from $Z' \rightarrow \tau^+\tau^-$ decays (solid line), and background from $pp \rightarrow t\bar{t} + X$ (dashed line). (d) Expected precision on the asymmetry from the $\mu^+\mu^-$ and $\tau^+\tau^-$ channel as function of $y_{Z'}$ for $\theta = 128°$.

Figure X.7c displays the transverse mass, M_T, as determined from the isolated lepton and the jet. The Z′ production dominates at high transverse masses. For $M_T > 1.6$ TeV we expect 216 events from the Z' decay and 10 events from $t\bar{t}$.

The forward-backward asymmetry is defined as

$$A_{FB} = F\frac{\sigma(y_- > y_+) - \sigma(y_- < y_+)}{\sigma(y_- > y_+) + \sigma(y_- < y_+)}$$

where $y_\pm$ refers to the rapidity of the final state $\mu^\pm$, and F=1 for $y_+ + y_- > 0$, and F=−1 for $y_+ + y_- < 0$. In the asymmetry measurement we use only events with muons for a reliable charge determination. The charge confusion for muons from the Z' decay is less than 1%. For the tau channel we restrict the analysis to events with at least one muon. 13.2% of the τ events are selected after all cuts. They are used in the asymmetry measurement. For 1000 Z′ events each in the muon and tau channel, the asymmetry can be measured with $\Delta A_{FB} = 3.0\%$. Figure X.7d shows the expected asymmetry as function of the Z′ rapidity in an E_6 model[5] with $\theta = 128°$. The error bars indicate the precision, which can be reached in rapidity intervals $\Delta y = 0.1$. The asymmetry measurement as a function of rapidity is important to distinguish models on Z' production. These studies show that L* can discover the Z' in the e^+e^-, $\mu^+\mu^-$, and $\tau^+\tau^-$ decay mode. The e^+e^- decay mode allows a precise measurement of the mass, and the $\mu^+\mu^-$ and $\tau^+\tau^-$ mode provides a precise measurement of the asymmetry.

References

[1] L* Collaboration, *Expression of Interest to the Superconducting Super Collider Laboratory*, May 1990.

[2] L* Collaboration, *Response to the Program Advisory Committee of the Superconducting Super Collider Laboratory*, July 1990.

[3] H. Benson, T. Sjorstrand, "A Manual to the Lund Monte Carlo for Hadronic Processes", PYTHIA version 5.4, June 1990.

[4] F. Paige, S.D. Protopopescu, "ISAJET 6.32, A Monte Carlo Event Generator for p-p and p̄-p Reactions", 1990.

[5] J.L. Rosner, Phys. Rev. D35, 2244 (1987)

Level 2 Cost of the L* Detector

	"1990" US Cost (k$)	US Cont. (%)	Cost US Cont. (k$)	Total Cost US (k$)	Switzerl. (kSF)	Germany (kDM)	USSR (k$)	Ba.+WL (k$)	Total Cost L* (k$)
A. MAGNET (RESISTIVE COIL)	37791.2	19.5	7369.8	45161.0			40348.4	4237.6	89747.0
B. MUON DETECTOR	80073.5	18.1	14462.1	94535.6	74778.1			15233.4	166419.1
C. HADRON CALORIMETER	33989.0	22.1	7528.3	41517.3			18061.1		59578.5
D. E.M. CALORIMETER	15820.6	15.5	2448.9	18269.6		54572.4		17780.1	71257.7
E. CENTRAL TRACKER	40120.3	31.0	12428.3	52548.6					52548.6
F. FORWARD CALORIMETER SYSTEM	10033.2	15.8	1583.0	11616.2		16970.2		5123.1	27687.8
G. COMPUTER								10000.0	10000.0
TOTAL L* DETECTOR	217827.8	21.0	45820.5	263648.3	74778.1	71542.7	58409.5	52374.2	477238.7

Table XI.1

XI Cost and Funding

As seen from the previous chapters and following the instructions of the Program Advisory Committee and the SSCL Director, we have been able to:

1. Maintain the original (EoI) physics objectives of L* at somewhat reduced muon resolution,
2. Reduce the size and weight of L* by more than a factor of two, and
3. Reduce the cost of each subdetector item by R&D efforts since the EoI.

In addition. we have broadened the participation of foreign countries to include more institutions from Western Europe and the Asia Pacific region.

The combined effort of reduced scope and more countries from Western Europe and the Asia Pacific region has enabled us to reduce the total foreign contribution to less than half of the total estimated cost. The fact that the total funding request from foreign participants is more than the projected need from foreign participants implies that L* will have adequate funding even if less than 2/3 of the funds requested of different governments are awarded.

In this chapter we present a detailed analysis of cost and funding of the basic design (with four options: resistive coil magnet with BaF_2 calorimeter, superconducting coil with BaF_2, resistive coil with LXe, superconducting coil with LXe.)

In the EoI, the procedure to calculate the detector cost was outlined. Since no distribution of responsibilities was assigned at that time, a possible U.S. contribution of 300M$ according to the U.S. accounting method was projected, and a possible distribution of responsibilities was discussed. Since the EoI, an extensive cost estimate has been undertaken on the LoI design. The level of detail at which the estimate was made varies by subsystem, in many cases it was finer than level 5 but never coarser than level 4 (L* assumed to be level 1). All estimates have been tabulated at level 4 for reporting purposes. The level 4 cost book has been submitted to SSCL. Table XI.1 summarizes a level 2 detector cost (the resistive coil, BaF_2 option).

The cost estimate for the detector is based on: (a) the experience of the L3 detector at CERN; (b) the experience of engineers and physicists from national laboratories (Oak Ridge National Laboratory, Lawrence Livermore National Laboratory, Los Alamos National Laboratory, and Kurchatov Atomic Energy Institute Moscow) as well as institute leaders of ETH Zurich and RWTH Aachen who have experience with other large construction projects.

A Preliminary Agreement of Responsibilities

Table XI.2 is a preliminary agreement on the sharing of responsibilities. Since the submission of EoI, a detailed study on funding possibilities on a broad international base has been undertaken which now allows us to propose a preliminary distribution of responsibilities.

Table XI.2: Sharing of Responsibilities*

Detector Subsystems	Government or Funding Agencies
Magnets	US, INFN Bologna (Italy) & World Laboratory **, USSR
Muon Detector	US, Bulgaria, China, INFN Bologna (Italy) & World Laboratory. Italy, Romania, Switzerland
Hadron Calorimeter	US, Italy, India, USSR
Electromagnetic Calorimeters	US, Germany, INFN Bologna (Italy) & World Laboratory, Italy, Japan, Korea, USSR
Central Tracker	US, Taiwan
Forward Calorimeter System	US, Germany, INFN Bologna (Italy) & World Laboratory
Computer	INFN Bologna (Italy) & World Laboratory

* As reported to the PAC on 7 July 1990, in generic question No. 7, in order to avoid a major collaborator from not fulfilling its planned obligation, our experience has been not to assign detailed responsibility until extensive R&D has been made on all the options.
** INFN Bologna (Italy) & World Laboratory is proposing to produce the magnets as an in kind contribution.

B Detector Cost

To determine the detector cost, we have used the following procedures:

- For the US portion, we follow the US accounting practice including EDIA and contingency. Labor rates are split into payroll (included in every level 3 item) and institutional support (added to the level 3 items).
- Asia Pacific, Europe, and USSR contributions are treated as in kind portions in manpower, materials, detector systems and detector parts including assembly at SSCL. Contingency and institutional support are not included. Manpower estimates from the different institutions are included only if existing personnel from the institutions do not meet the requirements of a given project. In such a case only the additional manpower costs are included in the table. Infrastructure costs are also not considered.

Table XI.3: Funding Requests from Foreign Participants

Funding Requests from Foreign Participants M$							
Germany	INFN Bologna* (Italy) & World Laboratory	India	Korea	Italy	Switzerland	USSR	Total Foreign Requests
65	60	8	20	12	77	90	332

Cost for Foreign Participants M$							
Magnets	Muon Detector	Hadron Calorimeter	Electro-magnetic Calorimeters	Central Tracker	Forward Calorimeter System	Computer	Total Cost
44.5	71.9	18.1	53.0	0	16.0	10.0	213.5

* INFN Bologna (Italy) & World Laboratory is proposing to produce the magnets as an additional in kind contribution.

Table XI.1 summarizes at level 2 the detector cost in thousands of US dollars and lists the US, Switzerland, Germany, USSR, and INFN Bologna (Italy) and World Laboratory (Ba + WL) as representative funding partners. (The exchange rates applied are as follows: \$1 = 1.32 SF and \$1 = 1.55 DM.) Table XI.1 includes the resistive coil magnet, muon detector, a liquid scintillator hadron calorimeter, a BaF_2 electromagnetic calorimeter, the central tracker, the forward calorimeter, and the on-line computer. The cost of the trigger is included in every detector subsystem. At the end of this chapter, tables summarizing the total costs of the different options at level 2 are included. The total costs vary from 492M\$ to 477M\$.

The costs are presented according to the responsibilities of the US institutions and the in kind responsibilities from foreign participants.

A level 3 cost breakdown in thousands of US dollars is included in Appendix A. The foreign portion is presented according to the preliminarily agreed upon responsibilities.

C Funding Requests

According to the preliminarily agreed upon responsibilities, Table XI.3 summarizes the funding requests which the different foreign participants are negotiating with their governments and/or funding agencies. The requests are presented in millions of \$US after conversion at present exchange rates.

In the last row of Table XI.3 these foreign requests are compared with the costs given in Table XI.1 for foreign participants for all the detector subsystems. As seen, the total request exceeds the cost. This situation reflects the strong interest for the experiment from foreign participants. The Taiwan and China requests are under discussion and, therefore, are not included. As seen from Table XI.3, L* will have adequate funding even if less than 2/3 of the funding requests to the different governments are accepted.

D Detector Cost without International Participation

For comparison, we estimated the cost of the detector without international participation. For the whole detector we follow US accounting procedures defined above. Table XI.4 summarizes at level 2 the detector cost in thousands of US dollars, assuming a resistive coil magnet, muon detector, a liquid scintillator hadron calorimeter, a BaF_2 electromagnetic calorimeter, the central tracker, the forward calorimeter and the on-line computer.

A level 3 cost breakdown in thousands of US\$ is included in Appendix A. As stated earlier, a level 4 cost breakdown has already been submitted to SSCL. A detailed comparison of level 3 detector cost, both with and without international participation, can be made from the attached tables.

Table XI.4: Detector Cost without International Participation

	"1990 Cost" (k$)	Contingency (%)	Contingency (k$)	Total Cost (k$)
A. Magnet (Resistive Coil)	132190.6	18.0	23782.9	155973.5
B. Muon Detector	158437.0	18.4	29154.7	187591.7
C. Hadron Calorimeter	65300.0	22.9	14964.5	80264.6
D. EM Calorimeter (BaF_2)	72256.2	12.6	7108.6	79364.8
E. Central Tracker	40120.3	31.0	12428.3	52548.6
F. Forward Calorimeter System	28693.1	18.4	5269.2	33962.3
G. Computer	10000.0	30.0	3000.0	13000.0
Total L* Detector	506997.2	18.9	95708.3	602705.5

E Experimental Program Facilities

We have submitted to the Physics Research Division of SSCL an update of the resource requirements needed for the L* detector. The cost of the Experimental Program Facilities, estimated by the SSCL, is shown in Table XI.5.

We have subtracted 5.2M$ of power supplies and cooling water systems which have been costed as part of the detector magnet system. An additional 1–2M$ of cost savings in surface facilities have been identified that will further reduce the SSCL estimate.

The cost of the foundation and structural supports for the detector and F/B magnets have not been included in the detector estimate. The cost of these structures when taken alone is approximately 3.7M$. We believe that this cost can be substantially reduced if the structures are integrated into the experimental hall foundation structures.

We intend to work with the SSCL to modify our requirements and/or design concepts to match the available budget.

F Level 2 Breakdown

We list in Tables XI.6 and XI.7 the level 2 breakdown for the four baseline options.

Table XI.5: Resource Requirements

WBS	Description	Subtotal M$	Cont. %	Cont. M$	Total M$
1	Underground Facilities	26.9	41.3	11.1	38.0
2	Surface Facilities	17.0	18.7	3.2	20.2
3	Power Systems	4.5	25.7	1.2	5.7
4	HVAC Systems	2.8	26.1	0.7	3.5
5	Cooling Load	2.2	27.4	0.6	2.8
6	IR Site Infrastructure	3.5	20.0	0.7	4.2
Subtotal	SSC Experimental Program Facilities	56.9	30.7	17.5	74.4
	Cost included in detector magnet system				(5.2)
Total					69.2

Table XI.6: Cost Estimates for the resistive coil, BaF_2 and for the superconducting coil, BaF_2 options

	"1990"	US	Cost	Total Cost					Total Cost
	US Cost	Cont.	US Cont.	US	Switzerl.	Germany	USSR	Ba.+WL	L*
	(k$)	(%)	(k$)	(k$)	(kSF)	(kDM)	(k$)	(k$)	(k$)
L* Cost Estimate: Resistive Coil [BaF2 Calorimeter Option]									
A. MAGNET (RESISTIVE COIL)	37791.2	19.5	7369.8	45161.0			40348.4	4237.6	89747.0
B. MUON DETECTOR	80073.5	18.1	14462.1	94535.6	74778.1			15233.4	166419.1
C. HADRON CALORIMETER	33989.0	22.1	7528.3	41517.3			18061.1		59578.5
D. E.M. CALORIMETER (BaF2)	15820.6	15.5	2448.9	18269.6		54572.4		17780.1	71257.7
E. CENTRAL TRACKER	40120.3	31.0	12428.3	52548.6					52548.6
F. FORWARD CALORIMETER SYSTEM	10033.2	15.8	1583.0	11616.2		16970.2		5123.1	27687.8
G. COMPUTER								10000.0	10000.0
TOTAL L* DETECTOR	217827.8	21.0	45820.5	263648.3	74778.1	71542.7	58409.5	52374.2	477238.7
L* Cost Estimate: S. C. Coil [BaF2 Calorimeter Option]									
A. MAGNET (S. C. COIL)	40975.0	24.0	9814.7	50789.7			43833.4	4169.1	98792.1
B. MUON DETECTOR	80073.5	18.1	14462.1	94535.6	74778.1			15233.4	166419.1
C. HADRON CALORIMETER	33989.0	22.1	7528.3	41517.3			18061.1		59578.5
D. E.M. CALORIMETER (BaF2)	15820.6	15.5	2448.9	18269.6		54572.4		17780.1	71257.7
E. CENTRAL TRACKER	40120.3	31.0	12428.3	52548.6					52548.6
F. FORWARD CALORIMETER SYSTEM	10033.2	15.8	1583.0	11616.2		16970.2		5123.1	27687.8
G. COMPUTER								10000.0	10000.0
TOTAL L* DETECTOR	221011.6	21.8	48265.4	269277.0	74778.1	71542.7	61894.6	52305.7	486283.8

Table XI.7: Cost Estimates for the resistive coil, LXe and for the superconducting coil, LXe options

	"1990"	US	Cost	Total Cost					Total Cost
	US Cost	Cont.	US Cont.	US	Switzerl.	Germany	USSR	Ba. + WL	L*
	(k$)	(%)	(k$)	(k$)	(kSF)	(kDM)	(k$)	(k$)	(k$)
L* Cost Estimate: Resistive Coil [LXe Calorimeter Option]									
A. MAGNET (RESISTIVE COIL)	37791.2	19.5	7369.8	45161.0			40348.4	4237.6	89747.0
B. MUON DETECTOR	80073.5	18.1	14462.1	94535.6	74778.1			15233.4	166419.1
C. HADRON CALORIMETER	33989.0	22.1	7528.3	41517.3			18061.1		59578.5
D. E.M. CALORIMETER (LIQUID XENON)	17644.5	20.2	3570.3	21214.8		54490.4		20320.0	76689.8
E. CENTRAL TRACKER	40120.3	31.0	12428.3	52548.6					52548.6
F. FORWARD CALORIMETER SYSTEM	10033.2	15.8	1583.0	11616.2		16970.2		5123.1	27687.8
G. COMPUTER								10000.0	10000.0
TOTAL L* DETECTOR	219651.7	21.4	46941.8	266593.5	74778.1	71460.6	58409.5	54914.1	482670.8
L* Cost Estimate: S. C. Coil [LXe Calorimeter Option]									
A. MAGNET (S. C. COIL)	40975.0	24.0	9814.7	50789.7			43833.4	4169.1	98792.1
B. MUON DETECTOR	80073.5	18.1	14462.1	94535.6	74778.1			15233.4	166419.1
C. HADRON CALORIMETER	33989.0	22.1	7528.3	41517.3			18061.1		59578.5
D. E.M. CALORIMETER (LIQUID XENON)	17644.5	20.2	3570.3	21214.8		54490.4		20320.0	76689.8
E. CENTRAL TRACKER	40120.3	31.0	12428.3	52548.6					52548.6
F. FORWARD CALORIMETER SYSTEM	10033.2	15.8	1583.0	11616.2		16970.2		5123.1	27687.8
G. COMPUTER								10000.0	10000.0
TOTAL L* DETECTOR	222835.4	22.2	49386.7	272222.2	74778.1	71460.6	61894.6	54845.6	491716.0

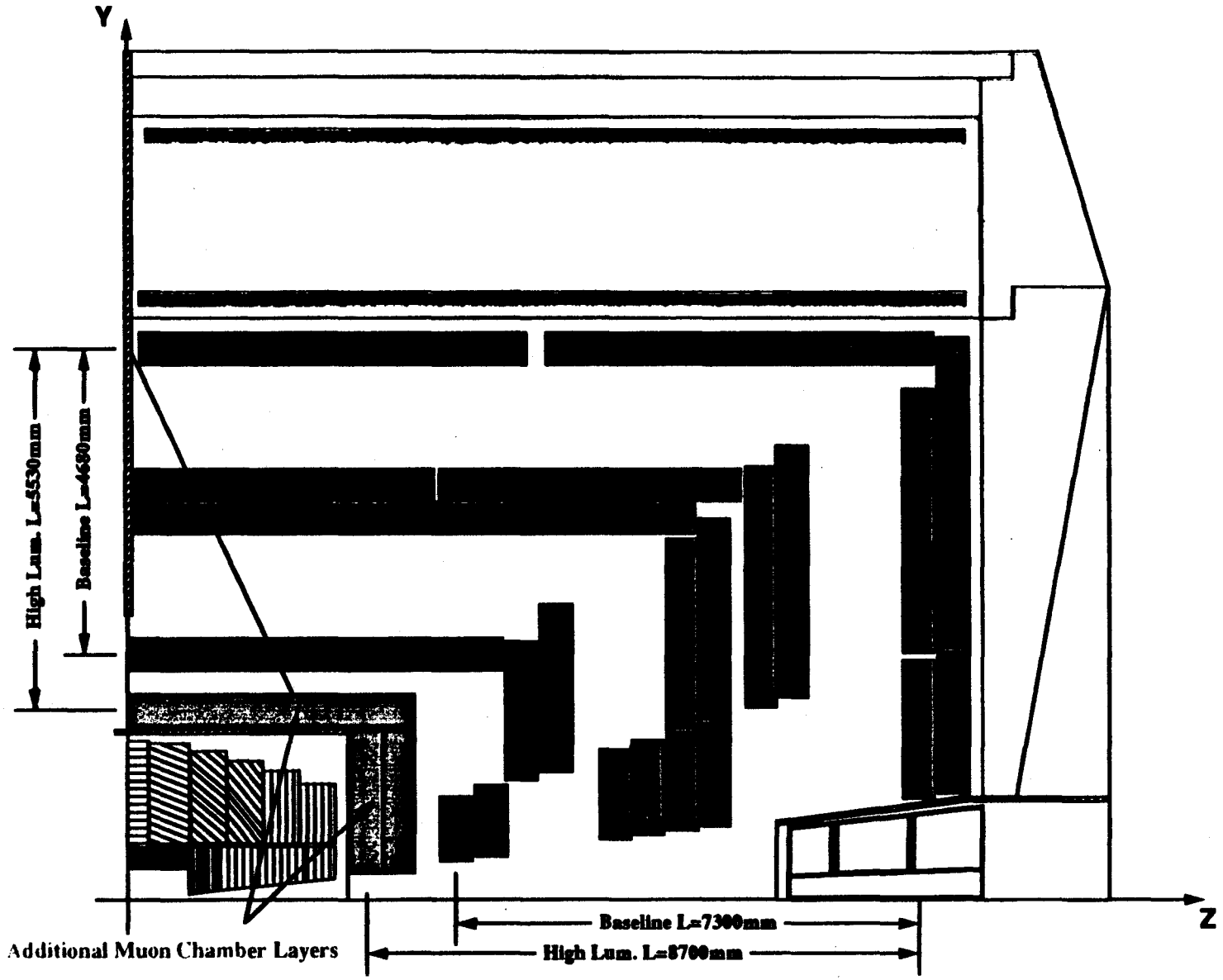

Figure XII.1 High Luminosity Version for the Double SC Coil Magnet: Side View

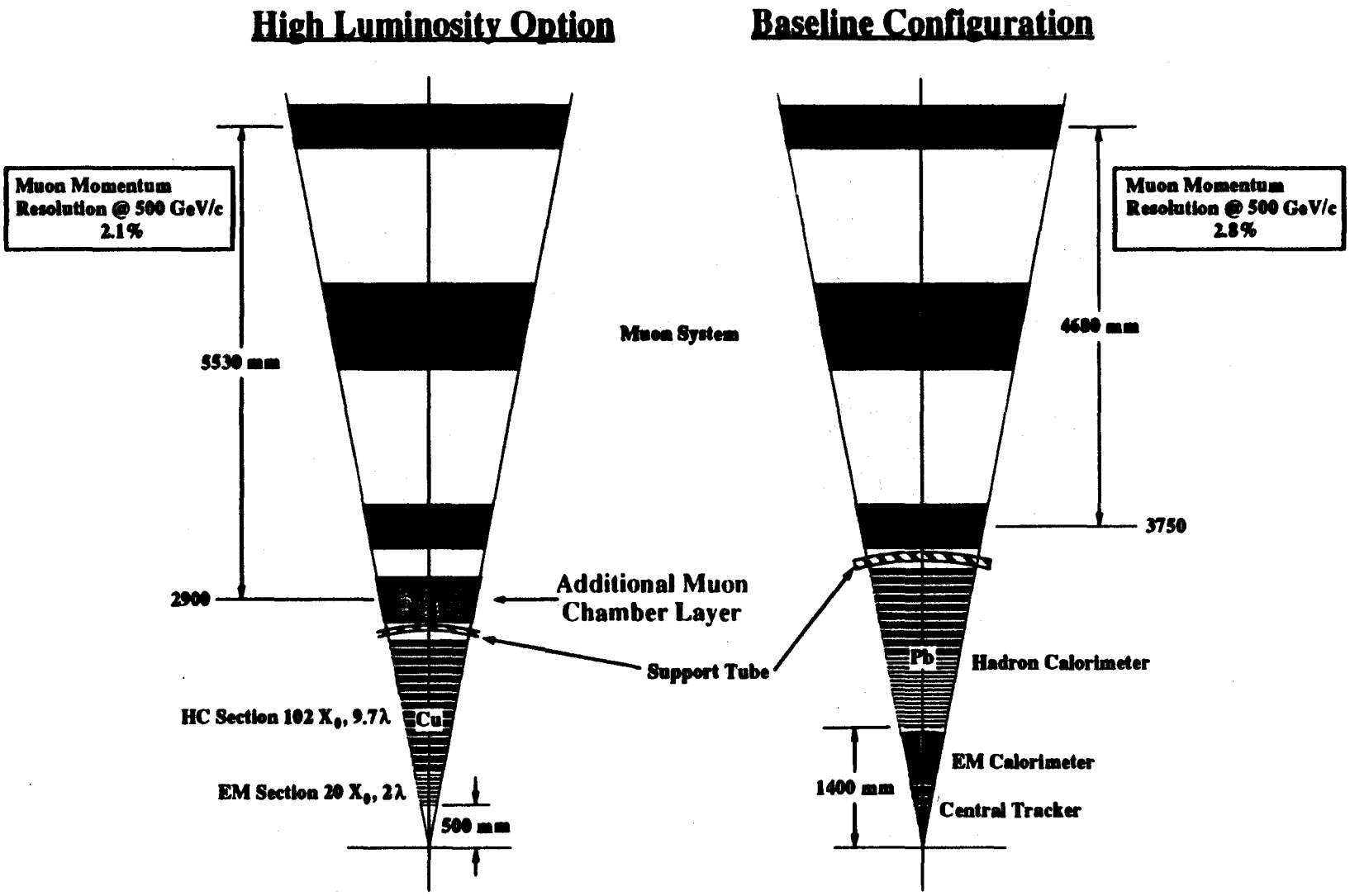

Figure XII.2 Schematic comparison of the High Luminosity Option with the baseline configuration: End View

XII OPTIONS

A Introduction

The L* magnet has a large volume filled with precision muon chambers. This permits us to rearrange the positions of the central tracker, the electromagnetic calorimeter and the hadron calorimeter to explore new physics. This flexibility is crucial when one considers the long construction time of L*. One of the unique features of the L* detector is its built-in capability to utilize various technical options which can be executed if experimental conditions and physics interest demand. We present here, as examples, four options based on both physics considerations and on our experience to cope with backgrounds. There are two kinds of backgrounds in any experiment:

1. Those from known physics origins which can be estimated with Monte Carlo programs.
2. Those from unknown origins: which, for example, may include muons traveling along the proton beam, or beam halo interactions with the beam pipe near the intersection point.

In general, the unknown background is much larger.

It is the ability to control the unknown background to a manageable level that will ultimately determine the quality of the experiment. This is particularly so in high intensity proton experiments, such as for $J \rightarrow e^+e^-$ and $\Upsilon \rightarrow \mu^+\mu^-$, where one needs both a high intensity beam and a very large rejection against hadron background. A similar situation exists at the SSC for detecting leptons. The success of the J and Υ experiments was due to both excellent resolution and repetitive momentum measurement of electrons and muons in the magnetic field; in the case of the electron, matching the momentum in the magnetic field with the pulse height in the shower counter is crucial.

In this chapter we present four examples. We begin by describing two options for a luminosity of 10^{34} cm^{-2}s^{-1} based on small changes of the baseline design presented in previous chapters. We follow this with an option requiring more extensive modifications (shown in Figures XII.1 and XII.2) for 2×10^{34} cm^{-2}s^{-1} and beyond. A fourth option, for inclusive lepton physics, is also described.

B Options

B.1 Option for $\sim 10^{34}$ cm^{-2}s^{-1}

If the Higgs is not found below a mass of 1 TeV, then high luminosity will be necessary to observe the symmetry breaking mechanism through measurements of longitudinally polarized gauge boson pairs, such as ZZ, ZW and WW. We present two of the simplest modifications of L* at 10^{34} $cm^{-2}s^{-1}$.

Enhanced Fiber Tracker

As indicated in Tables VII.4 and VII.5, scintillating fibers in the central tracker should be useful for more than several years at a luminosity of 10^{34} cm^{-2}s^{-1}, and the fiber occupancy would be less than 10%. The baseline design for operation at 10^{34} cm^{-2}s^{-1} therefore relies exclusively on the fiber tracker information. To augment its performance at minimal cost, an additional fiber super layer will be added at r = 44 cm (inside the inner straw module), as shown in Fig. XII.3. The estimated cost of this additional layer is $1.7M.

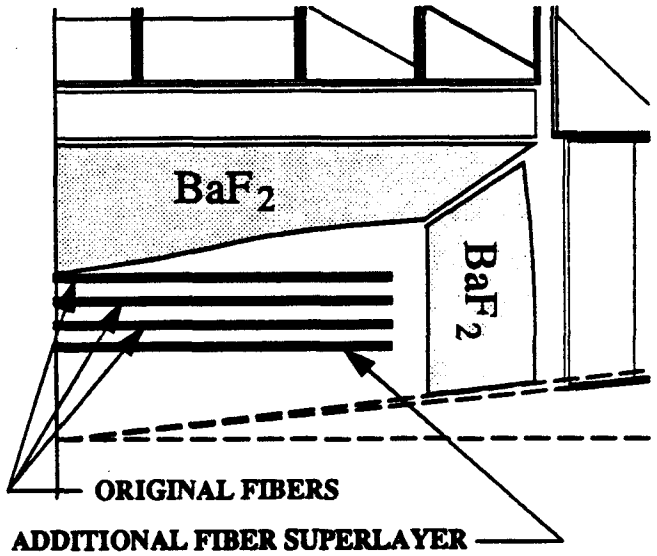

Figure XII.3: The side view of the enhanced fiber tracker.

We have investigated the pattern recognition capability by using only 4 super-layers of scintillating fibers. As an example, we have studied the mass reconstruction of a ZZ event with $P_T^Z > 200$ GeV which has a final state of 4 muons. The simulation includes 15 minimum bias events (MBE) overlapping with the ZZ signal. The average charged multiplicity for these events was found to be 300±100 for $\theta \in (16°, 164°)$ and $P_T > 200$ MeV. The track finding efficiency was found to be higher than 90%. The z position of an event vertex can be reconstructed to a precision of ~8.5 mm, as shown in Fig. XII.4.

The momentum resolution for the enhanced fiber tracker is shown in Fig. XII.5. The momentum information is very important in three respects:

- in providing correct track matching for muons and electrons by rejecting many low momentum charged tracks produced by overlaping MBE's;
- in reconstructing the correct event vertex by selecting charged tracks with momentum above a few GeV in the reconstruction process;
- in finding isolated muons and electrons by using the isolation cuts described in Chapter X.

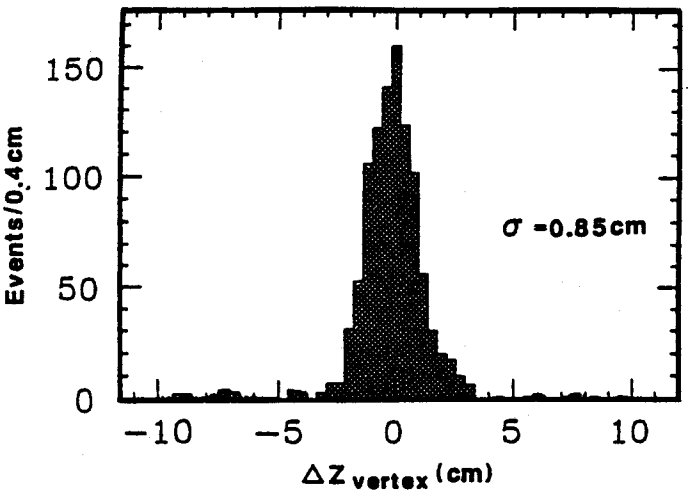

Figure XII.4: The distribution of the difference between the Monte Carlo generated z position and the reconstructed z position.

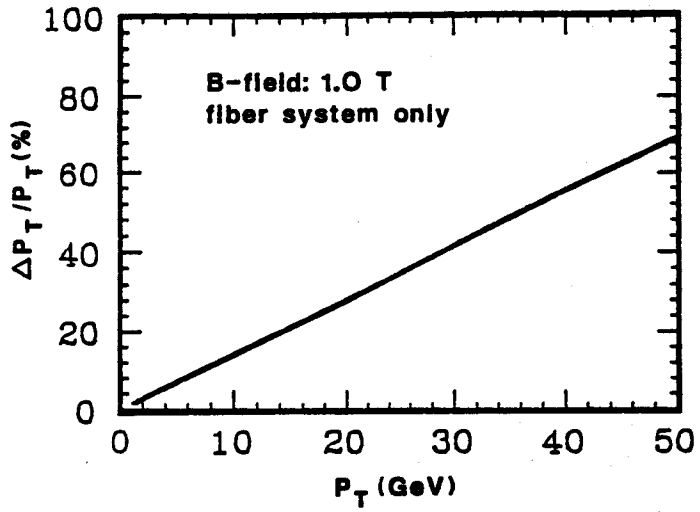

Figure XII.5: The momentum resolution ($\Delta P_T/P_T$) as a function of P_T for enhanced fiber tracker.

Modified Central Tracker

The LAA project has done much work on tracking at luminosities of 10^{34} $cm^{-2}s^{-1}$ and, with the participation of the INFN Bologna group, we are setting up an effort to explore the use of new central trackers at 10^{34} $cm^{-2}s^{-1}$ and beyond. Such tracking at 10^{34} $cm^{-2}s^{-1}$ may be achieved by using a finely segmented, radiation hard tracking device, such as the gas microstrip detector (GMD) [1], to replace the L* silicon tracker. Diamond or GaAs detectors may also become available during the next decade. However, prototypes of the GMD have already been built and their cost is much less than for the other devices. We therefore assume that the GMD's can be used for the modified central tracker. Figure XII.6 shows the side view of the modified central tracker consisting of GMD's and 4 super-layers of scintillating fibers.

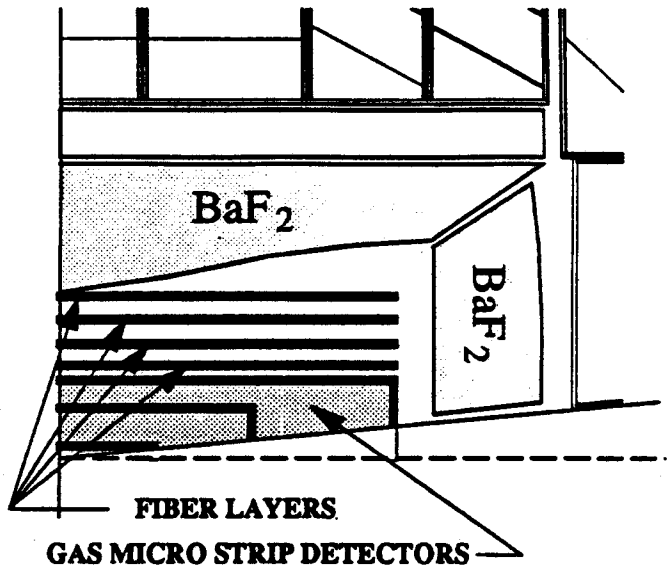

Figure XII.6: The side view of the modified central tracker.

The GMD is similar to a silicon strip detector in that microelectronics technology is used to produce high resolution (~1μm accuracy) electrode strips. Our design uses anode strip spacings of 200 μm, corresponding to r-ϕ resolution of 58 μm/plane. The strips would be deposited on radiation hard substrates having thicknesses of the order of 200 μm with a gas thickness of about 4 mm. The signals are very fast (30 ns) and rate capabilities are excellent (1 MHz/mm^2). Cell size is small so even at 10^{34} $cm^{-2}s^{-1}$, the occupancy is less than 1% per cell (individual cell rates are about 100 kHz). We are carrying out R&D to investigate chamber ageing. The estimated cost of replacing the L* silicon tracker with the GMD's is $18M.

The GMD strip geometry is similar to that for silicon so the electrode layout is nearly identical for the two configurations. The primary differences are the pitch, and the inner radius (10 cm for the GMD). The pattern recognition capability of this detector will be similar to the base-line design described in Chapter VII. The event vertex z resolution is expected to be ~2 mm. The momentum resolution of the modified central tracker is shown in Fig. XII.7.

B.2 Option for 2× 10^{34} $cm^{-2}s^{-1}$ and beyond

The detector is shown in Figures XII.1 and XII.2, with a new calorimeter configuration shown in Fig. XII.8.

Detector Design

The modifications of the basic design for the high luminosity are the following.

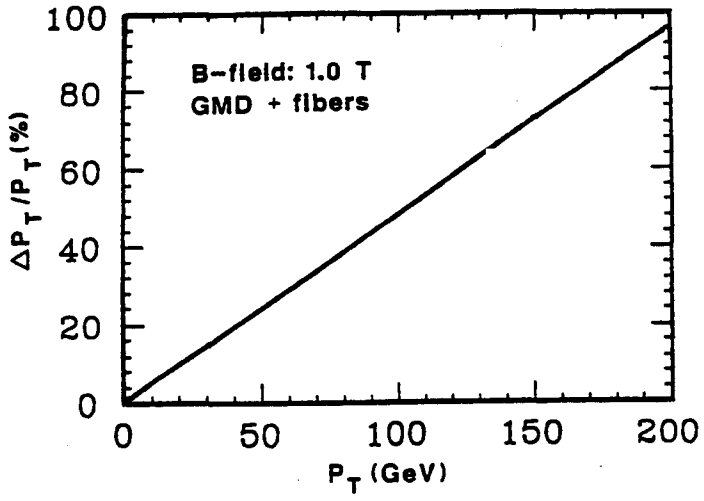

Figure XII.7: The momentum resolution ($\Delta P_T/P_T$) as a function of P_T for modified central tracker design.

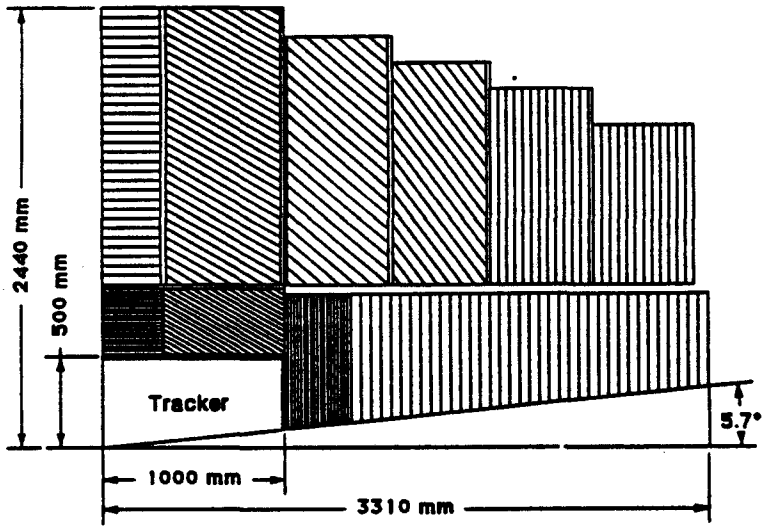

Figure XII.8: Longitudinal section of the calorimeter

- The central tracker and both electro-magnetic and hadron calorimeters as well as support tube are removed.
- A new layer of muon chambers is added. The lever arm of the muon chambers is thus increased as shown in Fig. XII.2.
- A calorimeter made of Cu and a scintillator sampling structure starts at an inner radius of 0.5m as shown in Fig. XII.8.Its electro-magnetic (front) section has 20 layers of a fine sampling structure: $1X_0$ Cu + 4mm of scintillator, and is followed by 29 layers of a coarser (5 cm Cu + 4 mm scintillation) hadronic section. The total thickness of the calorimeter is 11.7λ. Transversal segmentation of the basic design $\Delta\eta, \Delta\phi = 0.05$ is preserved. Readout is arranged to form towers pointing to the intersection region. The front window of the towers is 2.5x2.5 cm^2 above 15°and 1.5x1.5 cm^2 between 5.7°and 15°. Longitudinal segmentation will provide information for muon tracking.
- Inside the calorimeter coordinate measurement layers made of scintillating fibers are installed. The structure of each coordinate (super)layer is shown in Fig. XII.9. The fiber dimensions are chosen to limit the occupancy to an acceptable level of a few percent.
- A GMD central tracker is installed between the inside of the calorimeter and the beam pipe; the GMD design is the same as that described in section XII.B.1 with the exception that two tracking layers are added (bringing the total to 8) at radii of 46 and 48 cm.

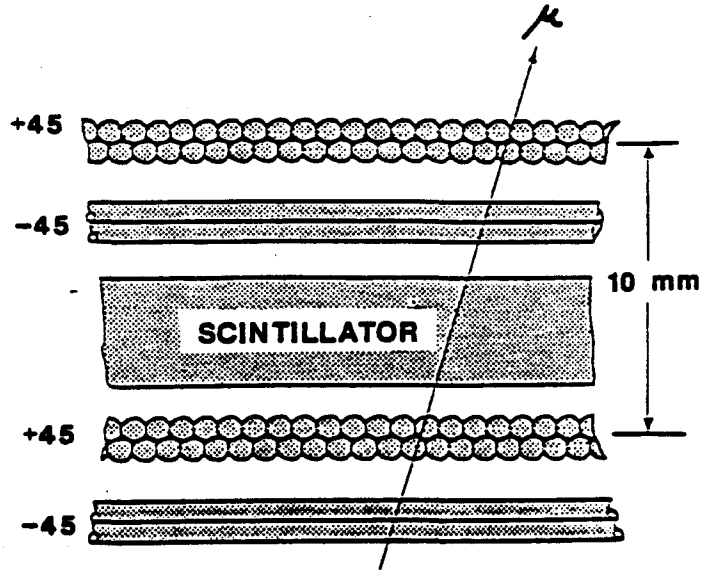

Figure XII.9: The structure of a superlayer of coordinate scintillating fibers

Detector Performance

The increased background of pileup events makes us concentrate on muon physics and on jet physics. Electron and photon studies are more affected by the background since pattern recognition becomes more difficult at high luminosity.

Since high levels of background may result in reduced effectiveness of the muon isolation criteria, one needs better muon momentum resolution to reduce the background. The muon momentum resolution is improved by increasing the lever arm and introducing a fourth layer of muon chambers. In addition an independent muon momentum measurement is performed within the modified calorimeter by introducing coordinate measurement layers.

At these high luminosities one relies on repetitive momentum measurements to reject background:

1. The four muon chamber layers add redundancy in that each combination of three chamber layers determines the momentum;
2. The momentum will be measured independently in the calorimeter;
3. The momentum will also be measured independently in the central tracker.

An important tool to reduce the pileup background, besides the multiple muon momentum measurement, will be the reconstruction of the muon vertex coordinate along the beam and discrimination of events with muons originating from different vertices. The accuracy of the event z position reconstruction will be ~2 mm.

Momentum Measurement with Muon Chambers

The installation of an additional muon chamber layer will improve the momentum resolution of the muons from 2.8% (at 500 GeV, 90°) to 2.1% (Fig. XII.2) for the superconducting magnet option, and will improve the muon momentum resolution from 4.9% to 3.0% for the resistive coil option.

Momentum Measurement with Central Tracker and Calorimeter

The independent measurement of muon momentum using GMD's and Calorimeter relies on the knowledge of transverse coordinates of the colliding beams and on the coordinates measured in the inner muon chamber. The expected accuracy of this measurement will be 40% at 100 GeV assuming scintillation fiber diameter in the superlayers (Fig. XII.9) is 1.0 mm, and systematic uncertainty because of fiber alignment is 0.5 mm.

The calorimeter energy resolution is affected by the overlap of MBE's coming from the same beam crossing. Because of the pile-up, the fluctuation of energy within a cone of $\Delta R = 0.4$ around a muon is ~20 GeV.

Physics Examples

We have studied the performance of the detector at a luminosity, $L = 2 \times 10^{34}$ cm^{-2}s^{-1}. Assuming a cross section for minimum bias events of about 100 mb, we expect an event pile-up of about 30 events for each beam crossing (for 60 MHz beam crossing rate). We have estimated by Monte Carlo [2] the energy inside a cone of R=0.4 around the muon direction for 30 pile-up events. The energy distribution has a long tail towards high energies. We find that for 98% of the muons the energy inside the cone is less than 100 GeV for $0 < |\eta| < 1$. The corresponding fractions are 96% and 82% for $1 < |\eta| < 2$, and $2 < |\eta| < 3$, respectively. These calculations give only approximate estimates, because of the large uncertainties introduced by the extrapolation from present $p\bar{p}$ colliders to the SSC. It is difficult to predict whether electron triggers will operate reliably, and whether the electron energy can be measured with high precision. This uncertainty does not apply for measurements with muons. The L* muon system is located outside the hadron absorber, thus the occupancy of the muon chambers is low. The reliability of the trigger and the precision of the momentum measurement is not affected by high luminosity.

Massive Higgs

If the Higgs boson has not been found at lower energies the experimental task will be to search for a heavy Higgs boson with a mass around 1 TeV and higher. The best channel is the $H^0 \longrightarrow Z^0Z^0$ decay, with subsequent decays into muons. The expected width of this particle is larger than 500 GeV. The signal is a broad Z^0Z^0 mass distribution on top of the $p+p \longrightarrow Z^0Z^0+X$ background. Therefore a precise measurement of the cross section $d\sigma/dM_{ZZ}$ is required to find evidence for the Higgs boson. The multiple and repetitive measurement of muons in the central tracker, in the hadron calorimeter and in the muon chambers will enable us to reduce unknown background to a minimum. As discussed in the EoI, p.88, the good muon momentum resolution enables us to identify $Z^0 \rightarrow \mu^+\mu^-$ clearly and to isolate the Z^0 peak with a resolution comparable with the natural width.

With the L* detector we can select Z^0Z^0 events with small background, as seen in figure XII.10. The

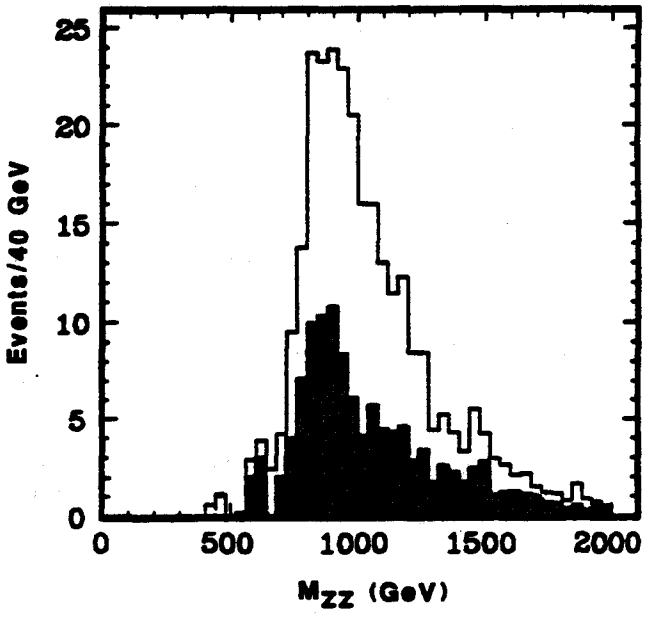

Figure XII.10: Z^0Z^0 mass distribution for two years of data taking at $L = 2 \times 10^{34}$ cm^{-2}s−1. The shaded area shows the background.

number of events corresponds to the four muon final state for two years data taking at $L = 2 \times 10^{34}$ cm^{-2}s^{-1}, assuming a top mass of 200 GeV.

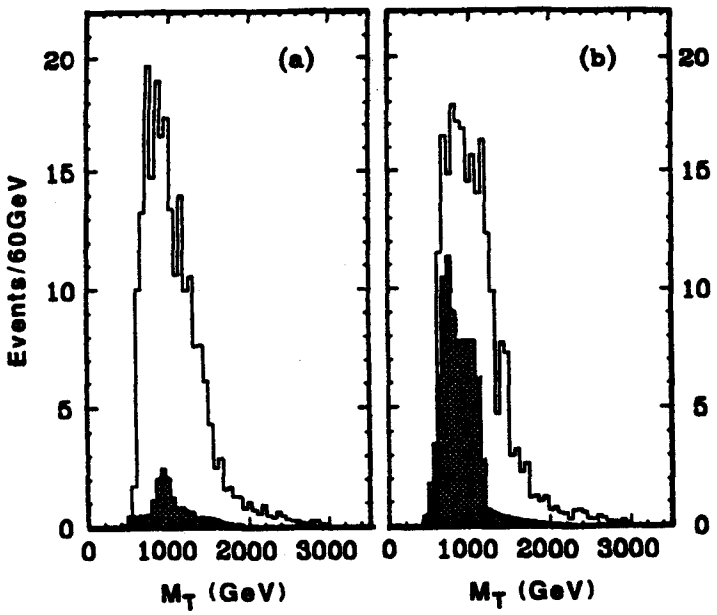

Figure XII.11: Reconstructed transverse mass $M_T(\mu^+\mu^- + \mu)$ for a) $\Delta p/p = 2.1\%$, and b) $\Delta p/p = 10\%$. The solid line indicates the WZ signal from Standard Model processes and from the decay of a techni-rho. The shaded area shows the background.

No isolation cuts have been applied for the muons. The solid line shows the contribution from the Higgs decay ($M_H = 1\ TeV$) and the $p + p \longrightarrow Z^0Z^0 + X$ contribution. The shaded area gives the expected events from $p + p \longrightarrow Z^0Z^0 + X$. In the Z^0Z^0 mass region between 800 GeV and 1.8 TeV we expect 148 events from the Higgs decay, 98 events from $p + p \longrightarrow Z^0Z^0$, and 3 events from $t\bar{t}$ and $Z^0 + X$. This corresponds to a Higgs signal of 14σ for two years of data taking. The background reduction has been achieved by requiring $|M_{\ell^+\ell^-} - M_Z| < 3\ GeV$. This corresponds to a cut at $\pm 2\sigma$ for the L* muon momentum resolution. A second important requirement is that the transverse momentum of one reconstructed Z^0 should exceed 400 GeV.

No Higgs

If no Higgs boson is found at the SSC a precise measurement of gauge boson pair production will be important to test the standard model at high energies or to find evidence for alternative models of symmetry breaking.

For example technicolor models, with dynamical symmetry breaking, predict a spectrum of high mass resonances. A discovery of such resonances provides strong evidence for technicolor. The predictions for these resonances are very model dependent. For example techni-rhos are expected to decay into WW, WZ^0 final states. The WW final state is difficult to observe because of the large background from $t\bar{t}$ production. The $W^{\pm}Z^0$ channel may be the most promising decay mode to discover the techni-rhos. A precise measurement of the $p+p \longrightarrow W^{\pm}\ Z^0 + X$ cross section is needed to separate the standard model and technicolor predictions. This requires a clean separation of the WZ final state from the background.

We have generated $W^{\pm}Z^0$ events with the PYTHIA program [2] for the production through $q\bar{q}$ annihilation. For the production through fusion we have used a technicolor model [3], with a techni-rho mass of $M_{T_\rho} = 1.5$ TeV. Backgrounds from $t\bar{t}$, $Zb\bar{b}$, and $Zt\bar{t}$ have been generated with PYTHIA 5.4. Every signal event has been overlayed with 30 minimum bias events. We have also included muons from hadronic showers or light quark decays, which penetrate the absorber and reach the muon detector. The punch through probability has been calculated from a GEANT simulation of the detector.

We apply the following selection criteria: Each muon should be isolated ($\Delta R = 0.4$, $E_{cone} < 100$ GeV), with $p_T > 20$ GeV, and $|\ \eta\ | < 3$. One Z^0 should be reconstructed from a muon pair with $|\ M_{\ell^+\ell^-} - M_Z\ | < 3$ GeV, and $p_T > 400$ GeV. The cut on the lepton pair mass corresponds to 2σ for the muon resolution of 2.1% at 500 GeV. The rapidity of the Z^0 bosons should be $|\ y\ | < 2.5$. We require a third muon (from the W decay) to have $p_T > 100$ GeV.

The result of the calculation is shown in Fig. XII.11 for two years of data taking (at $L = 2 \times 10^{34}\ cm^{-2}s^{-1}$). The solid line shows the WZ^0 signal from $q\bar{q}$ annihilation and techni-rho production. The shaded area gives the expected background.

Fig XII.11a corresponds to the L* detector with a momentum resolution of 2.1% at p_T=500 GeV. Fig XII.11b corresponds to a detector with a momentum resolution of $\Delta p/p = 10\%$ at p_T=500 GeV.

The distributions show the importance of momentum resolution and isolation cuts. With large pile-up we have used $E_{cone} < 100$ GeV (20 times larger than the normal cut of 5 GeV). With good resolution we can see the signal clearly.

B.3 Inclusive Lepton Option

Figure XII.12 shows a design operating at a luminosity of $10^{33}\ cm^{-2}s^{-1}$ where we have removed the electromagnetic detector and replaced it with a straw/fiber assembly. The long lever arm provides electrons and muons with a resolution of

$$\Delta P/P = 15\%\ at\ P = 0.5\ TeV.$$

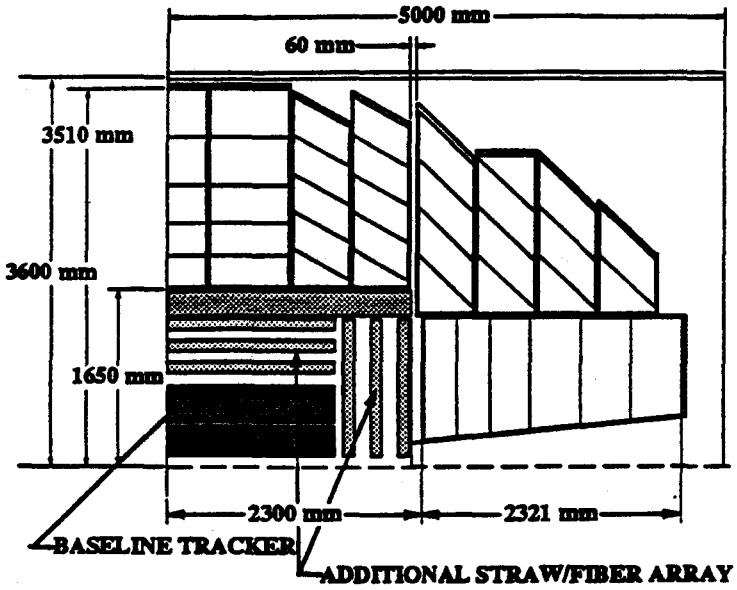

Figure XII.12: The side view of the large tracker option.

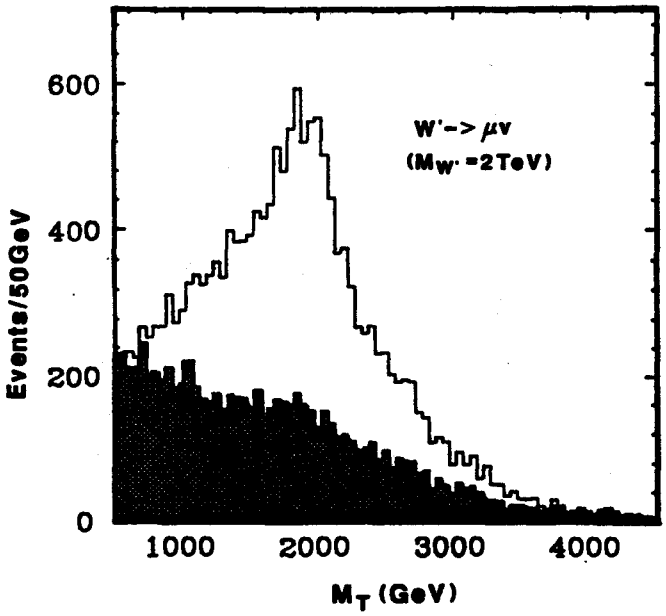

Figure XII.13: The transverse mass distribution of 2 TeV W′ particles reconstructed by using the large tracker option. The shaded area is the background from W+X and $t\bar{t}$. The solid line shows the sum of the signal and background.

This enables us to match very accurately the muon and electron momentum and thus reduce the unknown background. Figure XII.13 shows our study of examples of mass 2 TeV $W' \rightarrow \mu + \nu$.

The examples presented in this chapter are not the only possibilities, but serve as illustrations of the potential of L*.

References

[1] F. Angelini *et al.*, *Nucl. Inst. and Meth.* **A283** (1989) 755.
F. Angelini *et al.*, Particle World 1 (1990) 85.

[2] H. Benson, T. Sjorstrand, *A manual to the Lund Monte Carlo for Hadronic Processes*, PYTHIA version 5.4, June 1990.

[3] M.S. Chanowitz, M.K. Gaillard, *The TeV physics of strongly interacting W's and Z's*, Nucl. Phys. **B261** (1985) 379.

Appendix A Level 3 Cost Estimate

	"1990"	US	Cost	Total Cost					Total Cost
	US Cost	Cont.	US Cont.	US	Switzerl.	Germany	USSR	Ba. + WL	I.*
	(k$)	(%)	(k$)	(k$)	(kSF)	(kDM)	(k$)	(k$)	(k$)
SUMMARY: A. MAGNET SYSTEM (RESISTIVE COIL)									
A.1 ALUMINIUM COIL BARREL	16875.0	19.9	3350.3	20225.3			19711.0		39936.3
A.2 CENTRAL MAGNET FRAME	16394.0	18.0	2952.5	19346.5			12812.8		32159.3
A.3 ALUMINIUM COIL F/B							4306.4	3119.6	7426.0
A.4 F/B MAGNET FRAME							1968.2	1118.0	3086.2
A.5 S.C. INSERT COIL	2294.7	28.2	646.2	2940.9			1550.0		4490.9
A.6 PROJECT ENGINEERING	492.8	15.0	73.9	566.7			0.0	0.0	566.7
A.7 INSTITUTIONAL SUPPORT	1734.7	20.0	346.9	2081.6			0.0	0.0	2081.6
A. MAGNET (RESISTIVE COIL)	37791.2	19.5	7369.8	45161.0			40348.4	4237.6	89747.0
SUMMARY: A. MAGNET SYSTEM (S.C.COIL)									
A.1 STRUCTURES	12938.0	25.0	3234.5	16172.5			3130.0		19302.5
A.2 COILS	6982.0	29.9	2084.3	9066.3			21000.0		30066.3
A.3 CRYOGENICS	14468.9	21.8	3161.2	17630.1					17630.1
A.4 POWER & PROTECTION SYSTEM	2587.9	18.1	469.0	3056.9					3056.9
A.5 IRON END SHIELDS	1814.5	25.0	453.6	2268.1			13920.0		16188.1
A.6 ALUMINIUM COIL F/B							3960.4	3102.9	7063.3
A.7 MAGNET FRAME F/B							1823.0	1066.2	2889.2
A.8 PROJECT ENGINEERING	492.8	15.0	73.9	566.7					566.7
A.9 INSTITUTIONAL SUPPORT	1690.9	20.0	338.2	2029.0					2029.0
A. MAGNET (S. C. COIL)	40975.0	24.0	9814.7	50789.7			43833.4	4169.1	98792.1

	"1990"	US	Cost	Total Cost					Total Cost
	US Cost	Cont.	US Cont.	US	Switzerl.	Germany	USSR	Ba. + WL	L*
	(k$)	(%)	(k$)	(k$)	(kSF)	(kDM)	(k$)	(k$)	(k$)
SUMMARY: B. MUON DETECTOR									
B.1 CHAMBERS - BARREL	36272.5	16.0	5809.7	42082.2					42082.2
B.2 CHAMBERS - ENDCAP					32210.9				24402.2
B.3 CHAMBERS - F/B								6299.5	6299.5
B.4 SUPPORT STRUCTURE - BARREL	11293.0	15.7	1769.5	13062.5					13062.5
B.5 SUPPORT STRUCTURE - ENDCAP					11988.1				9081.9
B.6 SUPPORT STRUCTURE - F/B								1800.6	1800.6
B.7 SECTOR ASSY./TESTING - BARREL	3309.2	24.6	812.9	4122.1					4122.1
B.8 SECTOR ASSY./TESTING - END CAP					5180.9				3924.9
B.9 SECTOR ASSY./TESTING - F/B								1365.7	1365.7
B.10 ELECTRONICS - BARREL	16923.5	19.8	3354.7	20278.2					20278.2
B.11 ELECTRONICS - END CAP					16803.6				12730.0
B.12 ELECTRONICS - F/B								3671.5	3671.5
B.13 ALIGNMENT & CALIB. - BARREL	3310.6	24.3	804.7	4115.3					4115.3
B.14 ALIGNMENT & CALIB. - END CAP					3069.0				2325.0
B.15 ALIGNMENT & CALIB. - F/B								991.5	991.5
B.16 GAS & AUX. SYSTEMS - BARREL	1468.8	22.1	325.3	1794.1					1794.1
B.17 GAS & AUX. SYSTEMS - END CAP					1929.0				1461.4
B.18 GAS & AUX. SYSTEMS - F/B								278.3	278.3
B.19 TESTING AT SSCL - BARREL	1068.6	20.2	215.6	1284.2					1284.2
B.20 TESTING AT SSCL - END CAP					1410.0				1068.2
B.21 TESTING AT SSCL - F/B								292.4	292.4
B.22 INSTALLATION - BARREL	1582.7	27.8	439.3	2022.0					2022.0
B.23 INSTALLATION - END CAP					2186.5				1656.5
B.24 INSTALLATION - F/B								533.9	533.9
B.25 PROJECT ENGINEERING	770.0	15.0	115.5	885.5	0.0			0.0	885.5
B.26 INSTITUTIONAL SUPPORT	4074.6	20.0	814.9	4889.5	0.0			0.0	4889.5
B. MUON DETECTOR	80073.5	18.1	14462.1	94535.6	74778.1			15233.4	166419.1
B/I MUON DETECTOR BARREL	80073.5	18.1	14462.1	94535.6					94535.6
B/II MUON DETECTOR END CAP					74778.1				56650.1
B/III MUON DETECTOR F/B								15233.4	15233.4

	"1990"	US	Cost	Total Cost					Total Cost
	US Cost	Cont.	US Cont.	US	Switzerl.	Germany	USSR	Ba. + WL	L*
	(k$)	(%)	(k$)	(k$)	(kSF)	(kDM)	(k$)	(k$)	(k$)
SUMMARY: C. HADRON CALORIMETER									
C.1 STRUCTURAL COMPONENTS	1101.0	30.6	336.7	1437.7			5718.4		7156.1
C.2 SENSE LAYER ASSEMBLY	254.7	30.0	76.4	331.1			2347.7		2678.9
C.3 READOUT	16852.8	20.1	3386.3	20239.1					20239.1
C.4 ABSORBER PLATE ASSEMBLY	461.5	30.0	122.3	583.8			5505.0		6088.8
C.5 SCINTILLATING LIQUID	643.5	21.9	140.6	784.1			512.0		1296.1
C.6 THERMAL CONTROL	999.4	30.0	263.4	1262.8			128.0		1390.8
C.7 TESTING	2151.9	25.0	538.0	2689.9					2689.9
C.8 ASSEMBLY & INSTALLATION	7773.1	25.0	1943.3	9716.4			3850.0		13566.4
C.9 TRANSPORTATION	1193.4	20.0	238.7	1432.1					1432.1
C.10 PROJECT ENGINEERING	577.5	15.0	86.6	664.1					664.1
C.11 INSTITUTIONAL SUPPORT	1980.2	20.0	396.0	2376.3					2376.3
C. HADRON CALORIMETER	33989.0	22.1	7528.3	41517.3			18061.1		59578.5

	"1990"	US	Cost	Total Cost					Total Cost
	US Cost	Cont.	US Cont.	US	Switzerl.	Germany	USSR	Ba. + WL	L*
	(k$)	(%)	(k$)	(k$)	(kSF)	(kDM)	(k$)	(k$)	(k$)
SUMMARY: D. E.M. CALORIMETER (BaF2)									
D.1 CRYSTALS						27946.7		17780.1	35810.3
D.2 ELECTRONICS	10811.2	15.3	1656.0	12467.2					12467.2
D.3 MECH. STRUCTURE						17730.6			11439.1
D.4 THERMAL CONTROL						1497.6			966.2
D.5 CALIBRATION SYSTEMS	3832.7	15.0	574.9	4407.6					4407.6
D.6 MANUFACTURING CONTROL						842.5			543.5
D.7 ASSEMBLY & INSTALLATION						6555.0			4229.0
D.8 PROJECT ENGINEERING	346.5	15.0	52.0	398.5		0.0		0.0	398.5
D.9 INSTITUTIONAL SUPPORT	830.2	20.0	166.0	996.2		0.0		0.0	996.2
D. E.M. CALORIMETER (BaF2)	15820.6	15.5	2448.9	18269.6		54572.4		17780.1	71257.7
SUMMARY: D. E.M. CALORIMETER (LIQUID XENON)									
D.1 XENON PROCUREMENT & STORAGE	1681.5	15.0	252.2	1933.7		31496.0		20320.0	42573.7
D.2 XENON PURIFICATION SYSTEM	1637.5	17.1	280.6	1918.1					1918.1
D.3 XENON COOLING SYSTEM	1297.5	15.0	194.6	1492.1					1492.1
D.4 XENON SYSTEM POWER & CONTROL	506.2	15.0	75.9	582.1					582.1
D.5 DETECTOR CHAMBERS & SUPPORT						3942.5			2543.5
D.6 UV REFLECTORS						2479.3			1599.5
D.7 SIGNAL READOUT/MONITORING	8628.5	21.5	1852.9	10481.4		16572.6			21173.4
D.8 INSTALLATION	1641.7	30.0	492.5	2134.2					2134.2
D.9 PROJECT ENGINEERING	577.5	15.0	86.6	664.1		0.0			664.1
D.10 INSTITUTIONAL SUPPORT	1674.1	20.0	334.8	2008.9		0.0			2008.9
D. E.M. CALORIMETER (LIQUID XENON)	17644.5	20.2	3570.3	21214.8		54490.4		20320.0	76689.8

	"1990"	US	Cost	Total Cost					Total Cost
	US Cost	Cont.	US Cont.	US	Switzerl.	Germany	USSR	Ba. + WL	L*
	(k$)	(%)	(k$)	(k$)	(kSF)	(kDM)	(k$)	(k$)	(k$)
SUMMARY: E. CENTRAL TRACKER									
E.1 MECH. ASSY. SILIC. TRACKER	6787.6	19.6	1333.8	8121.4					8121.4
E.2 READOUT SILICON TRACKER	8220.4	63.1	5185.6	13406.0					13406.0
E.3 INSTALLATION SILICON TRACKER	1999.2	24.5	490.3	2489.4					2489.4
E.4 PROJECT ENGINEERING	793.1	11.5	91.5	884.6					884.6
E.5 MECH ASSY. STRAW TUBES/SCI. FIBERS	5983.0	21.4	1278.9	7261.9					7261.9
E.6 READOUT STRAW TUBES/SCI. FIBERS	10056.0	28.9	2910.6	12966.7					12966.7
E.7 INST. STRAW TUBES/SCI. FIBERS	1141.3	16.2	185.3	1326.5					1326.5
E.8 PROJECT ENGINEERING	910.1	11.7	106.5	1016.6					1016.6
E.9 INSTITUTIONAL SUPPORT	4229.6	20.0	845.9	5075.5					5075.5
E. CENTRAL TRACKER	40120.3	31.0	12428.3	52548.6					52548.6
SUMMARY: F. FORWARD CALORIMETER SYSTEM									
F.1 MECHANICS						7599.7			4903.0
F.2 DETECTORS						4506.5			2907.4
F.3 ELECTRONICS	9337.0	15.6	1453.4	10790.4					10790.4
F.4 SYSTEM SUPPORT								1887.7	1887.7
F.5 ASSEMBLY/DET. INTEGRATION						666.5		3235.4	3665.4
F.6 CALIBRATION SYSTEMS						2900.1			1871.0
F.7 INSTALLATION						1297.5			837.1
F.8 PROJECT ENGINEERING	192.5	15.0	28.9	221.4					221.4
F.9 INSTITUTIONAL SUPPORT	503.7	20.0	100.7	604.5		0.0		0.0	604.5
F. FORWARD CALORIMETER SYSTEM	10033.2	15.8	1583.0	11616.2		16970.2		5123.1	27687.8
SUMMARY: G. COMPUTER									
G.1 Computer System								10000.0	10000.0
G. COMPUTER								10000.0	10000.0

	"1990 Cost" (k$)	Contingency (%)	Contingency Cost (k$)	Total Cost L* Detector (k$)
SUMMARY: A. MAGNET SYSTEM (RESISTIVE COIL)				
A.1 ALUMINIUM COIL BARREL	52769.8	17.5	9253.1	62022.9
A.2 CENTRAL MAGNET FRAME	54450.8	17.5	9507.6	63958.4
A.3 ALUMINIUM COIL F/B	10326.0	19.2	1984.6	12310.6
A.4 F/B MAGNET FRAME	6506.2	17.5	1140.4	7646.6
A.5 S.C. INSERT COIL	4296.7	27.6	1186.7	5483.4
A.6 PROJECT ENGINEERING	1155.0	15.0	173.3	1328.3
A.7 INSTITUTIONAL SUPPORT	2686.1	20.0	537.2	3223.3
A. MAGNET (RESISTIVE COIL)	132190.6	18.0	23782.9	155973.5
SUMMARY: A. MAGNET SYSTEM (S.C.COIL)				
A.1 STRUCTURES	35632.9	24.8	8832.2	44465.1
A.2 COILS	34186.0	30.0	10241.7	44427.7
A.3 CRYOGENICS	14510.9	21.9	3171.7	17682.6
A.4 POWER & PROTECTION SYSTEM	2587.9	18.1	469.0	3056.9
A.5 IRON END SHIELDS	17247.0	16.9	2919.8	20166.8
A.6 ALUMINIUM COIL F/B	10188.3	19.5	1990.7	12179.0
A.7 MAGNET FRAME F/B	6000.2	17.2	1034.7	7034.9
A.8 PROJECT ENGINEERING	1155.0	15.0	173.3	1328.3
A.9 INSTITUTIONAL SUPPORT	5915.3	20.0	1183.1	7098.3
A. MAGNET (S. C. COIL)	127423.5	23.6	30016.1	157439.6

	"1990 Cost" (k$)	Contingency (%)	Contingency Cost (k$)	Total Cost L* Detector (k$)
SUMMARY: B. MUON DETECTOR				
B.1 CHAMBERS - BARREL	36272.5	16.0	5809.7	42082.2
B.2 CHAMBERS - ENDCAP	24514.7	16.3	4006.3	28521.0
B.3 CHAMBERS - F/B	6299.5	16.8	1057.2	7356.7
B.4 SUPPORT STRUCTURE - BARREL	11293.0	15.7	1769.5	13062.5
B.5 SUPPORT STRUCTURE - ENDCAP	9053.5	15.6	1413.6	10467.1
B.6 SUPPORT STRUCTURE - F/B	1800.6	15.6	280.3	2080.9
B.7 SECTOR ASSY./TESTING - BARREL	3309.2	24.6	812.9	4122.1
B.8 SECTOR ASSY./TESTING - END CAP	3950.4	25.0	986.2	4936.6
B.9 SECTOR ASSY./TESTING - F/B	1365.7	23.9	326.4	1692.1
B.10 ELECTRONICS - BARREL	16923.5	19.8	3354.7	20278.2
B.11 ELECTRONICS - END CAP	12731.7	20.0	2544.9	15276.6
B.12 ELECTRONICS - F/B	3671.5	20.4	748.9	4420.5
B.13 ALIGNMENT & CALIB. - BARREL	3310.6	24.3	804.7	4115.3
B.14 ALIGNMENT & CALIB. - END CAP	2333.3	25.4	593.6	2926.9
B.15 ALIGNMENT & CALIB. - F/B	991.5	24.5	243.4	1234.9
B.16 GAS & AUX. SYSTEMS - BARREL	1468.8	22.1	325.3	1794.1
B.17 GAS & AUX. SYSTEMS - END CAP	1468.8	22.1	325.3	1794.1
B.18 GAS & AUX. SYSTEMS - F/B	278.3	23.5	65.3	343.6
B.19 TESTING AT SSCL - BARREL	1068.6	20.2	215.6	1284.2
B.20 TESTING AT SSCL - END CAP	1075.6	20.1	216.7	1292.3
B.21 TESTING AT SSCL - F/B	292.4	20.6	60.1	352.5
B.22 INSTALLATION - BARREL	1582.7	27.8	439.3	2022.0
B.23 INSTALLATION - END CAP	1672.3	27.8	465.6	2137.9
B.24 INSTALLATION - F/B	533.9	28.2	150.7	684.6
B.25 PROJECT ENGINEERING	1925.0	15.0	288.8	2213.8
B.26 INSTITUTIONAL SUPPORT	9249.4	20.0	1849.9	11099.3
B. MUON DETECTOR	158437.0	18.4	29154.7	187591.7
B/I MUON DETECTOR BARREL	80073.5	18.1	14462.1	94535.6
B/II MUON DETECTOR END CAP	60936.2	18.6	11340.8	72277.0
B/III MUON DETECTOR F/B	17427.3	19.2	3351.8	20779.1

	"1990 Cost" (k$)	Contingency (%)	Contingency Cost (k$)	Total Cost L* Detector (k$)
SUMMARY: C. HADRON CALORIMETER				
C.1 STRUCTURAL COMPONENTS	7269.4	26.2	1905.1	9174.5
C.2 SENSE LAYER ASSEMBLY	2685.5	30.0	805.7	3491.2
C.3 READOUT	17254.8	20.2	3481.7	20736.5
C.4 ABSORBER PLATE ASSEMBLY	6199.0	20.8	1287.8	7486.8
C.5 SCINTILLATING LIQUID	1257.5	23.4	294.1	1551.6
C.6 THERMAL CONTROL	1371.0	27.2	373.2	1744.2
C.7 TESTING	3105.0	25.0	776.3	3881.3
C.8 ASSEMBLY & INSTALLATION	17337.2	25.0	4334.3	21671.5
C.9 TRANSPORTATION	1193.4	20.0	238.7	1432.1
C.10 PROJECT ENGINEERING	1155.0	15.0	173.3	1328.3
C.11 INSTITUTIONAL SUPPORT	6472.2	20.0	1294.4	7766.6
C. HADRON CALORIMETER	65300.0	22.9	14964.5	80264.6

	"1990 Cost" (k$)	Contingency (%)	Contingency Cost (k$)	Total Cost L* Detector (k$)
SUMMARY: D. E.M. CALORIMETER (BaF2)				
D.1 CRYSTALS	35843.3	20.0	868.7	36711.9
D.2 ELECTRONICS	10811.2	15.3	1656.0	12467.2
D.3 MECH. STRUCTURE	11508.5	15.0	1726.3	13234.8
D.4 THERMAL CONTROL	980.5	15.6	152.7	1133.2
D.5 CALIBRATION SYSTEMS	3832.7	15.0	574.9	4407.6
D.6 MANUFACTURING CONTROL	611.0	30.0	183.3	794.3
D.7 ASSEMBLY & INSTALLATION	5182.0	25.0	1295.5	6477.5
D.8 PROJECT ENGINEERING	924.0	15.0	138.6	1062.6
D.9 INSTITUTIONAL SUPPORT	2563.0	20.0	512.6	3075.5
D. E.M. CALORIMETER (BaF2)	72256.2	12.6	7108.6	79364.8
SUMMARY: D. E.M. CALORIMETER (LIQUID XENON)				
D.1 XENON PROCUREMENT & STORAGE	42321.5	5.8	2284.2	44605.7
D.2 XENON PURIFICATION SYSTEM	1637.5	17.1	280.6	1918.1
D.3 XENON COOLING SYSTEM	1297.5	15.0	194.6	1492.1
D.4 XENON SYSTEM POWER & CONTROL	506.2	15.0	75.9	582.1
D.5 DETECTOR CHAMBERS & SUPPORT	2623.0	18.6	488.5	3111.5
D.6 UV REFLECTORS	1679.0	21.6	363.0	2042.0
D.7 SIGNAL READOUT/MONITORING	19320.5	17.9	3456.7	22777.2
D.8 INSTALLATION	1641.7	30.0	492.5	2134.2
D.9 PROJECT ENGINEERING	924.0	15.0	138.6	1062.6
D.10 INSTITUTIONAL SUPPORT	2315.0	20.0	463.0	2778.1
D. E.M. CALORIMETER (LIQUID XENON)	74265.9	13.4	8237.7	82503.7

	"1990 Cost" (k$)	Contingency (%)	Contingency Cost (k$)	Total Cost L* Detector (k$)
SUMMARY: E. CENTRAL TRACKER				
E.1 MECH. ASSY. SILIC. TRACKER	6787.6	19.6	1333.8	8121.4
E.2 READOUT SILICON TRACKER	8220.4	63.1	5185.6	13406.0
E.3 INSTALLATION SILICON TRACKER	1999.2	24.5	490.3	2489.4
E.4 PROJECT ENGINEERING	793.1	11.5	91.5	884.6
E.5 MECH ASSY. STRAW TUBES/SCI. FIBERS	5983.0	21.4	1278.9	7261.9
E.6 READOUT STRAW TUBES/SCI. FIBERS	10056.0	28.9	2910.6	12966.7
E.7 INST. STRAW TUBES/SCI. FIBERS	1141.3	16.2	185.3	1326.5
E.8 PROJECT ENGINEERING	910.1	11.7	106.5	1016.6
E.9 INSTITUTIONAL SUPPORT	4229.6	20.0	845.9	5075.5
E. CENTRAL TRACKER	40120.3	31.0	12428.3	52548.6
SUMMARY: F. FORWARD CALORIMETER SYSTEM				
F.1 MECHANICS	4975.0	14.2	707.3	5682.3
F.2 DETECTORS	2988.6	21.0	628.9	3617.5
F.3 ELECTRONICS	9337.0	15.6	1453.4	10790.4
F.4 SYSTEM SUPPORT	1887.7	21.3	401.7	2289.3
F.5 ASSEMBLY/DET. INTEGRATION	3665.4	19.6	718.1	4383.5
F.6 CALIBRATION SYSTEMS	2031.0	26.0	528.8	2559.8
F.7 INSTALLATION	1004.0	30.0	301.2	1305.2
F.8 PROJECT ENGINEERING	616.0	15.0	92.4	708.4
F.9 INSTITUTIONAL SUPPORT	2188.4	20.0	437.7	2626.1
F. FORWARD CALORIMETER SYSTEM	28693.1	18.4	5269.2	33962.3
SUMMARY: G. COMPUTER				
G.1 Computer System	10000.0	30.0	3000.0	13000.0
G. COMPUTER	10000.0	30.0	3000.0	13000.0